

---

# **Incidence and transfer behaviors of high-order hot jud- der in passenger cars**

Vom Fachbereich Maschinenbau an der  
Technischen Universität Darmstadt  
zur Erlangung des Grades eines  
Doktor-Ingenieurs (Dr.-Ing.)  
genehmigte

## **Dissertation**

vorgelegt von

**Xinfu Xu M.Sc.**  
aus Shandong, China

Berichterstatter: Prof. Dr. rer. nat. Hermann Winner

Mitberichterstatter: Prof. Dr.-Ing. Tobias Melz

Tag der Einreichung: 20.10.2016

Tag der mündlichen Prüfung: 06.12.2016

Darmstadt 2016

D 17



---

# Preface

This work is created during the period that I worked as a research assistant in the Institute of Automotive Engineering (FZD) of Technische Universität Darmstadt, under the supervision of Prof. Dr. rer. nat. Hermann Winner. The research work was supported by the China Scholarship Council (CSC) under the State Scholarship Fund (grant number: 2011626046).

In the first place, I want to express my special gratitude to my doctoral supervisor, Prof. Dr. rer. nat. Hermann Winner, for his constant guidance, understanding, trust, and tolerance. Without his supervision and support, my promotion would be not possible. The numerous discussions and suggestions have always been inspiring me, not only in the aspect of scientific research, but also in many other aspects of my life.

I would like to thank Prof. Dr. -Ing. Tobias Melz most sincerely for his interest in this research topic, and for the co-supervision of this work.

I wish to extend my heartfelt thanks to CSC for the financial support, which makes the execution of the whole research work possible.

Moreover, I would like to thank all the staff members at FZD, including all the research assistants, the secretaries and the workshop staff, for the pleasant and efficient working atmosphere. I would like to especially thank Dr. Gunther Seipel and Dr. Sebastian Geyer for their kind helps in the process of adaptation into FZD and Germany, and I would also like to extend my especial thanks to Sebastian Fischer, my former office mate, who has given me many helps and so many good suggestions on the research topic of hot judder. Meanwhile, I would like to state my extra thanks to the workshop staff, for all their assistances to the bench test and the vehicle road tests.

I would like to acknowledge the colleagues from Continental Teves, especially Dr. Martin Semsch, Dr. Angelo Sardá, and Dr. Mathias Haag who have provided valuable friendly support for the hot judder tests at the chassis dynamometer. I would like to thank Maximilian Könnig for his coordination in the course of the vehicle tests.

Last but not least, I would like to thank my parents for their everlasting love and support during my entire education period. I also want to thank my parents-in-law for taking care of my daughter during the last more than two years and for their endless supports and good wishes. I would like to give the special thanks to my wife, Yinan Zhu, for her affectionate support and encouragement during all circumstances in both work and life; and to my daughter, Zhurui Xu, for her every laugh and smile.



---

# Table of contents

<b>Preface</b> .....	<b>III</b>
<b>Table of contents</b> .....	<b>V</b>
<b>Abbreviations</b> .....	<b>IX</b>
<b>Symbols and indices</b> .....	<b>X</b>
<b>Summary</b> .....	<b>XIII</b>
<b>1 Introduction</b> .....	<b>1</b>
1.1 Brake induced noises and vibrations .....	1
1.2 Hot spot types .....	4
1.3 The whole process of hot judder.....	5
1.4 Motivation .....	6
<b>2 State of the art</b> .....	<b>11</b>
2.1 Mechanisms of high-order hot judder .....	11
2.1.1 Cause and effect chain found by Sardá .....	11
2.1.2 TEL.....	12
2.1.3 PWD.....	15
2.1.4 Hot judder caused by resonance frequency.....	16
2.1.5 Hot judder caused by cooling vent.....	17
2.1.6 Influential factors of hot judder occurrence .....	18
2.2 Transfer behaviors of brake judder .....	20
2.2.1 Vehicle tests by Engel .....	20
2.2.2 MBS models.....	21
2.2.3 FE and analytical models .....	26
2.2.4 Conclusion of the transfer behaviors.....	28
2.3 Human perception of vibration.....	29
2.3.1 Subjective rating of brake judder induced vibrations .....	29
2.3.2 Frequency weighting of vibration .....	31
2.4 Human sensations of sound .....	33
2.4.1 Sound pressure and SPL.....	33
2.4.2 Psychoacoustics.....	34
2.4.3 Equal loudness contours and frequency weighting filters.....	36
<b>3 Goals and overall methodology</b> .....	<b>39</b>
3.1 Scientific goals .....	39
3.2 Overall methodology .....	40

<b>4 Test methodology.....</b>	<b>42</b>
4.1 Basics and definitions.....	42
4.1.1 Fist caliper brake.....	42
4.1.2 Definition of the characteristic parameters.....	43
4.2 Methodology for transferability investigation.....	44
4.2.1 Test strategy of the comparison test.....	44
4.2.2 Test setups of the comparison test.....	46
4.2.3 Methodology of the modification test.....	50
4.2.4 Methodology of the identification test.....	51
4.3 Methodology for the transfer behaviors.....	51
4.3.1 The fundamental investigation strategy.....	51
4.3.2 The novel test method: artificially modified discs.....	53
4.3.3 Test vehicles and modified discs.....	53
4.3.4 Test setup.....	55
4.3.5 Data acquisition system.....	57
4.3.6 Test maneuver.....	58
4.4 Methodology for subjective rating.....	59
4.4.1 Subjective evaluation system.....	59
4.4.2 Subjective rating strategy.....	60
4.5 Order analysis of hot judder.....	60
4.5.1 Definition and clarification of the dominant order.....	60
4.5.2 Mechanism of adjacent orders.....	62
4.5.3 Mechanism of lower-order hot judder.....	66
4.5.4 Harmonic orders caused by the modified discs.....	68
<b>5 Transferability from dynamometer test to vehicle test.....</b>	<b>70</b>
5.1 Evaluation strategy for comparison test.....	70
5.2 Comparison of the front brake.....	71
5.3 Comparison of the rear brake.....	72
5.3.1 Drag braking application.....	72
5.3.2 Stop braking application.....	74
5.4 Results of the modification test.....	75
5.5 Results of the identification test.....	76
<b>6 Transfer behaviors of high-order judder.....</b>	<b>78</b>
6.1 Determination of transfer functions.....	78
6.1.1 Time signals and spectral analysis.....	78
6.1.2 Coherence analysis.....	80
6.1.3 Calculation of the transfer functions.....	81
6.1.4 Reproducibility of the results.....	85
6.2 Transfer mechanisms of drone noise.....	87
6.2.1 The assumed transfer paths of drone noise.....	87
6.2.2 Drone noise emission from the disc/pads interfaces.....	88

6.2.3 Drone noise propagation from vehicle exterior to interior.....	90
6.2.4 Coherence between interior drone noise and dashboard vibration .....	91
6.3 Discussion.....	93
<b>7 Perception of high-order judder .....</b>	<b>95</b>
7.1 Determination of the critical SPL.....	95
7.1.1 Vehicle interior noise level.....	95
7.1.2 Auditory masking and selection of the critical SPL.....	98
7.2 Determination of the critical vibrations.....	101
7.2.1 Subjective rating and objective assessment .....	101
7.2.2 Regression analysis .....	102
7.2.3 Threshold values of BPV and BTV.....	104
<b>8 Conclusion and outlook .....</b>	<b>111</b>
8.1 Conclusion.....	111
8.2 Outlook .....	113
<b>A Statistics of the hot judder investigations from literatures .....</b>	<b>114</b>
<b>B Test and evaluation methodology.....</b>	<b>116</b>
B.1 Dynamometer setup of rear brake test.....	116
B.2 Examples of non-uniform hot spots.....	116
B.3 Order analysis of the thermal variation .....	118
B.4 Order analysis of BTV, BPV, DTV, LRO .....	118
<b>C Test results .....</b>	<b>119</b>
C.1 Influence of adapter stiffness on the order behaviors.....	119
C.2 The post-processing anti-aliasing filter used for the WFS signals .....	119
C.3 Time signals of one test with a modified disc .....	121
C.4 High-order judder of the rear brake .....	121
C.5 SPL spectrum of exterior drone noise .....	122
C.6 Amplitudes of BTV and BPV .....	123
<b>Reference .....</b>	<b>125</b>
<b>Own publications .....</b>	<b>134</b>
<b>Supervised Bachelor/ Master theses.....</b>	<b>135</b>
<b>Curriculum vitae.....</b>	<b>136</b>





# Abbreviations

<b>Abbreviation</b>	<b>Description</b>
<i>AC</i>	alternating current
<i>AM</i>	amplitude modulation
<i>AN</i>	airborne noise
<i>AWD</i>	all wheel drive
<i>BPV</i>	brake pressure variation
<i>BTV</i>	brake torque variation
<i>CAN</i>	controller area network
<i>CSC</i>	China Scholarship Council
<i>DOE</i>	design of experiment
<i>DT</i>	disc thickness
<i>DTV</i>	disc thickness variation
<i>ECE</i>	Economic Commission for Europe
<i>EHB</i>	electro-hydraulic brake
<i>EMB</i>	electro-mechanical brake
<i>FE</i>	finite element
<i>FZD</i>	Fahrzeugtechnik Darmstadt
<i>GTF</i>	global transfer function
<i>HBM</i>	Hottinger Baldwin Messtechnik
<i>IQR</i>	interquartile range
<i>HPS</i>	hydraulic power steering
<i>LRO</i>	lateral run out
<i>LTF</i>	local transfer function
<i>LTI</i>	linear time-invariant
<i>MBS</i>	multi-body simulation
<i>MTVV</i>	maximum transient vibration value
<i>NAO</i>	non-asbestos organic
<i>NTP</i>	Network Time Protocol
<i>NVH</i>	noise, vibration, harshness
<i>OEM</i>	original equipment manufacturer
<i>PWD</i>	progressive waviness distortion
<i>RMS</i>	root mean square
<i>SN</i>	structure-borne noise
<i>SPL</i>	sound pressure level
<i>SRO</i>	side-face run out
<i>SUV</i>	sport utility vehicle
<i>TEI</i>	thermo-elastic instability
<i>TPA</i>	transfer path analysis
<i>WFS</i>	wheel force sensor

---

## Symbols and indices

Symbol	Unit	Description
$A$	$s^2$	area
$a$	$m/s^2$	acceleration
$b$	-	complex exponential growth rate
$C$	1	coherence coefficient
$c$	$m/s$	speed of sound
$d$	$m$	distance
$E$	Pa, $N/m^2$	Young's modulus
$e$	-	expected value
$\hat{e}$	-	maximum likelihood of expected value
$F$	$N$	force
$f$	$Hz$	frequency
$f$	$Hz$	frequency array
$f'$	-	normalized frequency
$G$	-	gain, transfer function
$g$	$9.81m/s^2$	acceleration due to gravity
$h$	1	wave number in equation 2.2
$I$	$W/m^2$	sound intensity
$k$	1; 1	total number of explanatory variables; multiplying factors
$L_N$	phon	loudness level
$L_p$	dB	sound pressure level
$M$	$Nm$	moment, torque
$m$	1	degree of the polynomial regression model
$N$	1	order of brake judder
$N_s$	1	sample size
$n$	rps	rotational speed
$n$	rps	rotational speed array
$P$	$W$	power
$P_s$	$W/Hz$	power spectral density
$p$	bar; Pa	brake pressure; sound pressure
$q$	$J$	heat
$r$	1; $m$	correlation coefficient; radius in the cylindrical polar coordinate system
$R$	-; $\Omega$	real part; resistance
$R^2$	1	coefficient of determination
$\overline{R}^2$	1	adjusted coefficient of determination
$S$	-	sample standard deviation
$S^2$	-	sample variance
$S_N$	sones	loudness
$T$	$K, ^\circ C$	temperature
<b>X</b>		

$t$	s	time
$t_e$	s	vibration exposure duration, the entire time of one braking application
$t_o$	s	time of observation
$U$	-	pivotal quantity
$v$	m/s	velocity
$W$	1	frequency weighting filter
$X$	1	statistical population
$\bar{X}$	1	sample mean
$Z_0$	Pa·s/m	specific acoustic impedance
$x$	-	variable used in the mathematical equations
$y$	-	variable used in the mathematical equations
$z$	-	variable used in the mathematical equations
$\alpha$	1	significance level
$\beta$	1	unknown parameter in the regression model
$\chi$	1/K	coefficient of thermal expansion
$\varepsilon$	-	random error in the polynomial regression model
$\varphi$	rad	angle
$\kappa$	W/(m · K)	thermal conductivity
$\mu$	1	coefficient of friction
$\nu$	1	Poisson's ratio
$\rho$	kg/m <sup>3</sup>	density
$\sigma$	-	standard deviation
$\sigma^2$	-	variance
$\sigma^2$	-	maximum likelihood of variance
$\tau$	s	integration time constant for running averaging
$\Theta$	K, °C	nodal temperature
$\zeta$	1	acoustic efficiency

<b>Index</b>	<b>Description</b>
<i>atu</i>	actuation direction
B	brake
<i>BS</i>	braking system
<i>brake</i>	wheel brake
<i>carrier</i>	carrier signal
<i>circ</i>	circumferential direction
<i>critical</i>	critical speed, critical values of drone noise
D	brake disc
<i>exterior</i>	vehicle exterior
<i>finger</i>	finger side
<i>flexible</i>	flexible knuckle adapter
<i>interior</i>	vehicle interior
<i>mech</i>	mechanical
<i>modulation</i>	modulation signal
<i>noise</i>	drone noise
<i>pedal</i>	brake pedal
<i>piston</i>	piston side
<i>rms</i>	root mean square
<i>ST</i>	seat track
<i>StS</i>	steering system
<i>stiffer</i>	stiffer knuckle adapter
<i>SUS</i>	suspension system
<i>SW</i>	steering wheel
<i>target</i>	the target point on the order line
<i>thres</i>	threshold value
<i>total</i>	(vibration) total value
<i>w</i>	frequency weighting
<i>X</i>	in x-direction (the vehicle's longitudinal direction)
<i>Y</i>	in y-direction (the vehicle's transverse direction)
<i>Z</i>	in z-direction (the vehicle's vertical direction)

---

## Summary

As one of the brake-induced noises and vibrations, hot judder is forced vibration, which is caused by unevenness of the brake disc due to the thermal mechanical interactions in wheel brakes. Brake disc unevenness is normally described and evaluated as the Disc Thickness Variation (DTV) and the disc' Lateral Run-Out (LRO). DTV and LRO generate Brake Pressure Variation (BPV) and Brake Torque Variation (BTV) in wheel brakes, which are transmitted to the driver and perceived by the driver as the brake pedal pulsation, the steering wheel oscillation, the car body vibrations, and low-frequency drone noises inside a vehicle.

Hot judder is characterized by hot spots on the disc surfaces. The frequency of hot judder is dependent on the wheel rotational speed, showing order behaviors. The number of hot spots generally corresponds to the dominant order of hot judder. In the last decades, most of the hot judder tests have been carried out with brake dynamometers, and high numbers (typically around 10) of hot spots were found in the majority of the tests. The generation and development mechanisms of the high dominant order have been almost the exclusive focus of current hot judder researches. However, the influences of the vibrations and noises (with higher frequencies compared with the low-order cold judder) caused by high-order hot judder on the driver's subjective perception have been still not clarified. That is to say, it is still unknown in which form and under which conditions, the high-order hot judder can be transmitted to and perceived by the driver, and thus causing customer complaints.

A top-down approach is used in order to investigate the influences of high-order judder on driver's perception with respect to two aspects: the incidence of high-order hot judder in vehicle tests and the drivers' perception of high-order hot judder. The first aspect is mainly investigated by studying the transferability of dynamometer tests to vehicle tests and by identifying the incidence of high-order hot judder in production brakes. Specifically, identical brakes from one front brake and one rear brake are separately tested with a brake dynamometer and through vehicle tests by means of road tests and chassis dynamometer tests, and all brakes of four production passengers are identified with accelerometers attached on the brake caliper and the caliper bracket.

The perception of high-order hot judder is chiefly studied by investigating its transfer behaviors. Global transfer functions from BPV/BTV to the selected driver interface quantities (brake pedal pulsation, steering wheel oscillation, seat track vibrations, and vehicle interior drone noise) are defined, which establish the links between the hot judder intensity in the wheel brake and the intensity at the driver interface. In order to

identify the transfer functions with a high signal-noise-ratio and better reproducibility, a novel testing method is adopted: vehicle tests with brake discs that are artificially modified with the desired surface shapes simulating the high-order DTV/LRO. Altogether three vehicles with seven different modified discs are tested. Two critical levels of drone noise (60 and 80 dB(A)) are selected according to the general vehicle total noise level and the human's perception characteristics of sound. The perception threshold values of the driver interface vibrations are obtained through regression analysis between their subjective ratings and objective measurements. Based on the critical drone noise levels and the threshold values of vibrations, as well as the global transfer functions, threshold values of BPV and BTV for perceiving the high-order judder are computed.

Concerning the incidence of high-order judder, both the dominant order and the thermal increases of BTV and BPV for the dominant order showed great discrepancies in different test types (e.g. brake dynamometer or vehicle, drag braking application with constant velocity and constant pressure/torque or stop braking application with decreasing velocity and constant deceleration/pressure). Hot judder behaviors in the brake dynamometer test were not transferable to the vehicle tests. Besides, no evident high-order hot judder has been identified in all the brakes of the four passenger cars. Generally, hot judder seems to be more likely to be excited at the brake dynamometer than in the vehicles. Therefore, brake dynamometer test is still appropriate for detecting hot judder in the early phase of brake development, and thus preventing its occurrence in the vehicle.

Regarding the driver's perception, the drone noise is the most probable reason leading to customer complaints, since higher than 100 Hz less than 10 Nm BTV is required to perceive the drone noise and 50 Nm BTV can already result in unacceptable drone noise. The driver is less sensitive to the vibrations caused by high-order judder. Roughly at least 20 Nm BTV or 2.5 bar BPV is needed for perceiving the vibrations, and the perception is most possibly due to the steering wheel oscillation or the vertical vehicle vibration. Moreover, some resonances in the transfer paths play a significant role in the high-order judder transmission. Although the investigations in this work are limited to three vehicles, the practical significance of high-order hot judder on the driver's perception is revealed for the first time. With these results, the impact of the measured BTV and BPV of hot judder, e.g. in the brake dynamometer tests, can be assessed.

Combining these results, the most effective and efficient way to mitigate the high-order hot judder would be reducing its occurrences in the wheel brakes and diminishing the prominent resonances in the transfer paths.

# 1 Introduction

## 1.1 Brake induced noises and vibrations

The customer requirements for the driving comfort and the vehicle NVH behaviors are continuously increasing in the last decades und will still be higher and higher<sup>1</sup>. A lot of noises and vibrations may be induced by the braking system in a vehicle during braking. Figure 1-1 shows a classification of noises and vibrations caused by the braking system according to their occurring frequencies. Preventing or reducing these noises and vibrations is a major target firmly integrated in the development of wheel brake systems at both brake suppliers and vehicle manufactures.

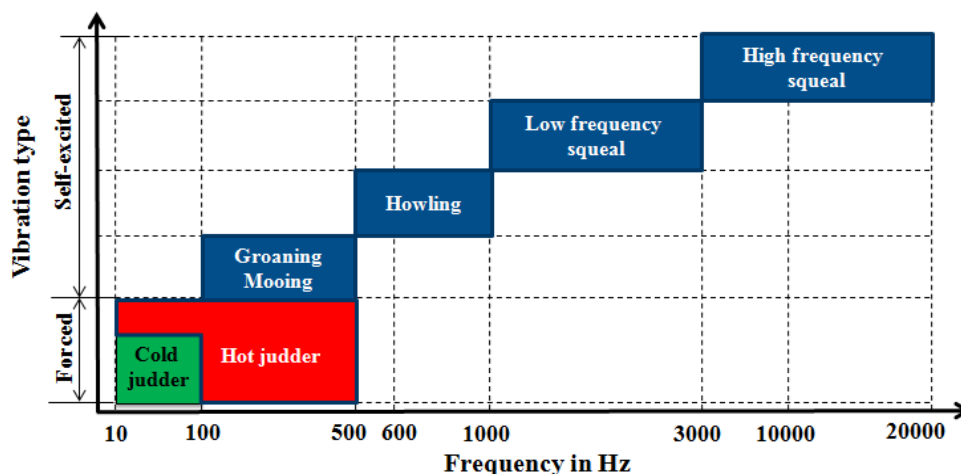


Figure 1-1: Classification of the brake induced noises and vibrations<sup>2</sup>

Brake squeal is the result of self-excited vibrations of the wheel brake. The frequencies of brake squeal are associated with the resonances of the brake components. There are two types of brake squeal: the low-frequency squeal and the high-frequency squeal. The difference between them is the mode shapes involved in the modal coupling mechanism. The low-frequency squeal is related to the out-of-plane modes of the brake disc (in the axial direction of the brake disc) and the bending modes of the brake pads, whereas the high-frequency squeal attributes to the in-plane modes of the brake disc (in the circumferential and radial directions of the brake disc). Because the brake disc is

<sup>1</sup> Genuit: Sound-Engineering im Automobilbereich, 2010, p.90.

<sup>2</sup> cf. Breuer und Bill: Brake technology handbook, 2008, p.410.

much stiffer in the in-plane direction than in the out-of-plane direction, the high-frequency squeal happens in a higher frequency range than the low frequency squeal.<sup>3</sup>

Howling, groaning and mooing are also self-excited vibrations, resulting from the vibrations that are caused by the dynamic instability of the wheel brake system. They are characterized by one or more tonal components<sup>4</sup>. Compared with howling, groaning and mooing happen in a lower frequency range and are related with the stick-slip phenomenon<sup>5,6,7</sup>. Brake squeal, howling, groaning and mooing often occur during light or light to medium braking shortly before standstill when the vehicle's total noise level is especially low. Therefore, they are very annoying for the driver and passengers.

Unlike the self-excited brake noises, brake judder is featured as forced, low-frequency vibration. It occurs during light to moderate (0.1 to 0.5 g) braking from higher speeds to lower speeds and it is normally perceived by the driver as vibrations at the driver interface, such as the steering wheel oscillation, the brake pedal pulsation, the seat and the foot floor vibrations, or even the whole vehicle body vibrations. Sometimes, it is also accompanied by a low-frequency drone noise<sup>8</sup>. Typical occurring conditions of the brake induced noises and vibrations are listed in Table 1-1.

Table 1-1: Occurring conditions and features of the brake induced noises and vibrations<sup>9</sup>

Vibration Type	Speed	Deceleration	Pressure	Temperature
<b>High frequency squeal</b>	< 10 km/h	light -medium	5-30 bar	up to 300 °C
<b>Low frequency squeal</b>	< 10 km/h	light -medium	5-30 bar	up to 300 °C
<b>Howling</b>	< 10 km/h	light	up to 10 bar	-
<b>Groaning, mooing</b>	< 15 km/h	light	up to 10 bar	-
<b>Cold judder</b>	160-80 km/h	light -medium	10-30 bar	< 200 °C
<b>Hot judder</b>	160-80 km/h	light -medium	10-30 bar	200-800 °C

Brake judder is mainly caused by the Disc Thickness Variation (DTV) and the disc's Lateral Run-Out (LRO, in many literatures also called waviness of the disc, or the Side-

<sup>3</sup> Triches Jr et al.: Reduction of squeal noise, 2004, p.341.

<sup>4</sup> Bittner: Reduzierung des Bremsrubbels, 2006, p.5–6.

<sup>5</sup> Abdelhamid and Bray: Braking systems creep groan noise, 2009, p.1.

<sup>6</sup> Jung and Chung: Research for brake creep groan noise with dynamometer, 2012, p.1.

<sup>7</sup> Woo et al.: Transfer path analysis of brake creep groan noise, 2014, p.1.

<sup>8</sup> Kubota et al.: Mechanism causing high-speed brake judder, 1998, p.133–137.

<sup>9</sup> Bittner: Reduzierung des Bremsrubbels, 2006, p.3.



face Run Out, SRO). According to the different occurring reasons of DTV and LRO, brake judder is traditionally divided into two categories: cold judder and hot judder.

DTV and LRO of cold judder are induced by production tolerances, mechanical wear (cold washout) or the deviation of disc axle resulting from assembly, which mainly happen in the off-brake status<sup>10,11</sup>.

DTV and LRO of hot judder are mainly caused by the thermal mechanical effects in wheel brakes during braking. They are normally combined with hot spots distributed in the circumferential direction of disc surfaces<sup>12</sup>. The temperature relating processes in the disc/pads interfaces lead to temporary, localized thermal expansion (reversible LRO and DTV as the result) on the one hand, and permanent changes in the micro-structure of disc materials (known as martensite formation<sup>13</sup>, resulting in irreversible LRO and DTV) on the other hand. Due to the irregular material changes along disc surfaces and the dependence of the friction coefficient on the contact pressure and especially on the surface temperature, variation of friction coefficient ( $\mu$ -variation) on the disc friction rings may emerge<sup>14</sup>, which is another reason of hot judder.

Because brake judder is forced vibration that is caused by DTV and LRO of brake discs, it is normally characterized by order behaviors. The order of brake judder  $N$  is defined as the integer number of the vibration excitations per disc rotation. It is calculated with the disc's rotational speed  $n$  divided by the brake judder induced vibration frequency  $f$ :

$$N = \frac{f}{n} \quad (1.1)$$

As a result of the mechanism of cold washout, cold judder mostly happens with lower orders (typically 1<sup>st</sup> -3<sup>rd</sup> order) and thus occurs in the lower frequency range. However, because the number of hot spots is generally corresponding to the dominant order of hot judder and hot judder is typically characterized by high number of hot spots, hot judder normally happens with higher orders and higher frequencies.

Besides, under high temperatures the DTV and LRO of cold judder will be intensified by the thermal expansion, as manifested by Meyer, displayed in Figure 1-2. Thermal increases of the lower orders of cold judder are also sorted as hot judder phenomenon in this work. Therefore, hot judder might also happen in the lower frequency range (see Figure 1-1).

---

<sup>10</sup> Engel: Systemansatz zur bremseregter Lenkunruhe, 1998

<sup>11</sup> Hodges and Dlugosch: Methode zur Bremsen-Kaltrubbeln, 2001

<sup>12</sup> Sardá: Wirkungskette von Hotspots und Heißrubbeln, 2009

<sup>13</sup> Kreitlow et al.: Vibration and "hum" of disc brakes, 1985, p.1434–1436.

<sup>14</sup> De Vries, A. and Wagner, M.: The brake judder phenomenon, 1992, p.27.

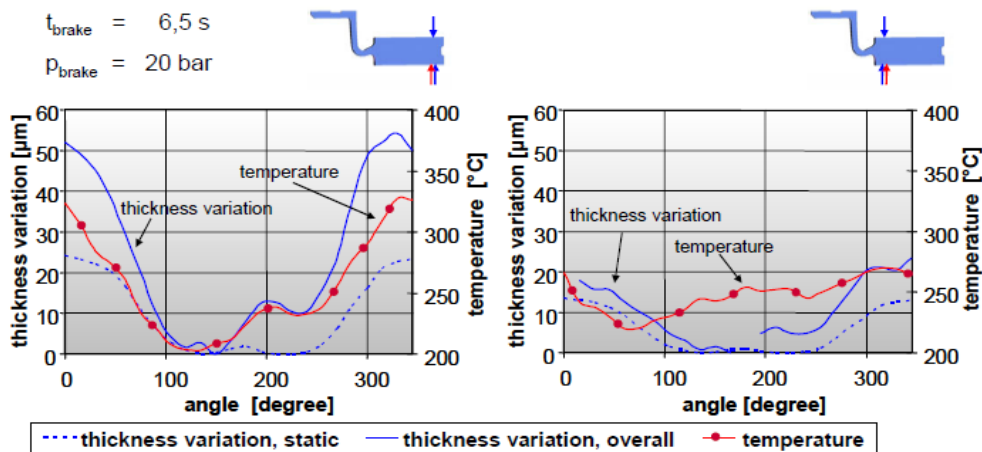


Figure 1-2: The thermal increase of cold judder, the static thickness variation of cold judder is intensified by the thermal effect during braking with  $v = 175$  to  $50$  km/h and  $a = -0.3 g$ <sup>15</sup>

## 1.2 Hot spot types

Hot spots are firstly classified into different types by Anderson and Knapp in 1990<sup>16</sup>, and the thermographic illustrations (see Figure 1-3) of the hot spot types were given by Pufrenoy et al. according to the similar classification. Generally, five different types of thermal variations on brake discs were defined as listed in Table 1-2<sup>17</sup>:

- Asperity results from discrete asperity contacts. Temperatures rise rapidly but briefly on very small areas of the rubbing surfaces.
- Gradients on hot bands correspond to small contact sites which appear along a single rubbing path.
- Hot bands appear as reduced contact friction areas of the pad in the radial direction. It is seen on the disc as narrow rings of high temperatures in the direction of sliding. They can move along the radial direction during braking, according to the evolution of the bearing surface.
- Macroscopic hot spots are large thermal gradients regularly distributed on the disc surfaces. This phenomenon reduces drastically the contact surface area with high local temperatures.
- Regional hot spots are low thermal gradients on the whole disc surfaces because of inhomogeneous cooling. Such distributions appear at the end of braking due to thermal diffusion.

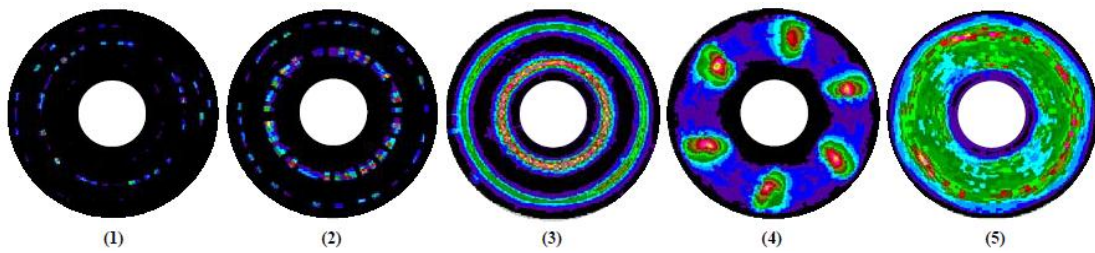
<sup>15</sup> Meyer: Brake judder - excitation and transmission mechanism, 2005, p.7.

<sup>16</sup> Anderson and Knapp: Hot spotting in automotive friction systems, 1990, p.320–321.

<sup>17</sup> Panier et al.: Hot spots in railway disc brakes, 2004, p.765.

Table 1-2: Classification of hot spot types<sup>17</sup>

	Width (mm)	Temperature (°C)	Duration
Asperity (type 1)	<1	1200 (peak)	<1 ms
Gradients on hot bands (type 2)	5–20	650–1000	0.5–10 s
Hot bands (type 3)	5–50	800	>10 s
Macroscopic hot spots (type 4)	40–110	1100 (peak)	>10 s
Regional hot spots (type 5)	80–200	20–300	>10 s

Figure 1-3: Thermographic illustrations of the five hot spot types<sup>18</sup>

The most damaging thermal gradients are the types 2, 3 and 4<sup>17</sup>. The high-order hot judder, which is the object of this work, is associated with the type 2 and 4.

### 1.3 The whole process of hot judder

Hot judder in passenger cars can be divided into four separate phases: cause, effect, transfer, and driver interface, as shown in Figure 1-4. During braking DTV and LRO firstly cause variation of the axial clamping force, and by this fluctuation of circumferential friction force between disc and pads is generated. Variations of the axial clamping force and the circumferential friction force further lead to BPV and BTV separately. However, the  $\mu$ -variation can only contribute to the fluctuation of the circumferential friction force and thus only influences BTV. Generally the generation and development of DTV, LRO and  $\mu$ -variation are considered as the causes of hot judder, whereas BPV and BTV are regarded as their effects in wheel brakes.

Via various vehicle systems, BTV and BPV are transmitted to the driver interface afterwards and they are perceived by the driver as interferences. The processes in the third frame of Figure 1-4 present the three transfer paths of hot judder. BPV is mainly transmitted by the hydraulic braking system. It is firstly transmitted to the master cylinder via the hydraulic connection of brake fluid in the brake lines and finally transmitted to the brake pedal through the mechanical components in between. The transmission of

<sup>18</sup> Dufrénoy and Brunel: Thermal localizations in friction brakes, 2008

BTV on the one hand causes brake force variation at the tire/road interface, leading to longitudinal vibration of the knuckle due to the force balance between the brake force and the hub force in the vehicle's longitudinal direction; on the other hand, it directly causes knuckle vibrations via the brake caliper (for fixed calipers) or the brake caliper bracket (for fist calipers). Thereafter, vibrations of the knuckle are respectively transmitted to the car body through the spring, damper and various links of the suspension system, and to the steering wheel via the steering system. Moreover, the brake pedal pulsation and steering wheel oscillation can also be influenced by the car body vibrations.

In the case of high-order hot judder, low-frequency drone noises normally occur at the disc/pads interfaces due to the variation of brake power. Sometimes, the vibrations of some vehicle interior components (especially the resonance of the dashboard) can also be excited by the high-order hot judder, which radiate some noises as well<sup>19</sup>.

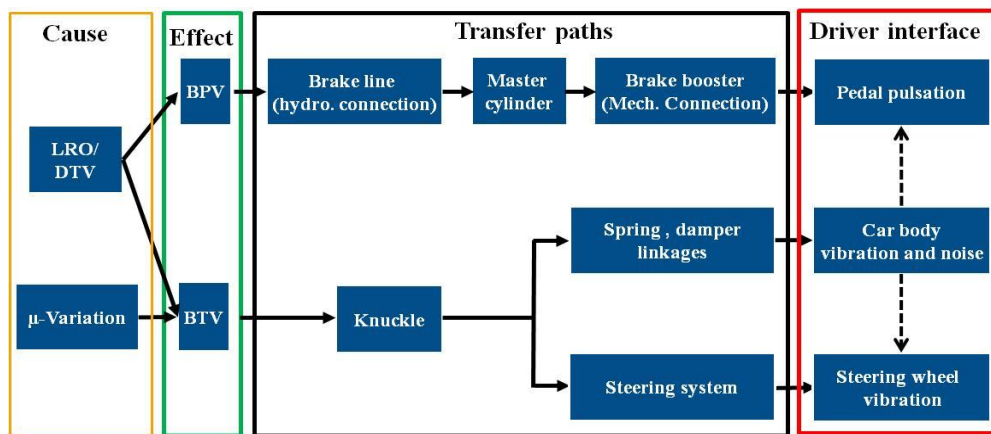


Figure 1-4: Causes, effect, transfer paths, and driver interface of brake judder

The vibrations and noises caused by hot judder might impair the driver' and passengers' subjective feeling of comfort and safety. Besides, in some critical conditions hot judder can also lead to disc crack due to the high temperature gradients und the formation of martensite<sup>20</sup>. These vibrations and noises as well as the disc crack are the main reasons for customer complaints about hot judder.

## 1.4 Motivation

In the last decades, a lot of hot judder tests have been carried out by different authors. A statistic of 23 tests found in the literature is summarized in Table A-1 of Appendix A, including the number of hot spots, the test equipment, the main test design and et al.

<sup>19</sup> Kreitlow et al.: Vibration and "hum" of disc brakes, 1985, p.1431.

<sup>20</sup> Anderson and Knapp: Hot spotting in automotive friction systems, 1990, p.322–326.

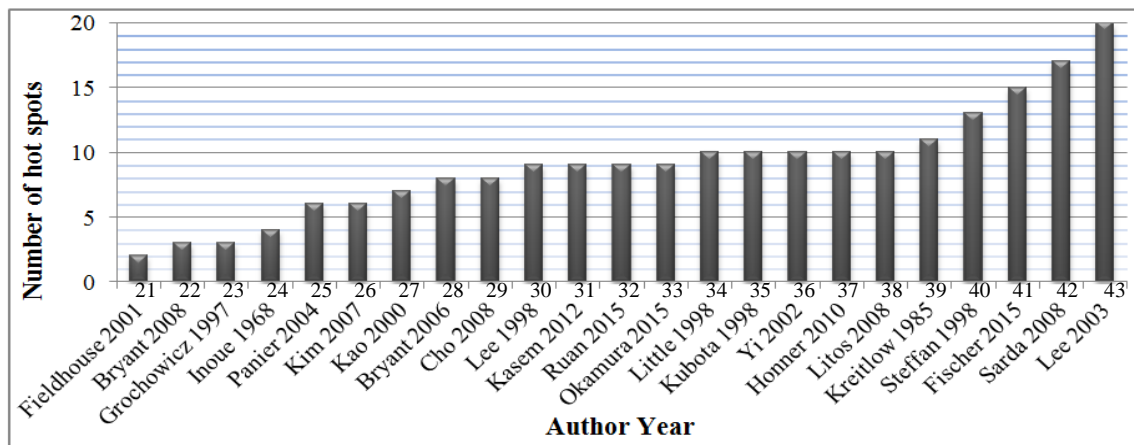


Figure 1-5: The number of hot spots testified by different authors in the literature

- <sup>21</sup> Fieldhouse and Beveridge: An experimental investigation of hot judder, 2001, p.3–4.
- <sup>22</sup> Bryant et al.: Thermal brake judder investigations, 2008, p.3–5.
- <sup>23</sup> Grochowicz: Bremsdruck- und Bremsmomentschwankungen, 1995, p.60–61.
- <sup>24</sup> Inoue: Brake judder caused by thermal deformation, 1986, p.215–216.
- <sup>25</sup> Panier et al.: Hot spots in railway disc brakes, 2004, p.765.
- <sup>26</sup> Kim et al.: Pressure change and variation of vibration due to hot spot, 2007, p.3.
- <sup>27</sup> Kao and Richmond: Brake disc hot spotting and thermal judder, 2000, p.294.
- <sup>28</sup> Bryant et al.: Discussion of characteristics of brake judder, 2006, p.2.
- <sup>29</sup> Cho: Thermo-elastic behavior of automotive disk brake, 2008, p.80–81.
- <sup>30</sup> Lee and Dinwiddie: Conditions of frictional contact in disk brakes, 1998, p.2.
- <sup>31</sup> Kasem et al.: Relationships between surface thermal gradients and disc distortion, 2012, p.175–177.
- <sup>32</sup> Ruan et al.: Bench test of friction-induced hot spots, 2015, p.312–314.
- <sup>33</sup> Okamura: Deformation of brake discs, 2015, p.298–299.
- <sup>34</sup> Little et al.: A dynamometer investigation of thermal judder, 1998, p.85–86.
- <sup>35</sup> Kubota et al.: Mechanism causing high-speed brake judder, 1998, p.133.
- <sup>36</sup> Yi et al.: TEI in automotive disc brakes, 2002, p.14.
- <sup>37</sup> Honner et al.: Frictionally excited TEI and suppression of its exponential rise, 2010, p.436.
- <sup>38</sup> Litos et al.: A measuring system for research on thermomechanical coupling, 2008, p.1254–1256.
- <sup>39</sup> Kreitlow et al.: Vibration and “hum” of disc brakes, 1985, p.1433.
- <sup>40</sup> Steffen: Hotspotbildung bei Pkw-Bremsscheiben, 1998, p.17.
- <sup>41</sup> Fischer et al.: Ordnungsanalyse von Heißrubbeln, 2015, p.11–15.
- <sup>42</sup> Sardá: Wirkungskette von Hotspots und Heißrubbeln, 2009, p.54–77.
- <sup>43</sup> Lee and Brooks: Hot spotting in aluminum drum brakes, 2003, p.45–49.

The number of hot spots is various in different brakes and sometimes also varies under different braking conditions<sup>44</sup>, or even changes during one braking application<sup>45</sup>. Figure 1-5 shows the maximum numbers of hot spots found in the 23 tests.

Because high number (> 5, typically around 10) of hot spots was detected by most of the authors, the generation and development mechanisms of the high dominant order have been almost the exclusive focus for the hot judder researchers. However, considering a typical occurring scenario for brake judder, leaving the German Autobahn by decelerating from 180 to 80 km/h, the vibrations excited by the cold judder with 1<sup>st</sup> to 4<sup>th</sup> orders are approximately from 100 to 10 Hz<sup>46</sup>, while the vibrations caused by the high-order hot judder with 10<sup>th</sup> to 20<sup>th</sup> order are between 500 and 100 Hz. According to Zeller (Figure 1-6)<sup>47</sup>, low-frequency oscillations up to ca. 50 Hz are normally perceived as vibrations, while high-frequency oscillations from 100 Hz to ca. 1000 Hz only play a role if airborne sounds are excited. In the transition zone from 20 to 100 Hz, the oscillations are normally both audible and palpable, which is called harshness.

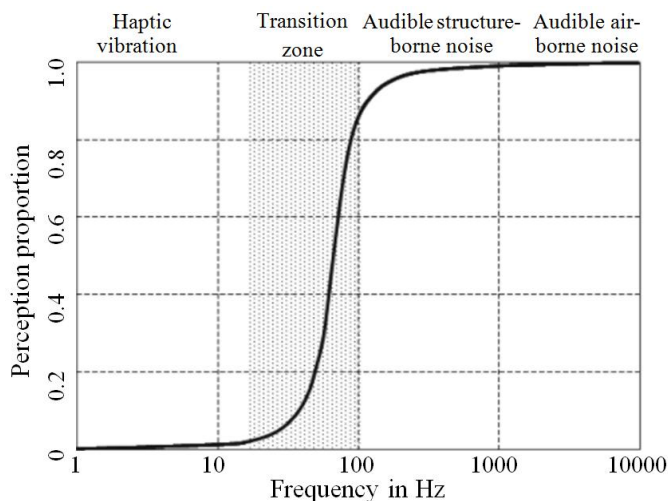


Figure 1-6: Vibro-acoustic perception range<sup>47</sup>

On the one hand, the transfer behaviors and the influences of the vibrations caused by cold judder that happen in the transition zone have been already well investigated by means of testing and simulation in the last decades. On the other hand, the transfer behaviors and the impacts of the high-order hot judder that occurs in a higher frequency range still remain totally unclarified. Specifically, it is still not well known whether the vibrations and noises caused by the high-order hot judder can be transferred to and be

---

<sup>44</sup> Fischer et al.: Ordnungsanalyse von Heißrubbeln, 2015, p.12–16.

<sup>45</sup> Ruan et al.: Bench test of friction-induced hot spots, 2015, p.314.

<sup>46</sup> cf. Meyer: Brake judder - excitation and transmission mechanism, 2005, p.1.

<sup>47</sup> Zeller et al.: Handbuch Fahrzeugakustik, 2012, p.22.

perceived by the driver at all, or under which conditions and in which form can the high-order hot judder be perceivable to the driver and the passengers and thus lead to customer complaint. Therefore, the ultimate objective of this work is to investigate the transfer behaviors of the high-order judder and the influences of the high-order judder induced vibrations and noises on the driver's subjective perception.

Furthermore, because the inspection and prevention of hot judder have been chiefly the tasks in the development phase of friction system, when the complete vehicle test is not possible or practical<sup>48</sup>, and plus the difficulties of applying some sensors (e.g. displacement sensors and thermal camera) as well as the controlling of the braking conditions in vehicle tests, hot judder tests have been mostly carried out at brake dynamometers. Only a few vehicle tests have been executed in the last decades (e.g. only four of the 23 tests in Table A-1). Moreover, currently there is still no unified test equipment or test program (see the test design in Table A-1) for hot judder detection. Regarding the test apparatus, both vehicle test and dynamometer test are being used and the types of vehicle test and dynamometer test are also various. The possible test types of hot judder as well as their main features are shown in Table 1-3.

Vehicle test can be carried out on test tracks or with chassis dynamometers. Comparing with the vehicle road test, chassis dynamometer test has the advantage that the brake pressure can be precisely controlled, but it has the disadvantage that the braking system of the vehicle needs to be modified by connecting it with the control system of the dynamometer. Besides, the movement of the vehicle is also constrained during chassis dynamometer tests, thus chassis dynamometer test is not appropriate for investigating the whole car body vibrations caused by hot judder.

Table 1-3: Various test types of hot judder<sup>49</sup>

Equipment types		Feature
Vehicle test	road test	trying to keep a constant pedal position by the driver; influenced by other road excitations
	chassis dyno test	brake pressure control by the dyno; changed layout of braking system; constrained vehicle movements
Dyno test	inertia dyno	vehicle weight is simulated with inertia mass; stop braking applications are possible
	simple dyno	no inertia mass thus deceleration is not possible; only acceleration and drag braking are possible

<sup>48</sup> Anderson and Knapp: Hot spotting in automotive friction systems, 1990, p.336.

<sup>49</sup> cf. The test equipments used by the authors in Figure 1-5.

In the dynamometer tests, typically only the wheel brake, the knuckle, the hub and the hub axis are mounted, but sometimes the ¼ car suspension assembly is also applied<sup>22</sup>. Normally the brake dynamometer has inertia masses simulating the vehicle weight, which makes the stop braking application possible. However, simple dynamometers that are without inertia masses were also used by some authors<sup>21,22,26,29</sup>. At such dynamometers, only drag braking applications with constant rotational speed or tests with varying velocity by acceleration instead of deceleration are possible.

With respect to the test program, the vehicle road test is normally executed by experienced drivers, trying to keep the brake pedal at a constant position with the help of real-time display of the brake pressure or the deceleration. As for the test procedure at both chassis dynamometer and brake dynamometer, drag braking and stop braking applications are normally carried out with different control strategies, as summarized in Table 1-4. For example, drag braking can be executed with a constant rotational speed and a constant brake pressure, starting and finishing with defined initial and final disc temperatures; stop braking can be carried out by accelerating to an aimed initial velocity, drag braking with this velocity to a defined initial disc temperature, and then decelerating with a constant deceleration to a wanted final velocity. As seen from Table A-1, the control parameter as well as the rotational speeds/initial speeds adopted by different authors show great discrepancies.

Table 1-4: The typical test programs of hot judder

Braking types	Control parameter	Variable parameter	Trigger signal
<b>Drag braking</b>	pressure (5 - 30 bar), torque	rotational speed, initial disc temperature	initial and final disc temperature
<b>Stop braking</b>	deceleration(0.1 - 0.5 g), pressure (5 - 30 bar), torque	initial and final velocities, initial disc temperature	initial disc temperature, inertial and final velocities

Up to now there is no direct comparison among different types, especially between dynamometer test and vehicle test. Whether hot judder behaves similarly or totally differently in different test types or under different test conditions has also been not well known. In order to investigate the transfer behaviors of the high-order hot judder and its influences on the driver, the incidence of the high-order hot judder in the vehicle tests and the transferability of hot judder tests from the brake dynamometer to the real vehicle need to be clarified as well.



---

## 2 State of the art

State of the art regarding the overall process of high-order hot judder: the mechanisms, the transfer behaviors, as well as the human responses to the vibrations and noises caused by the high-order judder, are introduced in sequence in this chapter.

### 2.1 Mechanisms of high-order hot judder

The emerging mechanism of high-order hot judder is not unique. Various theories are raised by different researchers, explaining the occurrence and evolution mechanisms.

#### 2.1.1 Cause and effect chain found by Sardá

Sardá provided a general cause and effect chain of the high-order hot judder, as illustrated in Figure 2-1. Hot judder occurs during light to moderate braking from higher speeds to lower speeds. On the one hand, the heat generated at the disc surfaces are transferred into the disc inside. Due to the presence of cooling channels, the temperature gradient in the disc's axial direction is established. As a result, the brake disc cannot expand uniformly, the thermal stress is formed and a waved deformation of the disc is generated. The wave-like disc leads to an inhomogeneous brake pressure distribution between the disc and pads, which further causes inhomogeneous temperature distribution in the circumferential direction. In return, the inhomogeneous temperature distribution intensifies the disc waviness and thus the dynamic LRO is formed. Because the troughs and crests of the waviness are not uniform in the disc's circumferential direction, the thermal localizations near the crests are also not homogenous, by which the dynamic DTV is induced. Hot spots are the results of the thermal localizations around the crests. "Dynamic" LRO or DTV means that this DTV or LRO will disappear when the disc cools down after the braking application.

On the other hand, due to the hot spots and inhomogeneous pressure distribution, unbalanced thermo-mechanical stress is brought about. Under this unbalanced thermo-mechanical stress, a metallurgical transformation of disc materials around the hot spots would happen, known as martensite formation. Martensite occupies a greater volume than the parent metal<sup>50</sup> and therefore causes static LRO/DTV. The micro-structural transformation is not reversible and speckles remain visible on the disc surfaces even

---

<sup>50</sup> Day et al.: Thermal effects and pressure distributions, 1991, p.203–204.

when the disc cools down (see Figure 2-2). Due to the material changes on the disc surfaces and the dependence of the friction coefficient on the contact pressure and especially on the surface temperature<sup>51</sup>, variation of friction coefficient ( $\mu$ -variation) on the friction rings of the brake disc may emerge. In disc brakes, the dynamic and static LRO/DTV combined with the  $\mu$ -variation lead to BTV and BPV afterwards.

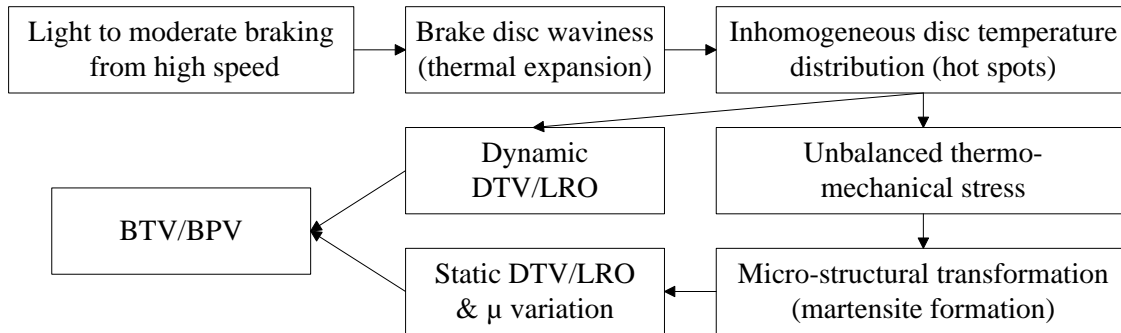


Figure 2-1: Cause and effect chain of hot judder based on Sardá<sup>52,53,54,55</sup>



Figure 2-2: One brake disc with “hot spots” under cold status<sup>56</sup>

This theory basically explained the occurring process of hot judder, but the specific number of hot spots generated under defined test conditions was not clarified.

## 2.1.2 TEI

Thermo-elastic Instability (TEI) is a theory used by the most hot judder researches, trying to determine the occurring conditions (critical speed) of hot judder and the specif-

<sup>51</sup> Kreitlow et al.: Vibration and “hum” of disc brakes, 1985, p.1436.

<sup>52</sup> cf. Sardá: Wirkungskette von Hotspots und Heißrubbeln, 2009, p.76–87.

<sup>53</sup> cf. Sardá et al.: Wirkungskette der Entstehung von Hotspots, 2008, p.13–20.

<sup>54</sup> cf. Sardá et al.: Investigation of hot spots and thermal judder, 2008, p.5–7.

<sup>55</sup> cf. Fischer et al.: Effects of different friction materials on hot judder, 2013, p.1–2.

<sup>56</sup> Sardá et al.: Investigation of hot spots and thermal judder, 2008, p.4.

ic number of hot spots. The instability, which results from the interaction of frictional heat generation, thermo-elastic distortion and elastic contact, is known as TEI<sup>57,58,59</sup>.

The basic mathematical function of TEI is the coupling between the mechanical and thermal problem by the energy balance relation<sup>60</sup>

$$q(x, y, t) = \mu v p(x, y, t) \quad (2.1)$$

where  $x$  and  $y$  are the coordinate position on the contact surface,  $q(x, y, t)$  is the frictional heat distribution,  $p(x, y, t)$  is the contact pressure distribution, and  $v$  is the sliding speed of disc. For this equation, there is generally a critical speed  $v_{critical}$ <sup>61</sup>, above which non-uniform perturbations in the temperature will grow, leading to a characteristic pattern of hot spots or hot bands on the brake disc<sup>62</sup>. For the continuous contact with plane strain, the critical speed of a conductive surface sliding against a rigid nonconductive surface is linearly proportional to the wave number  $h$  per  $2\pi$  of length (comparable with the judder order)<sup>63,64</sup>:

$$v_{critical} = \frac{2\kappa h(1-\nu)}{E\chi\mu} \quad (2.2)$$

where  $\kappa$  is the thermal conductivity,  $E$  is the Young's modulus,  $\nu$  is the Poisson's ratio,  $\chi$  is the coefficient of thermal expansion.

Considering the basic geometries of brake components, two methods are applied to determine the dominant order of hot judder: Yi's FEM calculation and Graf' stability chart method. In Yi's method, the temperature filed in a cylindrical polar coordinate system  $(r, \varphi, z)$  is expressed by the form<sup>65</sup>

$$T(r, \varphi, z, t) = R\{e^{bt}\Theta(r, \varphi, z)e^{bt}\} \quad (2.3)$$

where  $\Theta$  is the nodal temperatures and  $b$  is a complex exponential growth rate. If this form is substituted into the various governing equations and boundary conditions of the feedback process of TEI, the FEM problem can be transformed into a linear eigenvalue

<sup>57</sup> Lee and Barber: Frictionally excited TEI in automotive disk brakes, 1993, p.607.

<sup>58</sup> Barber: Influence of thermal expansion on the friction and wear, 1967, p.157.

<sup>59</sup> Barber: TEI in the sliding of conforming solids, 1969, p.385.;

<sup>60</sup> Yi et al.: TEI in automotive disc brakes, 2002, p.188.

<sup>61</sup> Dow and Burton: TEI of sliding contact in the absence of wear, 1972, p.315–328.

<sup>62</sup> Yi et al.: TEI in automotive disc brakes, 2002, p.188.

<sup>63</sup> Burton et al.: Thermoelastic instability in a seal-like configuration, 1973, p.177–188.

<sup>64</sup> Yi et al.: FEA of TEI in intermittent sliding contact, 2014, p.872.

<sup>65</sup> Yi et al.: TEI in automotive disc brakes, 2002, p.190.

problem of  $b$ . And  $b$  can be calculated for each given judder order  $N$ . The order that leads to an eigenvalue  $b$  with positive real part is then considered as the dominant order, because any slightly perturbed initial condition could result in great temperature perturbations increasing in exponential form<sup>65</sup>.

In Graf's method, the critical speeds for each given hot spot number (hot spot magnitude in the circumferential direction) and for each given wavelength in the radial direction (hot spot magnitude in the radial direction) are calculated, which yields the stability chart, as shown in Figure 2-3. The dominant thermal modes on the disc surfaces for hot band and hot spot are thought to be the orders that have local minimal critical sliding velocities; and the magnitudes of hot bands and hot spots (in sine forms) in the radial direction are determined by the wavelength under which the minimal critical sliding velocities are reached<sup>66</sup>. For example, in Figure 2-3, the dominant order of hot spots was thought to be the 6<sup>th</sup> order and the critical sliding speed for both hot band and hot spots are approximately 9.1 m/s, which corresponds to a vehicle velocity of 98 km/h.

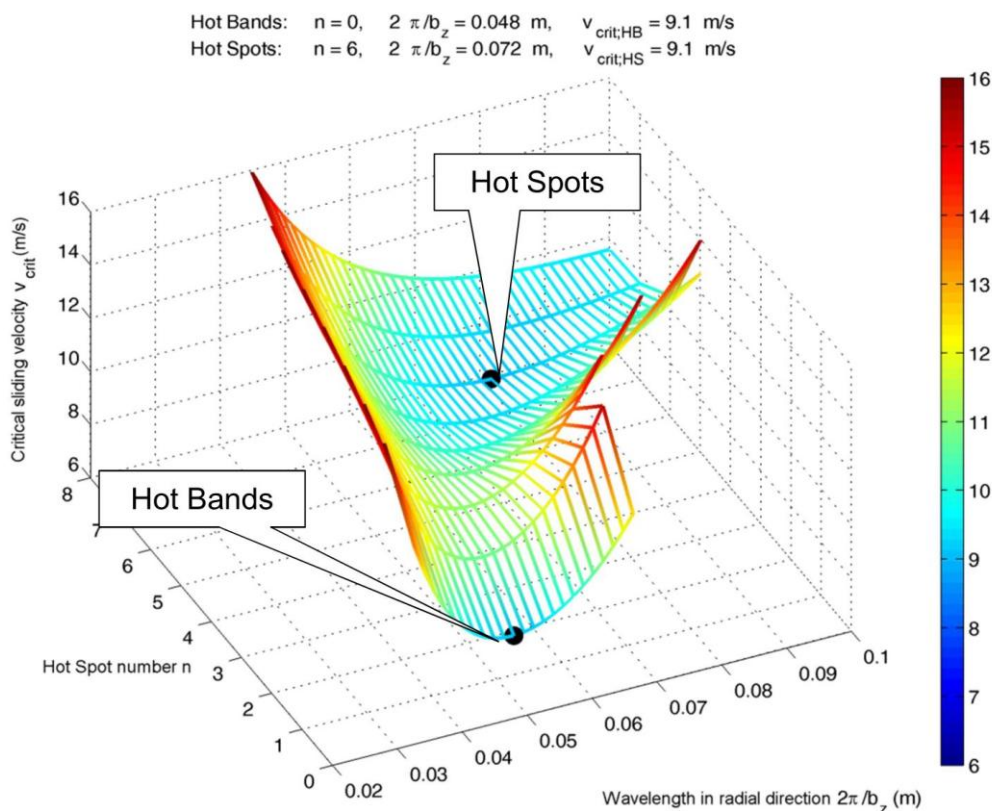


Figure 2-3: Stability chart of Graf<sup>66</sup>

However, according to Barber, there could be more orders with critical speeds that are under the possible sliding speed and are with exponential growth rates possessing posi-

<sup>66</sup> Graf and Ostermeyer: Efficient computation of hot bands and hot spots, 2013

tive real parts. In this case, it is assumed that the mode with the highest exponential growth rate is expected to dominate the transient process<sup>67</sup>.

In the light of TEI, parameter study is possible with respect to the critical sliding velocity<sup>68,69,70,71,72</sup>. However, TEI is not valid for all the hot judder phenomena, e.g. it was not validated in the Sardá's tests<sup>73</sup>.

### 2.1.3 PWD

Panier et al. gives an explanation for the formation mechanism of the hot judder that mainly possesses six hot spots in railway brakes. It is named as “Progressive Waviness Distortion” (PWD) and three steps are defined for the hot judder evolution<sup>74</sup>:

#### Step 1: two-wave disc bending

- Considering that the brake disc is asymmetrically fixed on the hub, the thermal loading from the frictional contact between the disc and its pads is also asymmetric. Therefore, radial and angular moments are induced and the disc bends with a warped deformation of two troughs and ridges, as shown in Figure 2-4.

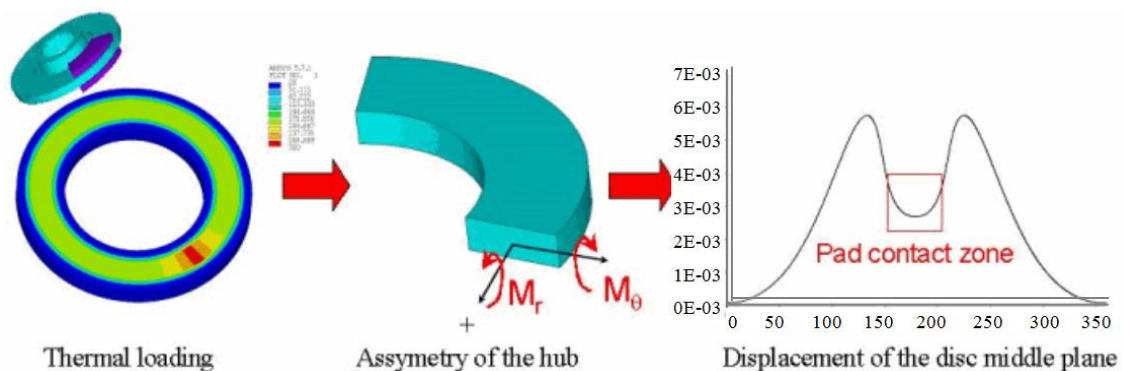


Figure 2-4: Step 1 of PWD<sup>75</sup>

<sup>67</sup> Barber: Frictionally Excited TEI, Internet source, accessed at 15 April.2016.

<sup>68</sup> Lee and Barber: Frictionally excited TEI in automotive disk brakes, 1993, p.612–614.

<sup>69</sup> Graf and Ostermeyer: Efficient computation of hot bands and hot spots, 2013, p.6–9.

<sup>70</sup> Hartsock and Fash: Effect of pad/caliper stiffness on TEI, 2000, p.512–517.

<sup>71</sup> Hartsock et al.: Parametric analyses of TEI in disc brakes, 1999, p.521–524.

<sup>72</sup> Kao et al.: Predictive techniques to study TEI of brakes, 1994

<sup>73</sup> Sardá: Wirkungskette von Hotspots und Heißrubbeln, 2009, p.91–94.

<sup>74</sup> Panier et al.: Progressive waviness distortion, 2004, p.52–54.

## Step 2: transition from two waves to a higher number of waves and warpage

- If the thermal loading is high enough, plastic flow occurs and distortions become stationary on the disc. The disc is then submitted to two skew-asymmetric thermal gradients per side. Under this loading, the distortion of the disc gives six troughs and ridges leading to six hot spots. This whole process is illustrated in Figure 2-5.

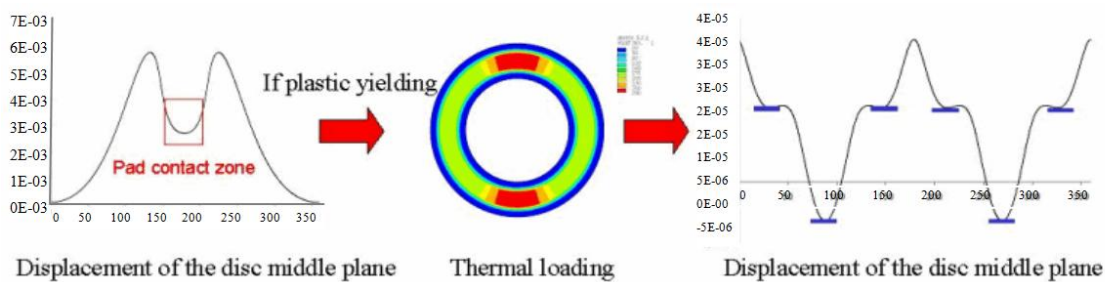


Figure 2-5: Step 2 of PWD<sup>76</sup>

## Step 3: hot spot stabilization

- With the thermal loading on the six hot spots, plastic yielding occurs on the troughs leading to stationary hot spot.

PWD approach shows that the formation of hot spots strongly depends on plastic yield of the disc material, and the number of hot spots is greatly influenced by the contact conditions between the disc and the pads, which is mainly decided by the pad structure and materials (e.g. stiffness and length of pad)<sup>77</sup>. According to the theory of PWD, hot spots are always at the same positions in the following braking applications<sup>78</sup>. However, this theory was also not validated in the tests of Sardá by using passenger car brakes, in which positions of hot spots alternated in the subsequent braking application<sup>73</sup>.

### 2.1.4 Hot judder caused by resonance frequency

Dynamometer test results of Fischer show that hot judder frequency is closely combined with a resonance frequency of the wheel brake. The number of hot spots (or hot judder

<sup>75</sup> Panier et al.: Progressive waviness distortion, 2004, p.53.

<sup>76</sup> Panier et al.: Progressive waviness distortion, 2004, p.54.

<sup>77</sup> Panier et al.: Hot spots in railway disc brakes, 2004, p.769-771.

<sup>78</sup> Panier et al.: Hot spots in railway disc brakes, 2004, p.767.

order) varies with changing rotational speed of the brake disc, while the induced vibration frequency keeps relatively constant (see Figure 2-6).

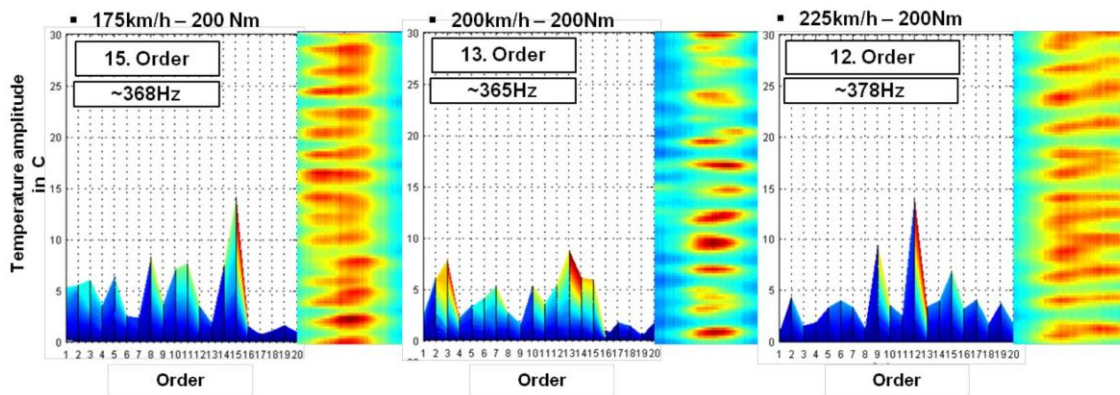


Figure 2-6: Variation of hot spots with changing velocities for three drag braking applications<sup>79</sup>

### 2.1.5 Hot judder caused by cooling vent

It is testified by Bryant et al. that the cooling vent of the brake disc can cause circumferential temperature gradients and thus leads to high-order hot judder. Figure 2-7 shows that the vent profile is influencing the temperature distribution on the disc surface, with a recorded temperature variation of 16.2°C and the number of peaks in the temperature profile correlates exactly with the number of disc vents<sup>80,81</sup>. Besides, according to the simulation result of Tang<sup>82</sup>, the vent pattern has also strong influence on the distribution and intensity of hot spots.

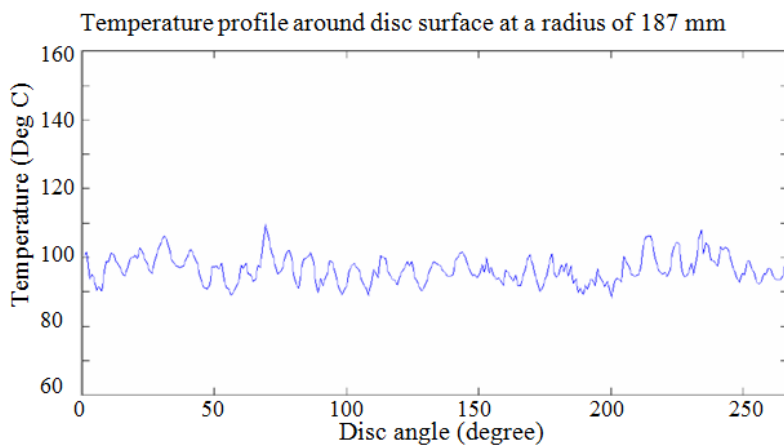


Figure 2-7: Temperature profile at the disc surface correlates with the number of hot spots<sup>81</sup>

<sup>79</sup> Fischer et al.: Ordnungsanalyse von Heißrubbeln, 2015, p.15.

<sup>80</sup> Bryant et al.: Thermal brake judder investigations, 2008, p.5–6.

<sup>81</sup> Bryant et al.: Thermo-elastic and thermo-plastic effects, 2011, p.69.

<sup>82</sup> Tang et al.: A 3D FE simulation of hot spotting, 2016

Furthermore, it is manifested by Tang that for the two-piece ventilated brake discs, the mounting pins can also give rise to hot spots and thus could lead to the high-order hot judder. His simulation result demonstrated that at the end of the braking event ( $t = 24$  s), 17 hot spots were clearly developed which correlate with the number and position of the mounting pins, as displayed in Figure 2-8. In addition, it is further suggested by his simulation that the elastic modulus and the heat capacity of the pins have evident influences on the intensity of hot spots<sup>82</sup>.

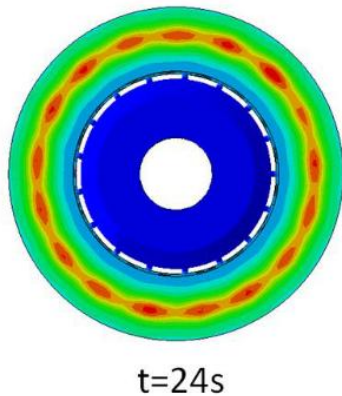


Figure 2-8: Simulation result of Tang with a two piece ventilated brake disc<sup>82</sup>

### 2.1.6 Influential factors of hot judder occurrence

In spite of the theories introduced above, there are still no universally applicable design rules for hot judder prevention. Nowadays, the most efficient way to reduce hot judder occurrence is still the parameter sensitivity analysis for specific brakes by means of testing and simulation. Table 2-1 lists some already testified influential factors, categorized by the three main wheel brake components: the disc, the pad, and the caliper.

Although the effect of certain parameters (e.g. the compressibility of brake pad) coincides among different authors, it also might vary for some other parameters. For example, according to Kubota and Panier, shorter pad length will lead to higher number of hot spots; however, there is no specific correlation between pad length and hot spot number in the tests of Sardá. With respect to the influential parameters from the brake caliper (the stiffness of caliper and hydraulic system), the conclusions were drawn by simulations with constant given DTV values. The results are only the mechanical transformations from DTV to BTV via the caliper. The influences of the caliper characteristics on hot judder propensity (the occurrence of hot spots or the thermal increase of DTV) were not verified.



Table 2-1: Influential factors of brake components on hot judder

Component	Parameter	Influence
Disc	thermal conductivity	higher thermal conductivity → lower hot judder intensity <sup>83</sup>
	diameter	larger disc → higher hot spots number <sup>84</sup>
	thickness	thicker discs → lower hot judder intensity <sup>84</sup>
	material	hot judder is more likely to happen for aluminum discs than grey iron discs <sup>84</sup>
	connection disc/cup	lower connection stiffness → higher hot judder intensity <sup>84</sup> optimized connecting form greatly reduces hot judder <sup>85</sup>
	coning	higher coning → higher thermal BTV <sup>86</sup>
	vent and pin	the number of vent and pin correlates with the number of hot spots <sup>80,81,82</sup>
Pad	coefficient of friction	lower $\mu$ → lower hot judder propensity <sup>87</sup>
	elastic modulus	lower elastic modulus → lower hot judder propensity <sup>87</sup>
	thermal conductivity	higher thermal conductivity → lower hot judder propensity <sup>87</sup>
	compressibility	more compressible → lower hot judder propensity <sup>88,89,90</sup>
	damping	higher damping → lower hot judder intensity <sup>90</sup>
	length	shorter pads → lower hot judder propensity <sup>83,87,89</sup> shorter pads → higher hot spot number <sup>83,91</sup> pad length has no correlation with hot spot number <sup>89</sup>
	thickness	thicker pads → lower hot judder intensity <sup>83</sup>
Caliper	caliper stiffness	stiffer caliper → higher hot judder intensity <sup>92</sup>
	hydraulic stiffness	stiffer hydraulic system → higher hot judder intensity <sup>93</sup>

<sup>83</sup> Kubota et al.: Mechanism causing high-speed brake judder, 1998, p.135–137.

<sup>84</sup> Steffen: Hotspotbildung bei Pkw-Bremsscheiben, 1998, p.12–25.

<sup>85</sup> Inoue: Brake judder caused by thermal deformation, 1986, p.219.

<sup>86</sup> Cho et al.: Pad properties and disc coning on high speed judder, 2012, p.2–6.

<sup>87</sup> Lee and Dinwiddie: Conditions of frictional contact in disk brakes, 1998, p.6–11.

<sup>88</sup> Little et al.: A dynamometer investigation of thermal judder, 1998, p.83–88.

<sup>89</sup> Sardá: Wirkungskette von Hotspots und Heißrubbeln, 2009, p.71–76.

<sup>90</sup> Fischer et al.: Ordnungsanalyse von Heißrubbeln, 2015, p.18.

<sup>91</sup> Panier et al.: Hot spots in railway disc brakes, 2004, p.770–771.

<sup>92</sup> Augsburg et al.: Untersuchungen zum Rubbelverhalten, p.29.

<sup>93</sup> Herkenrath: Bremsmomentenschwankungen, 2005

Besides, as pointed out by Schlecht, in many circumstances, the reduction of brake judder by modifying some certain parameters could bring negative influences to the brake performance (the braking response characteristics, the volume consumption, the brake pedal feeling, and et al.)<sup>94</sup>. For each wheel brake system, an optimal compromise between the mitigation of the brake induced NVH problems and the fundamental braking performance needs to be ascertained.

## 2.2 Transfer behaviors of brake judder

Up to now the transfer behaviors of hot judder, especially the high-order hot judder, have been still not investigated. However, a lot of researches about the transfer behaviors of cold judder have been carried out by means of vehicle tests and/or simulations.

### 2.2.1 Vehicle tests by Engel

Engel investigated the transfer behaviors from the BTV caused by the 1<sup>st</sup> order cold judder and the tire imbalance force to the steering wheel. Four lower middle-class vehicles and two upper middle-class vehicles all possessing MacPherson front axle were tested through vehicle road tests. Figure 2-9 shows the test setup and the measured quantities used in his investigation.

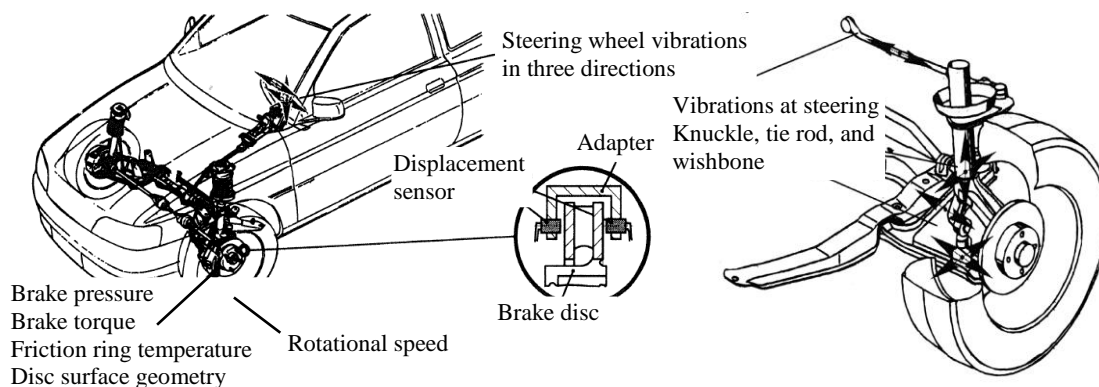


Figure 2-9: The test setup and the measured quantities used by Engel<sup>95</sup>

The transfer behaviors were studied by defined Global Transfer Functions (GTF) and Local Transfer Functions (LTF). GTF is the global transfer of cold judder and the tire imbalance force from the wheel brake to the steering wheel. LTF is the expression of the concrete transfer behaviors of the components in the transfer paths. Three LTFs were

<sup>94</sup> Schlecht: Minimierung der Schwingungsempfindlichkeit, 2012, p.27.

<sup>95</sup> Engel: Systemansatz zur bremsenregter Lenkunruhe, 1998, p.31.

used by Engel: the tire imbalance force → the vibration of steering knuckle → the vibration of the tie rod → the circumferential steering wheel vibration.<sup>96</sup>

The transfer behaviors differed greatly among the six vehicles under test, although they have similar wheel suspensions and steering systems. Following mitigation strategies were raised as main conclusions of the investigation<sup>97</sup>:

- Avoiding the superimposition of the resonance frequency of one subsystem with that of the whole system. For example, this could be realized by modifying the stiffness and the damping of the suspension system or by changing the rotating stiffness of the steering column and the inertia moment of the steering wheel.
- Reducing the disturbing lever arm by setting the oscillating axis of the suspension as near as possible to the articulation point of the tie rod.

## 2.2.2 MBS models

### Bitter: integrated optimization of the chassis mounts

Bitter explored the transfer behaviors and the reduction methods by optimizing the chassis mounts with the help of MBS models. Two whole vehicle models were utilized: an Audi A6 (Figure 2-10 (a)) with 4-link front suspension and an Audi A2 with MacPherson front suspension. They were both built with ADAMS/ Car. These models were directly provided by Audi AG and had already been validated regarding the driving dynamics. By comparing the simulating results with the vehicle test results with an Audi A6 2.5 V6 TDI (Figure 2-10 (b)), it was testified that the model that was valid for the driving dynamics also applied for the brake judder issue.<sup>98</sup>

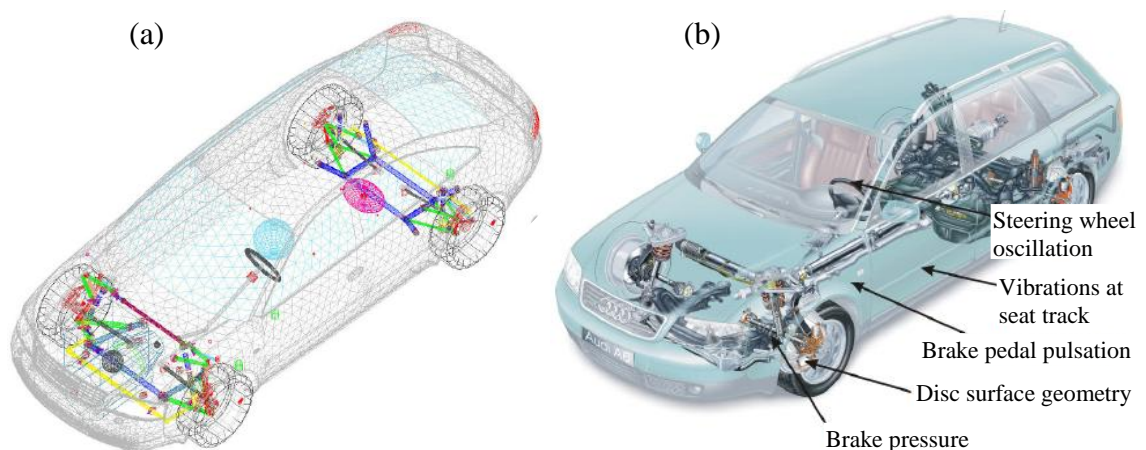


Figure 2-10: (a) The simulation model and (b) the test vehicle used by Bitter<sup>98</sup>

<sup>96</sup> Engel: Systemansatz zur bremseregter Lenkunruhe, 1998, p.54–55.

<sup>97</sup> Engel: Systemansatz zur bremseregter Lenkunruhe, 1998, p.64–71.

<sup>98</sup> Bittner: Reduzierung des Bremsrubbels, 2006, p.42–67.

The transfer behaviors of cold judder from the wheel brake to the car body and the steering wheel were investigated. Following results were obtained by the simulations with the two whole vehicle models<sup>99</sup>:

- The longitudinal direction is the dominant transfer direction. The vibration of the car body in  $X$  direction is much higher than that in  $Y$  and  $Z$  directions.
- One-side excitation (much stronger judder at one of the front brakes) is the main reason for the vehicle transverse vibration and the steering wheel oscillation.
- Vertical car body vibration also owes to the longitudinal vibration, because the vibration in the  $X$  direction will cause the axle load shifting, which further leads to the vibration in the  $Z$  direction.

Regarding the brake judder reduction measures, the conclusions were as follows<sup>100</sup>:

- The brake judder induced vibration is not transmitted through one favorable dominant path; all the paths in the chassis share the transmission. Hence it is not possible to break the transmission by only optimizing one single component in the transfer paths.
- An optimal robust chassis against brake judder can only be achieved with an optimal combination of all the chassis mounts. By this way little changes in the stiffness and damping of the chassis mounts could already make a remarkable improvement.

### **Zhang: confirming the transfer paths and optimizing the chassis mounts**

Zhang et al. confirmed the transfer path of brake judder from the wheel brake to the steering wheel: the wheel brake → the suspension → the tie rod → the steering wheel, by using Transfer Path Analysis (TPA) based on the vehicle road test results and simulation results with a whole vehicle MBS model<sup>101</sup>. The objective vehicle is configured with MacPherson front suspension, twist beam rear suspension and rack-pinion steering system. By the determined transfer functions (see Figure 2-11), the important role that the resonance frequency plays in the course of brake judder transmission was revealed. It was manifested by simulation that the stiffness of the chassis mounts (the one between the lower control arm and the sub-frame, and the one between the sub-frame and the vehicle body) had great influence on the amplitude of the resonance frequency<sup>102</sup>.

---

<sup>99</sup> Bittner: Reduzierung des Bremsrubbels, 2006, p.73.

<sup>100</sup> Bittner: Reduzierung des Bremsrubbels, 2006, p.92,124.

<sup>101</sup> Zhang et al.: Transfer path of steering wheel wobbling, 2006

<sup>102</sup> Zhang et al.: Brake judder induced steering wheel vibration, 2007, p.144–147.

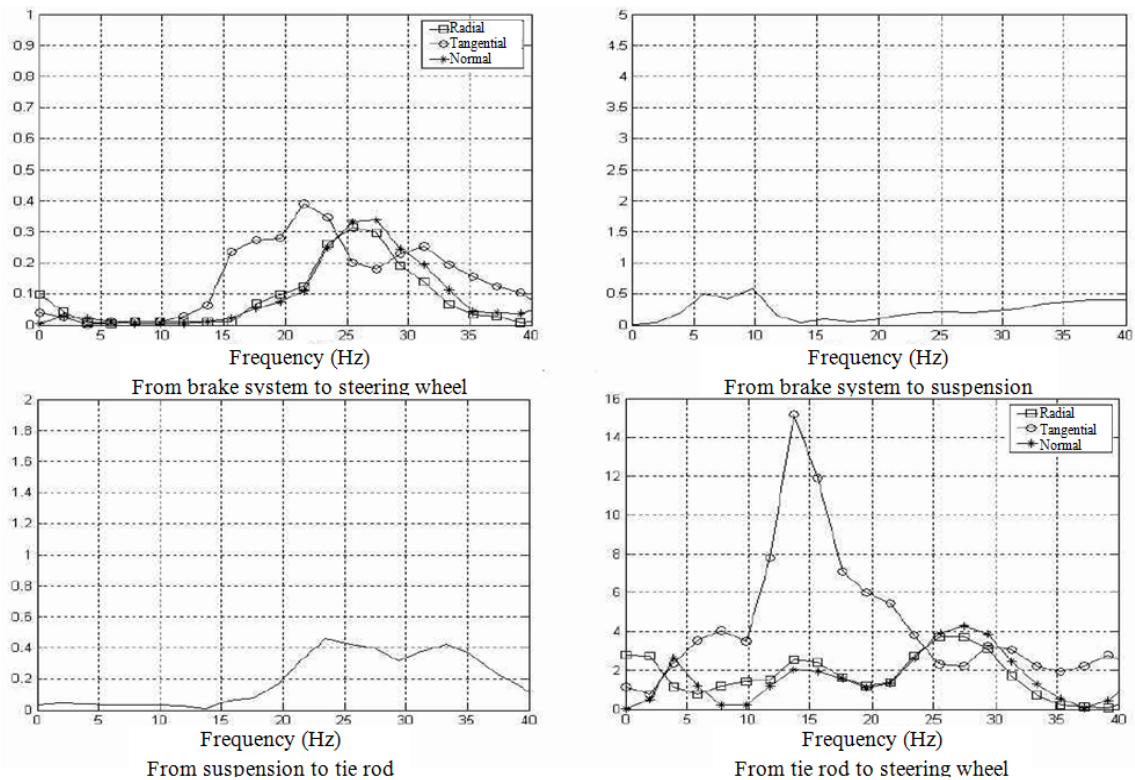


Figure 2-11: The transfer functions of brake judder in the steering system<sup>102</sup>

### Schlecht: optimization of the axle kinematics

By using a MBS whole vehicle model Schlecht optimized the kinematics (including the toe angle, the camber angle, the kingpin inclination angle, the caster angle, the trail, the king pin offset, the steering arm, the level arm of braking force, the braking support angle, the suspension oblique angle, and the longitudinal stiffness of the axle<sup>103</sup>) of the front axle of an Audi A4 regarding the 1<sup>st</sup> order cold judder and the imbalanced tire. This car was configured with 5-link front axle and Hydraulic Power Steering (HPS). The model was validated by comparing the simulation results with the test data from corresponding vehicle test carried out at the chassis dynamometer.

Besides the optimization of axle kinematics, the characteristics of the elastomeric mounts for chassis support was also modified, which presented an obvious reduction of vehicle vibration sensitivities to both the brake judder and the imbalanced tire force<sup>103</sup>.

<sup>103</sup> Schlecht: Minimierung der Schwingungsempfindlichkeit, 2012, p.81–83.

### Sim: sensitivity analysis of selected parameters

Sim studied the optimization method of brake judder transfer from the wheel brake to the steering wheel by using a whole vehicle MBS model. This model was built with MacPherson front suspension, coupled torsion beam rear suspension and rack-pinion steering system. It was validated by comparing the vibrations at the tie rod, the rack housing, and the steering wheel obtained by simulation and test. Resonance frequencies of the tie rod (15 Hz), the rack housing (1-2 Hz), and the steering wheel (15 and 40 Hz) were determined by both simulation and test. Four of the six selected design variables (the stiffness of the A-bush, the MTG-bush, the G-bush, and the damper characteristics; the positions of the bushes, see Figure 2-12) were determined to be the most influential parameters through sensitivity analysis with the objective function of steering wheel vibration. By virtual DOE of the four parameters, the optimal values were identified, and the RMS value of steering wheel vibration was reduced by 6.6% with the optimized parameters.<sup>104</sup>

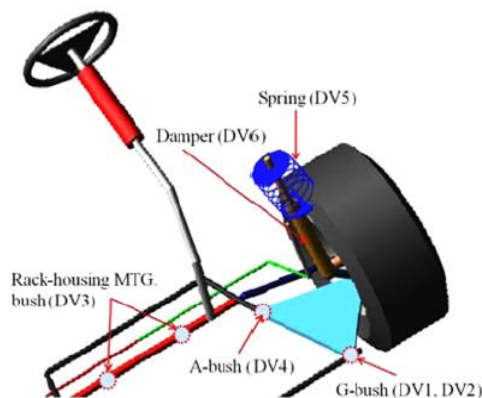


Figure 2-12: Locations of the bushings in the front suspension<sup>104</sup>

### Yu: reducing the mode coupling effect by virtual DOE

A MBS model composed of the front chassis system of a SUV with MacPherson suspension and rack-pinion HPS steering system was built by Yu et al., and the optimization measures of the front chassis design were explored regarding the transmission of the tire imbalance force and the brake judder to the steering wheel. The steering system model was confirmed by bench test<sup>105,106</sup> and the whole front chassis assembly model was validated by a specially designed laboratory test<sup>107</sup>.

---

<sup>104</sup> Sim et al.: Vibration path analysis and optimal design, 2013, p.587–594.

<sup>105</sup> Yu: Analysis of automotive HPS, 2004

<sup>106</sup> Yu et al.: Modeling and factor analysis of HPS, 2004

<sup>107</sup> Yu et al.: Chassis transmissibility: modeling and validation, 2007

The coupling of two vibration modes was detected to be decisive for the transfer in the frequency range below 20 Hz: one is the suspension fore-aft mode (Figure 2-13 (a)) and the other is the rotational mode of the steering wheel (Figure 2-13 (b))<sup>108</sup>. The mode coupling mechanism is illustrated in Figure 2-13 (c).

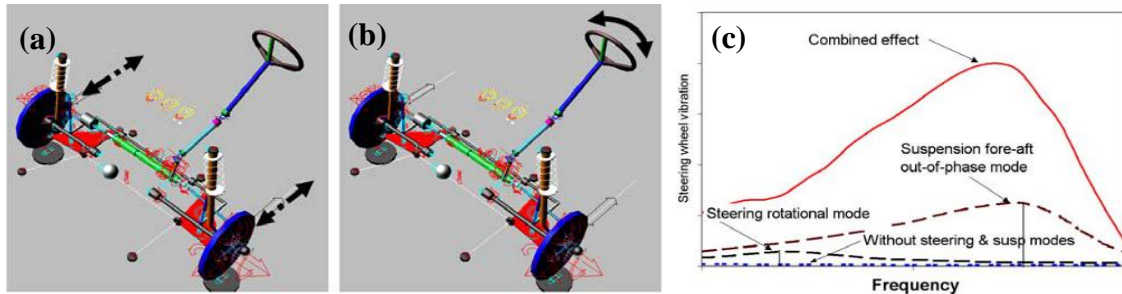


Figure 2-13: (a) The out-of-phase fore-aft mode of the suspension (b) the rotational mode of the steering wheel (c) the mode coupling effect<sup>108</sup>

In order to reduce the transmission, virtual DOE was conducted with two defined objectives: the maximum amplitude of the steering wheel vibration and the frequency for this maximum vibration. As results, the main influential factors were ranked and the relative importance of the factors was determined (Figure 2-14). The ranking of the factor were similar for both tire imbalance and brake judder because of the similarity of their transfer paths. The DOE results were validated by corresponding vehicle road tests followed. Due to confidentiality issue, the physical meanings of the factors were not disclosed.<sup>108</sup>

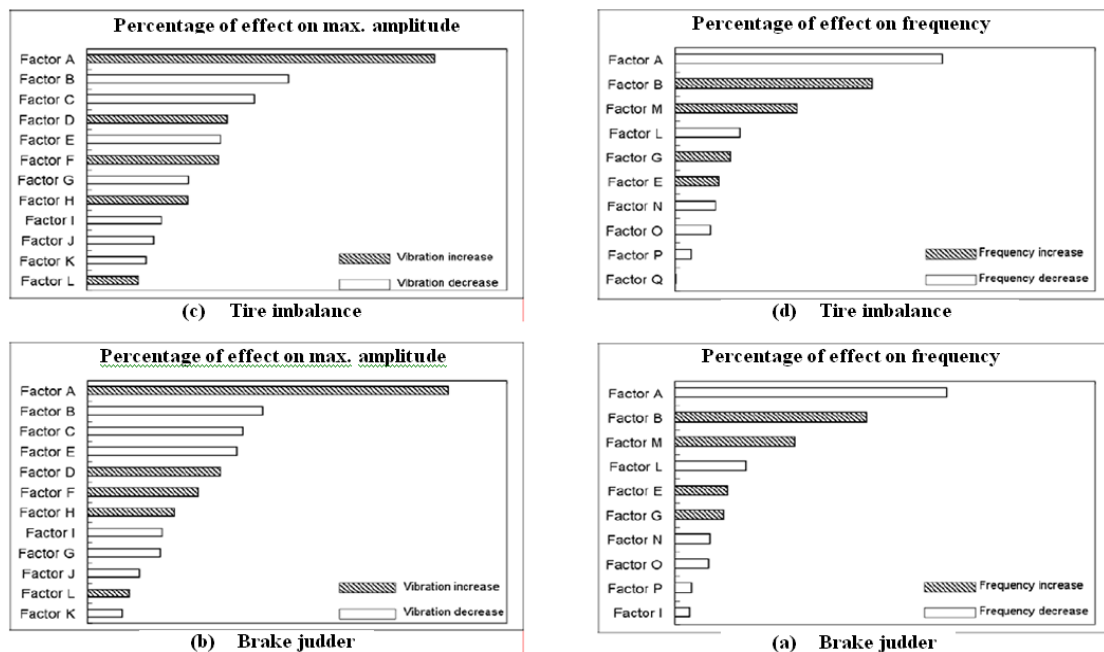


Figure 2-14: Ranking of the influential factors for reducing the transfer of tire imbalance and brake judder (factor specification changes from -10% to 10% around nominal setting)<sup>108</sup>

<sup>108</sup> Yu et al.: Chassis transmissibility: mechanism study and virtual DOE, 2007

### Meyer: mitigation of the specific mode shape

With the help of the vehicle test executed at chassis dynamometer and the simulation with a MBS model, Meyer testified that the transmission of brake judder could be strongly influenced by the motion shape of some special suspension components, which could be effectively eliminated by modifying one specific part. For example, the rotating vibration mode of the wishbone around the U1 bearing in a standard MacPherson front axle (Figure 2-15) greatly amplified the brake judder transfer, which was effectively depressed by replacing the normal rubber U3 bearing with a hydraulic bearing that has much higher damping property.<sup>109</sup>

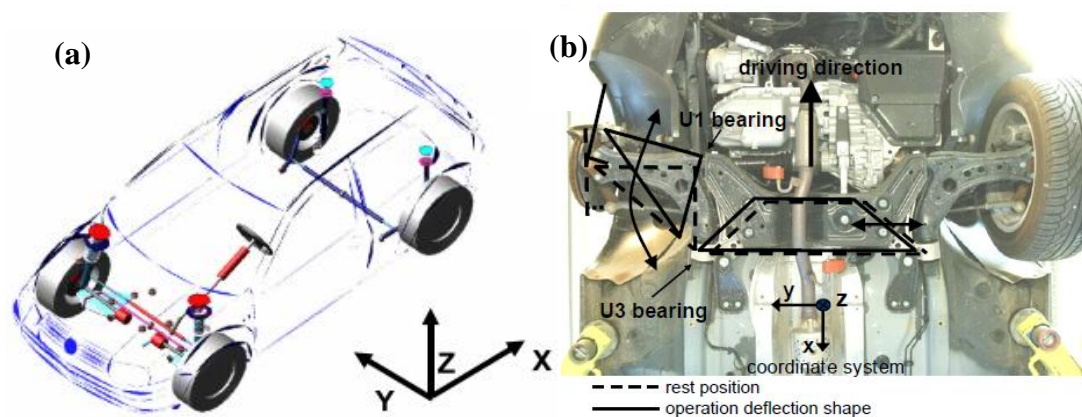


Figure 2-15: (a) The MBS model (b) The motion shape accounting for the resonance in the transfer path: the rotating vibration of the wishbone around the U1 bearing<sup>109</sup>

### 2.2.3 FE and analytical models

#### The FE model by Tan: resonance decoupling

According to the rotating vibration response of steering wheel in Figure 2-16 (a) during a vehicle road test and the modal analysis with a FE brake model (including the wheel brake system, the steering knuckle, and the connections with the suspension by ball joints) in Figure 2-16 (b), Tan suggested that the large response in the 16 to 19 Hz range was caused by the overlap of a resonance frequency in the steering system with another resonance frequency from the wheel brake system. Through sensitivity analysis with the FE model, the stiffness of the lower ball joint in *Y* and *Z* directions and the stiffness of the upper ball joint in *Y* direction were manifested to be the most influential factors of the resonance in the brake corner assembly. It was determined that this resonance frequency could be shifted to a higher value by increasing the stiffness of the ball joints, by which the high peak in 16 to 19 Hz was greatly mitigated.

<sup>109</sup> Meyer: Brake judder - excitation and transmission mechanism, 2005, p.1–9.



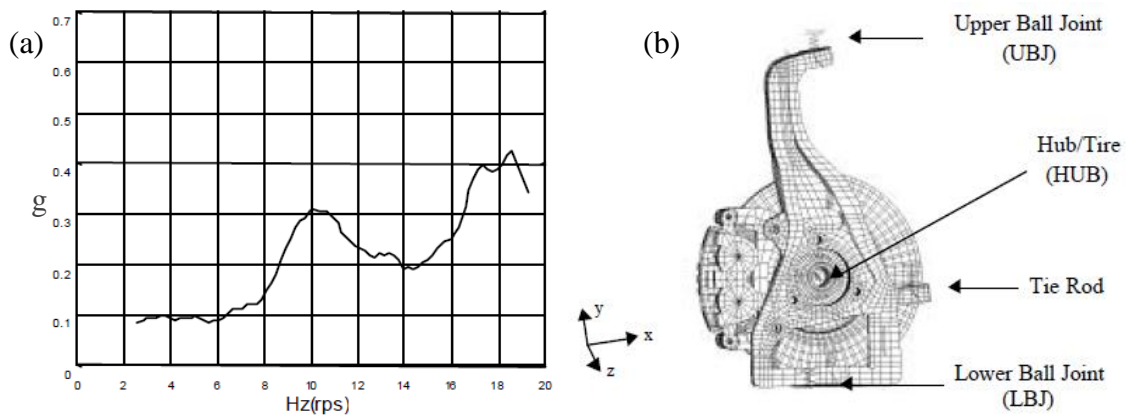


Figure 2-16: (a) The steering wheel rotating vibration and (b) the FEM model used by Tan<sup>110</sup>

### The simplified analytical model by Duan: diminishing the resonance effect

Duan<sup>111</sup> presented a simplified analytical source-path-receiver model, analyzing the brake judder transfer behaviors, as illustrated in Figure 2-17. The source regime contained a constant brake pressure  $P(t)$ , the brake pad and brake disc. The equivalent vehicle moment of inertia was added onto the disc. The input of the whole system was defined as the first order DTV with sine signal. The stiffness and damping in the wheel brake was represented by the linear spring  $K_p$  and the damping element  $C_p$ .

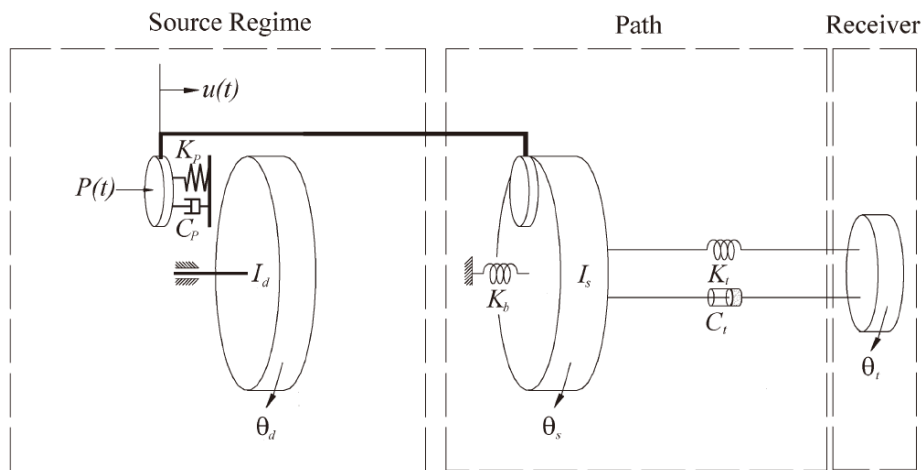


Figure 2-17: A simplified analytical source-path-receiver model of brake judder transfer<sup>111</sup>

The transfer path consisted of the moment of inertia  $I_s$  of the suspension system, the linear tensional stiffness  $K_t$  and damping  $C_t$  of the steering system, the nonlinear tensional stiffness  $C_t$  of the bushing that connects the suspension to the car body or the sub-frame. The steering wheel was the receiver with the moment of inertia  $I_r$ . Simulation

<sup>110</sup> Tan et al.: A parametric study of brake roughness, 2002, p.544.

<sup>111</sup> Duan and Singh: A simplified source-path-receiver model, 2011, p.142.

results showed that the transfer of brake judder was greatly amplified by a resonance frequency in the transfer path, while lower pad stiffness  $K_p$  and higher bushing stiffness  $C_t$  could effectively reduce the vibration levels. In particular, it was supposed that brake judder could be significantly reduced by active modulation of the brake pressure based on the information of the disc angular displacement and the specific DTV (perfect sine signal) used in the model.

## 2.2.4 Conclusion of the transfer behaviors

From the literature researches above, the main transfer behaviors of cold judder are summarized as follows:

- The steering wheel oscillation is the most significant effect of cold judder. Therefore, the transfer of the vibrations from the wheel brake to the steering wheel is the main focus of the most researches. All the components in the suspension system are involved in the transfer of cold judder from the wheel brake to the car body, but the transfer is dominant in the longitudinal direction (see Bittner). The transfer of drone noise has been completely neglected.
- The transfer of cold judder shares the similar mechanism of that of the tire imbalance force, and the transmissions of them are coupled sometimes. Therefore they are often investigated jointly (see Engel, Schlecht, and Yu).
- Some resonance frequencies and certain vibration modes are decisive for the transmission of cold judder. However, due to the diversity of the vehicle suspension systems and the steering systems, there is no unified subsystem or component that always accounts for the resonance frequency or the vibration mode. Regarding the sources of the resonance, each specific car should be treated as an individual case that ought to be specifically inspected and analyzed.

The mitigation strategies of cold judder transfer can be generally classified into three groups: modifying the characteristics of the chassis mounts, optimizing the axle kinematics, and the active control method. The methods employed by the authors above as well as their pros and cons are summarized in Table 2-2.

Besides, it was manifested by Lee that brake judder could be effectively reduced by active BTV compensation strategy for EMB (Electro-Mechanical Brake)<sup>112,113</sup> and EHB (Electro-Hydraulic Brake)<sup>114</sup>. In addition, it was supposed by Bittner that Brake-by-

---

<sup>112</sup> Lee: Brake force control and judder compensation, 2013

<sup>113</sup> Lee and Manzie: Adaptive BTV compensation for EMB, 2012

<sup>114</sup> Lee et al.: Active brake judder compensation using EHB system, 2015

Wire system and Steer-by-Wire system would completely isolate the transmission of brake judder to the brake pedal and the steering wheel respectively<sup>115</sup>.

Table 2-2: The reduction methods for brake judder transmission

Strategy	Method	Advantage	Disadvantage
<b>Modifying the characteristics of chassis mounts</b>	integrated optimization of all chassis mounts (see Bitter)	little changes of the mounts' properties is already effective	reliable MBS model is essential, validation is complicated
	identifying the influential factors by TPA and reducing the transmission by modifying the characteristics of chassis mounts (see Zhang)	result is relatively reliable	efficient combination of the test and simulation is required
	optimizing the transferability with defined objective functions through parameter sensitivity analysis that is conducted by means of virtual DOE (see Yu, Sim, and Duan)	fewer parameters are involved, thus faster	selection of the parameters is essential, and validation by vehicle tests is necessary
	avoiding the overlap of resonance frequencies (see Engel, Yu and Tan), and depressing the critical mode shapes (see Meyer)	efficient and effective	identification of the resonance frequencies or mode shapes is required.
<b>Optimizing the axle kinematics</b>	integrated optimization of the axle kinematics (see Schlecht)	effective	possible conflict with driving dynamics and driving comfort
	reducing or eliminating the lever arm of the disturbing force (see Engel)	simple and effective	potential influence on driving behaviors
<b>Active control</b>	active modulation of the brake pressure (see Duan)	effective for evident cold judder	costly and complicated

## 2.3 Human perception of vibration

### 2.3.1 Subjective rating of brake judder induced vibrations

Only by the measured vibration values it is impossible to judge the effects of brake judder on the human's subjective perception. Therefore the correlation between the subjective assessments and the objective measurements is required for evaluating the practical influences of brake judder on the drivers' subjective perception. The investiga-

<sup>115</sup> Bittner: Reduzierung des Bremsrubbels, 2006, p.29–32.

tion has already been done by many researchers regarding the vibrations caused by cold judder or by the imbalanced tire.

Engel investigated the correlation between the subjective rating and the measured valuation for the steering wheel oscillations<sup>116</sup>. As excitations two tire imbalance masses (40 g and 120 g) were separately applied at one front wheel of a sedan and vehicle road tests were carried out. The subjective evaluations were made by six persons for the tests with constant driving speeds from 60 to 180 km/h in a step of 10 km/h. A ten-level evaluation system was used for the subjective rating.

Neureder also studied the correlation for the steering wheel vibrations through vehicle road tests. Three C-segment passenger cars were tested with excitations of different tire balance masses at the front wheels as well. An eight-level evaluation system with ten subjective scores was adopted<sup>117</sup>.

Schlecht explored the correlations between the subjective ratings and the objective measurements of the steering wheel oscillation and the car body vibrations caused by cold judder through vehicle tests with a luxury car. Four DTV values (10, 20, 30, and 40  $\mu\text{m}$ ) and five decelerations were varied. The subjective ranking was made by six drivers according to a ten-level evaluation system.<sup>118</sup>

Besides, reference values about the correlation are also provided by two standards. VDI 2057<sup>119</sup> provides a reference according to the responses of seated persons on a seat with perpendicular sinusoidal movements. ISO 2631-1<sup>120</sup> supplies a reference based on the general human reactions to various magnitudes of overall vibrations in public transport.

However, the correlations identified in the investigations above showed great discrepancies, because effects of vibrations on human beings are dependent on many factors. Besides the individual's characteristics (physique, age, sex) and the physical parameters (amplitude, frequency and duration), they are also influenced by the direction of vibrations (with respect to the individual and the gravity), the part of the body where the vibrations enter, as well as the body posture (sitting, standing or recumbency)<sup>119</sup>. As further manifested by Bellmann that human response to both whole body vibrations and the steering wheel vibrations inside passenger cars are dependent on the types of cars (e.g. small, middle class, middle upper class; petrol or diesel), the frequency band (e.g. narrow bands or the whole range), the excitation characteristics (different motor orders),

---

<sup>116</sup> Engel: Systemansatz zur bremseregter Lenkunruhe, 1998, p.41–53.

<sup>117</sup> Neureder: Übertragung von Radkraftschwankungen auf die Lenkung, 2002, p.109–114.

<sup>118</sup> Schlecht: Minimierung der Schwingungsempfindlichkeit, 2012, p.47–54.

<sup>119</sup> VDI 2057 Part 1, 2002-09

<sup>120</sup> ISO 2631-1, 1997-05-01

the measuring positions (e.g. at seat track or on the seat surface for the whole body vibration), as well as the processing method of the objective accelerations (spectrally weighted acceleration or unweighted RMS acceleration)<sup>121</sup>. As a result, the correlation between the subjective perceptions and the objective measurements of the high-order judder induced vibrations needs to be individually identified.

### 2.3.2 Frequency weighting of vibration

In order to conduct the correlation analysis between the subjective ratings and the objective measurements of the vibrations, the objectively measured vibrations ought to be reasonably processed with respect to the basic features of the vibration signals, like the amplitude, the frequency, the duration as well as the position and the direction of the vibrations being perceived. For this sake, some standards are available, which provide uniform procedures and general instructions for the assessment of the vibrations. For example, VDI 2057 Part 1<sup>122</sup> and ISO 2631-1<sup>120</sup> are available for evaluating the human exposure to the whole-body vibration; VDI 2057 Part 2<sup>122</sup>, ISO 5349-1<sup>123</sup> and ISO 5349-2<sup>124</sup> can be used to assess the human exposure to the hand-arm vibration.

On the basis of the physical data of vibration measurements and taking the frequency-dependent effects and the exposure duration  $t_e$  into consideration, the root-mean-square (RMS) value  $a_{wt_e}$  of the frequency-weighted acceleration  $a_w(t)$  is formed as a variable characterizing the vibration exposure. Currently two methods are used for the formation of the RMS value of frequency-weighted accelerations, in time domain and frequency domain separately, as illustrated in Figure 2-18 and Figure 2-19.

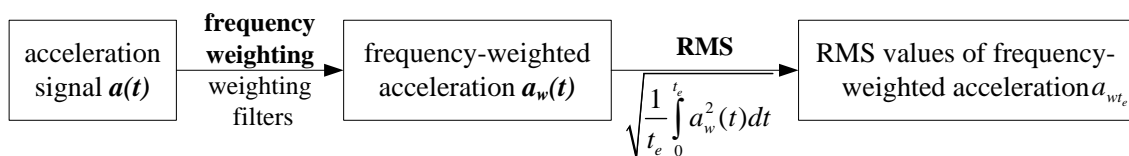


Figure 2-18: Calculating process of the RMS value of frequency-weighted accelerations in the time domain

In the time domain, the frequency-weighted acceleration  $a_w(t)$  is firstly calculated by frequency weighting of the acceleration signals with the weighting filters given by ISO-2631-1: 1997 and ISO 2631-2. The RMS  $a_{wt_e}$  is then the quadratic (energy-equivalent)

<sup>121</sup> Bellmann: Perception of whole body vibrations, 2002, p.103–133.

<sup>122</sup> VDI 2057 Part 2, 2014-05

<sup>123</sup> ISO 5349-1, 2001-05-01

<sup>124</sup> ISO 5349-2, 2001-08-01

mean value of the frequency-weighted acceleration  $a_w(t)$  defined as  $a_{wr_e} = \sqrt{\frac{1}{t_e} \int_0^{t_e} a_w^2(t) dt}$ .

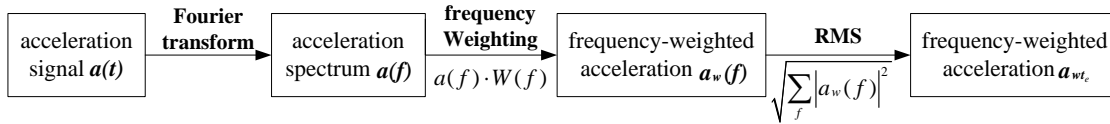


Figure 2-19: Calculating process of the RMS value of frequency-weighted accelerations in the frequency domain

In the frequency domain, the time signals of acceleration are firstly transformed by Fourier Transformation into either constant bandwidth or proportional bandwidth (e.g. as one-third octave band) spectra, the partial energy equivalent frequency-weighted acceleration  $\tilde{a}_w(f)$  is then calculated for each frequency component or for each frequency band by multiplying the RMS acceleration  $\tilde{a}(f)$  under each frequency component with the corresponding weighting factor  $W(f)$ . The RMS value  $\tilde{a}_{wr_e}$  of frequency-weighted accelerations is finally obtained by  $\tilde{a}_{wr_e} = \sqrt{\sum_f |\tilde{a}_w(f)|^2}$ . In general, only minor differences are to be expected between the results of the two methods<sup>119</sup>.

In the case of brake judder testing, the exposure duration  $t_e$  is the whole braking time. During the whole braking process, vibrations at the measured positions are varying under different velocities. One or more peaks could be obviously perceived, which are caused by the resonance frequencies in the transfer paths. In order to reveal this effect, the running RMS value of the frequency-weighted vibration acceleration  $a_w(t)$  can be calculated by using the following equation in the time domain:

$$a_w(to) = \sqrt{\frac{1}{\tau} \int_{to-\tau}^{to} [a_w(t)]^2 dt} \quad (2.4)$$

where  $\tau$  is the integration time constant for running averaging;  $t$  is the integration variable (time) and  $to$  is the time of observation (instantaneous time)<sup>120</sup>. Similarly, the running RMS of the frequency-weighted acceleration  $a_w(to)$  can be calculated by dividing the entire braking time  $t_e$  with a constant time window  $\tau$ . The running RMS method takes into account occasional shocks and transient vibrations by use of the short integration time constant (or constant time window)  $\tau$ . The vibration magnitude is defined as a maximum transient vibration value (MTVV), given as the highest magnitude of  $a_w(to)$  or  $a_w(t)$  during the measuring period, defined as:

$$MTVV = \max [a_w(to)] \text{ or } MTVV = \max [a_w(t)] \quad (2.5)$$

## 2.4 Human sensations of sound

### 2.4.1 Sound pressure and SPL

The sound caused by mechanical vibrations in the frequency band from approximately 16 to 16 kHz could be heard by human beings. Vibrations in air, liquids and solids are called airborne sound, liquid-borne sound and structure-borne sound respectively.<sup>125</sup>

A large amount of physical quantities (sound pressure, sound velocity, sound intensity, sound power, sound energy and etc.) can be used to describe the sound characteristics, among which sound pressure is mostly used in the measurement<sup>126</sup>. Sound pressure or acoustic pressure is the local pressure deviation from the ambient atmospheric pressure, caused by a sound wave. Sound pressure in air can be measured by using a microphone, which transforms the sound pressure to electrical signals. Condenser microphones are the most popularly used microphones in the sound pressure measurement. A condenser microphone is a passive electrostatic transducer, consisting of a mobile diaphragm and a rigid backplate. The working principle and the equivalent circuit of condenser microphones are shown in Figure 2-20.

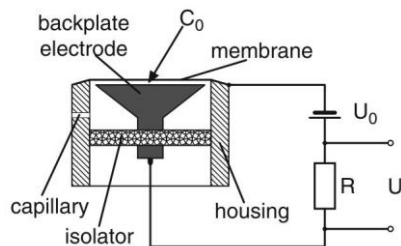


Figure 2-20: The working principle and the equivalent circuit of condenser microphones<sup>127</sup>

A constant polarisation voltage  $U_0$  (typically 200 V) over a very large resistance  $R$  ( $> 10 \text{ G}\Omega$ ) is applied in the circuit. This voltage creates a constant charge on the condenser. A sound-induced modulation of the distance between the diaphragm and the backplate results in a change in capacity with constant charge, and thus in a sound-induced AC voltage signal  $U$  added to the constant polarisation voltage. For amplitudes that are not too high, the relation between sound pressure and voltage is linear to an excellent approximation. With the measurement microphones used today, this approximation is valid for very high sound pressure levels of up to 140 dB. The dimensions of standard measurement microphone are with a diameter of 1/2-inch (12.7 mm) and a distance between the diaphragm and the backplate of about 20  $\mu\text{m}$ . The capacity of this

<sup>125</sup> Müller: Handbook of engineering acoustics, 2013, p.8.

<sup>126</sup> Möser: Messtechnik der Akustik, 2010, p.26.

construction is about 20-30 pF. But other diameters of 1-, 1/4-, or 1/8-inch are also in use.<sup>127</sup>

In view of Weber's and Fechner's law, stating that the human perception is proportional to the logarithm of the stimulus, the physical quantities are usually expressed in terms of their levels. This law applies for the acoustical perception. The sound pressure level  $L_p$  is defined to be<sup>125</sup>

$$L_p = 20 \lg \frac{p_{rms}}{p_0} \quad (2.6)$$

where  $p_{rms}$  denotes to the RMS value of the signal with

$$p_{rms}^2 = \frac{1}{\tau} \int_0^{\tau} p^2(t) dt \quad (2.7)$$

The standardized reference is  $p_0 = 2 \times 10^{-5} \text{ N/m}^2$ , which is also the threshold audibility of human beings. The averaging time of  $\tau = 250 \text{ ms}$  and  $\tau = 1 \text{ s}$  are normally adopted as "fast" and "slow" separately.<sup>128</sup> "Slow" has the property that the SPL is relatively constant, but the peaks of the measuring signals could be strongly smoothed.

### 2.4.2 Psychoacoustics

Interfering noises are sounds with a negative sound quality, which is perceived as unpleasant, disturbing and interfering. Vehicle noise can be characterized as interfering, if it fills at least one of the following conditions:<sup>129</sup>

- A sound is unpleasant or interfering even if the passengers expect this sound to happen due to their actions.
- The sound quality is worse than expected.
- The extent to which the person feels disturbed (too weak or too strong) is not relevant.
- A sound occurs without the user expecting the sound event (e.g. rattling of parts of the interior trims).
- The noise does not occur due to any event related to the usage of the automobile (e.g. warning noises due to the lack of engine lubrication).

Influences of noises on human sensation are currently described by some psychoacoustic parameters. The most often used ones as well as their main influential factors are

---

<sup>127</sup> Müller: Handbook of engineering acoustics, 2013, p.31.

<sup>128</sup> Genuit: Sound-Engineering im Automobilbereich, 2010, p.6.

<sup>129</sup> Genuit: Sound-Engineering im Automobilbereich, 2010, p.185.



listed in Table 2-3. Psychoacoustics is the science about the relationship between the physical quantities of sound and the subjective hearing impressions. The hearing-related quantities, also referred to as psychoacoustic parameters, provide a linear representation of human hearing perception. This means that a doubling of a psychoacoustic quantity corresponds to a doubling of the corresponding subjective perception level<sup>130</sup>.

Table 2-3: Psychoacoustic parameters<sup>131</sup>

Parameter	Unit	Description	Influential factors
<b>Loudness</b>	sones	consideration of the frequency distribution and the masking characteristics	SPL, frequency, duration, masking, spectral bandwidth
<b>Sharpness</b>	acum	ratio of the high-frequency loudness to the whole loudness.	frequency composition
<b>Roughness</b>	asper	consideration of the temporal structure of signals, modulation depth and level difference	carrier frequency, modulation frequency, modulation depth, SPL <sup>130</sup>
<b>Fluctuation Strength</b>	vacil	periodic variation of signals with modulation frequency smaller than 20 Hz	modulation frequency, SPL
<b>Tonality</b>	tu	proportion of tonal, narrowband components	tonal, narrowband components

## Loudness

Loudness is the sensation value of the human perception of sound volume<sup>132</sup>. The formal definition of loudness is that: “intensive attribute of auditory sensation in terms of which sounds can be ordered on a scale extending from soft to loud”<sup>133</sup>. The perception of loudness mainly depends on the sound level, the frequency and the bandwidth of the sound event, as well as the masking effects<sup>134</sup>. Loudness increases with rising duration of stimulus and it keeps constant only when the duration is longer than 200 ms<sup>131</sup>.

## Sharpness

The sharpness of a sound event depends on its frequency composition. Fundamentally, the sharpness of a signal is the higher the more high frequencies it contains. The factor that most affects sound sharpness is the distribution of its spectral envelope<sup>134</sup>. Sharp-

<sup>130</sup> Head acoustics: Psychoacoustic Analyses II, p.1.

<sup>131</sup> cf. Genuit: Sound-Engineering im Automobilbereich, 2010, p.54–73.

<sup>132</sup> Head acoustics: Psychoacoustic Analyses I, p.1.

<sup>133</sup> Rossing: Handbook of acoustics, 2014, p.484.

<sup>134</sup> Müller: Handbook of engineering acoustics, 2013, p.78–80.

ness is not suitable for describing the low frequency phenomenon e.g. booming (narrowband 20 to 180 Hz noise), because the parameter sharpness is aimed for the perception of high-frequency noises.<sup>131</sup>

### **Roughness**

Roughness is a perception dimension that occurs most often with frequency-modulated and amplitude modulated sounds. The impression of roughness occurs whenever a time-variant envelope exists within a critical band, for example, when tones exhibit a temporal structure due to a variation of their amplitude or frequency. Frequency modulation leads to higher perceived roughness than amplitude modulation. It is less dependent on the sound pressure level. The sound pressure level has to be increased by circa 40 dB in order to double the roughness.<sup>130</sup>

### **Fluctuation strength**

Fluctuation strength describes the perception of "slow" modulations. The noises that are with 20 Hz or lower modulations are perceived as fluctuated<sup>131</sup>. Perception of fluctuation strength is especially important in terms of the unpleasantness of sounds.

### **2.4.3 Equal loudness contours and frequency weighting filters**

Considering the characteristics of the drone noise caused by the high-order judder (which can be roughly considered as frequency-sweep signals, especially in the case of modified discs with artificial DTV, see Section 7.1.1) as well as the definitions and application scenarios of the psychoacoustic parameters discussed in 2.4.2, loudness is the most suitable parameter to describe drone noise. By which the most important features of drone noise, its amplitude (SPL) and frequency, are emphasized. The dependency of loudness on SPL and frequency is illustrated by DIN ISO 226 with the equal loudness contours, as shown in Figure 2-21.

The curves of different loudness levels were obtained by testing. It is complicated to directly use the equal loudness contours to correlate the sound measurements with the human sensation of loudness. In practice therefore, some filters, such as *A*-weighting, *C*-weighting, *Z*-weighting and et al. are applied to account for the relative loudness perceived by the human ear<sup>135</sup>. Because human beings are most sensitive to the sound around 1000 to 4000 Hz, and since the *A*-weighting curve has the characteristic of emphasizing this frequency range, it is readily adopted as the standard for measuring

---

<sup>135</sup> DIN EN 61672-1, 2014-07, p.20–49.

workplace noise<sup>136</sup>. According to Zeller, A-Weighting is also the most commonly used filter for vehicle acoustics, because all the weighting filters are only very rough approximations of the human subjective sensitivities in the circumstances of complex noises<sup>137</sup>. A weighted loudness is normally indicated with the unit dB(A) and the weighting function in amplitude spectrum is expressed by<sup>135</sup>:

$$A(f') = 10 \lg \left[ \frac{12194^4 f'^4}{(f'^2 + 20.06^2) \sqrt{(f'^2 + 107.7^2)(f'^2 + 737.9^2)(f'^2 + 12194^2)}} \right]^2 + 2 \quad (2.8)$$

where  $f'$  is the normalized frequency value, with  $f' = f/\text{Hz}$ .

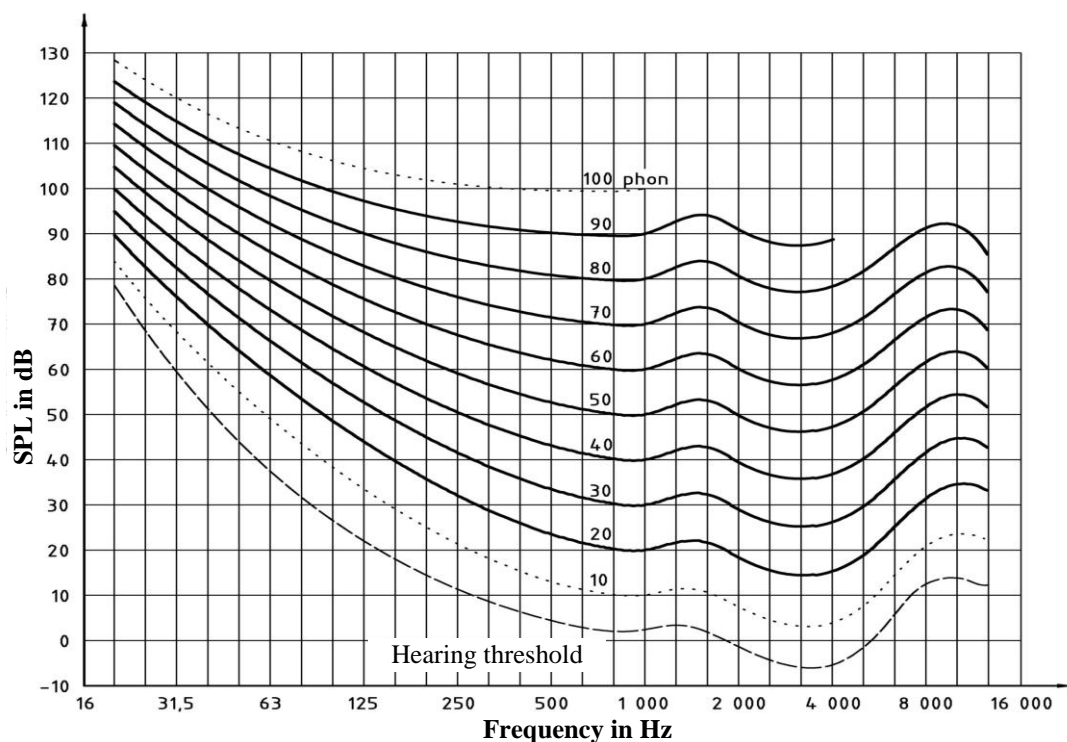


Figure 2-21: Threshold of hearing and equal loudness contour<sup>138</sup>

The frequency weighted loudness level is called the loudness level  $L_N$  and is measured in the unit called phon. The loudness level is a numerical value that is identical to the sound pressure level of an equally loud 1000 Hz tone. Above 40 phon, a 10-phon increase in the loudness level is roughly equivalent to a doubling of the perceived loudness<sup>139</sup>. In order to display the practical effects of different loudness levels on human

<sup>136</sup> Richard L. St. Pierre Jr. and Maguire: The impact of A-weighting SPL measurements, 2004

<sup>137</sup> Zeller et al.: Handbuch Fahrzeugakustik, 2012, p.192.

<sup>138</sup> DIN ISO 226, 2006-04, p.9.

<sup>139</sup> Müller: Handbook of engineering acoustics, 2013, p.72.

sensation, the typical subjective evaluations and the typical scenarios of the loudness level ( $L_N$ ), as well as the corresponding parameters of loudness ( $S_N$ ), sound pressure level ( $L_p$ ), sound pressure ( $p$ ) and sound intensity ( $I$ ) for 1000 Hz pure tone sounds are shown in Table 2-4. It is classified into seven groups from 0 to 140 phon.

Table 2-4: Classification of human sensation to loudness after Melz<sup>140</sup>

Group	$L_N$ (phon)	$S_N$ (sone)	$L_p$ (dB)	$p$ (pa)	$I$ (W/m <sup>2</sup> )	Evaluation	Scenario
1	140	1024	140	$2 \times 10^2$	$10^2$	very loud to unbearable loud	commercial vehicles in 5 m, aircraft noise, passing train noises at platform
	134	threshold of pain					
	130	512	130				
	120	256	120	$2 \times 10^1$	1		
	110	128	110				
	100	64	100	2	$10^{-2}$		
2	90	32	90			loud	passenger cars in 5 m, very loud talking
	80	16	80	$2 \times 10^{-1}$	$10^{-4}$		
3	70	8	70			fairly loud	office background noises
	60	4	60	$2 \times 10^{-2}$	$10^{-6}$		
4	50	2	50			fairly quiet	soft speech
5	40	1	40	$2 \times 10^{-3}$	$10^{-8}$	quiet	whisper
6	30		30			very quiet	very soft speech
7	20		20	$2 \times 10^{-4}$	$10^{-10}$	not or barely perceptible	in the quietest surroundings
	10		10				
	3.8	threshold of hearing					
	0		0	$2 \times 10^{-5}$	$10^{-12}$		

<sup>140</sup> Melz: Maschinenakustik- Kapitel2, Teil 3, 2013, p.87–89.

---

## 3 Goals and overall methodology

### 3.1 Scientific goals

On the one hand, as clarified in section 1.4 and 2.1.1 that high numbers of hot spots were found in many hot judder tests but the occurring mechanism of hot spots has been still not completely well-known, thus the trigger and development mechanisms of hot spots have been almost the exclusive focuses of the current hot judder investigations. On the other hand, the transfer behaviors of cold judder and the final effects of the vibrations caused by cold judder on the driver have been already intensively investigated by means of vehicle test and simulation (section 2.2 and 2.3). In consideration of the different frequency ranges of high-order hot judder and cold judder, the ultimate goal of this work is therefore established to explore the question:

- Whether the high-order hot judder can be perceived by the driver in passenger cars, and thus leads to customer complaints?

In order to answer this question, two aspects need to be considered and some further specific questions are raised:

- 1) **Incidence of high-order hot judder in the real vehicles.** Since the current hot judder tests have been mostly carried out with the brake dynamometers (section 1.4), considering the different constraints (e.g. the overall support stiffness, the cooling rate of the brake disc, and possibly the retroaction of some vehicle resonance frequencies) of the wheel brakes and the modifications of the hydraulic layouts of the braking system at the dynamometers, as well as the different control methods of the test conditions:
  - Whether high-order hot judder can be excited in the vehicle test? Or are the high orders found in the dynamometer tests reproducible in the vehicle tests?
  - Whether the dynamometer test results are transferable to the vehicle test? Or in other words, are the behaviors of hot judder (e.g. the intensity and the dominant order) in the dynamometer tests representative for those under real vehicle driving conditions?
- 2) **Perception thresholds of high-order hot judder.** Even if there was high-order hot judder occurring in the vehicle:
  - Under which conditions (e.g. the frequency range and the thresholds of BTV/BPV) could the high-order hot judder be perceived by the driver?
  - In which form (as vibration, noise, or both) could the high-order hot judder be perceived by the driver?

## 3.2 Overall methodology

Based on the goals raised above, a top-down approach is established to investigate the questions, as presented in Figure 3-1.

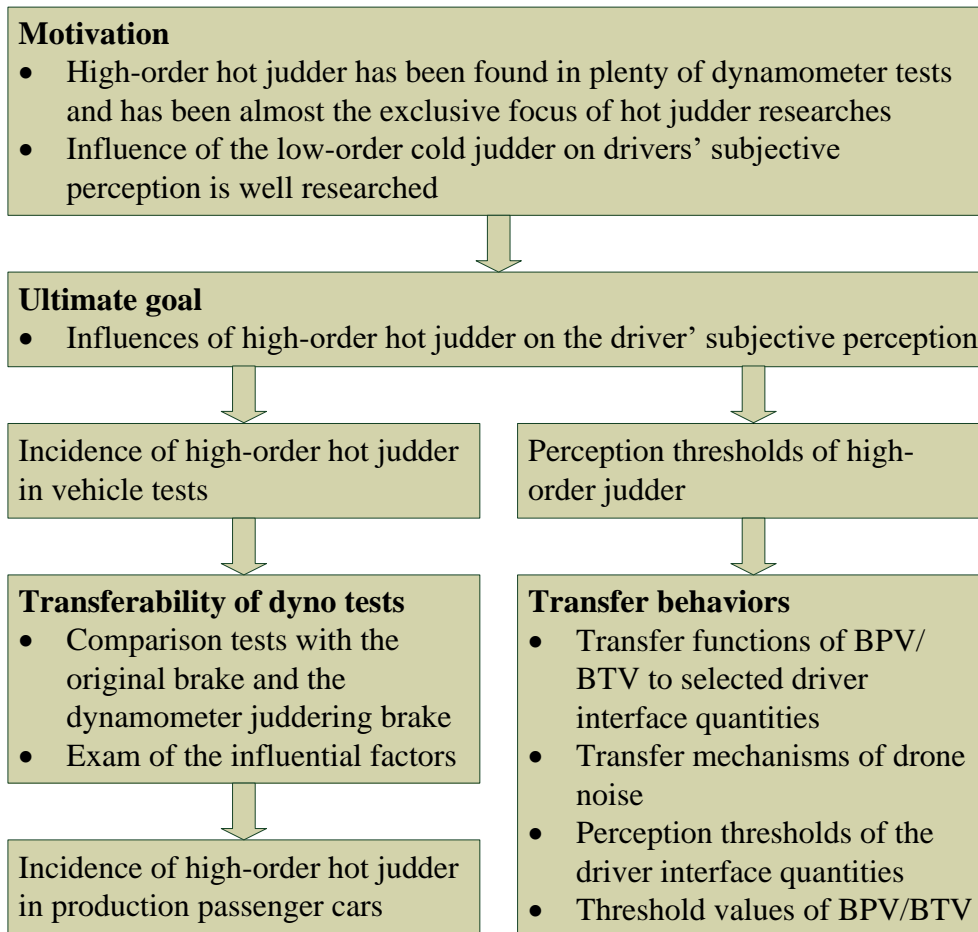


Figure 3-1: The overall top-down methodology

In order to detect the incidence of high-order hot judder in passenger cars, the transferability from dynamometer test to the vehicle test is firstly investigated. One front brake and one rear brake from two similar mid-size upper class cars are separately tested through dynamometer test and vehicle test. Regarding the vehicle test, both driving tests on the test tracks and vehicle tests at chassis dynamometer have been carried out. Only the original brake components are adopted in the tests of the front brake, while two sets of intentionally produced brake pads that have the same structure but different materials (the NAO pads and the ECE low-metallic pads) compared with the original pads are employed in the tests of the rear brake. The identical brake components are used in all the corresponding comparison tests. The hot judder behaviors between dynamometer tests and vehicle tests are compared with respect to the dominant order and the amplitude of the dominant order. In addition, the support stiffness of the wheel brake in the

dynamometer tests has been modified, so as to examine the influential factors of the hot judder behaviors. Moreover, further vehicle road tests with the other four production cars have been conducted, in order to identify the incidence of high-order judder in the production brakes.

The perception thresholds of high-order hot judder are indicated by the threshold values of BPV/BTV, the threshold values of the selected vibrations at the driver interface (the brake pedal pulsation, the steering wheel oscillation, and the whole car body vibrations in three directions) and the critical noise levels of the vehicle interior drone noise. The links between the BPV/BTV and the driver interface quantities are defined as global transfer functions, by which the transfer behaviors of the high-order judder are presented. In order to investigate the transfer behaviors with a higher signal-to-noise ratio and guaranteed judder occurrence, a novel test method is employed. That is, vehicle tests with brake discs that are artificially modified with desired surface shapes simulating the high-order DTV/LRO. Altogether three passenger cars with seven brake discs possessing various DTV or LRO are tested, and the transfer functions of BPV/BTV to the vibrations and drone noise at the driver interface are identified for the three vehicles. In addition, based on the assumed transfer paths the transfer mechanisms of drone noise from BTV at the wheel brake to the vehicle interior are clarified, by using the results of the vehicle tests.

The threshold values for perceiving the vibrations are obtained by regression analysis between their subjective ratings and objective measurements, and the critical values for drone noise perception are selected through literature research on the vehicle interior noise level and the masking effect of sound. Based on the threshold values of the driver interface vibrations and drone noise as well as the identified transfer functions, the threshold values of BPV/BTV are determined in the frequency domain.

Test methodologies regarding the transferability investigation, the vehicle tests for researching the transfer behaviors, and the threshold values of the vibrations caused by the high-order judder are demonstrated in Chapter 4, and the results of these investigations are presented in Chapter 5, 6, and 7.

---

## 4 Test methodology

### 4.1 Basics and definitions

#### 4.1.1 Fist caliper brake

Because all the brakes involved in this work are one-piston fist caliper brakes, the basic structure and working principle as well as the nomenclatures (see Figure 4-1) need to be clarified, in order to guarantee a better understanding of the following investigations and results. This type of caliper looks like the human fist, so it is normally called the fist caliper. The side of disc that possesses the brake piston is called the “piston side” and the other side that looks like the human fingers is called the “finger side” in this work.

The fist caliper brake consists of the main components of the brake disc, the brake pads, the caliper, and the caliper bracket. The brake disc is fixed with the wheel hub that is supported by the wheel bearings, thus it rotates simultaneously with the wheel. The caliper bracket is screwed together with the wheel knuckle, which is connected with the car body or the sub-frame via the suspension components. The caliper is connected with the caliper bracket through the bushings and guide pins, and the connection allows the caliper moving “freely” along the guide pins. Besides, there is a vent valve at the caliper, enabling the venting of gases from the brake fluid. In the following vehicle tests, this vent valve is removed and a pressure sensor is directly mounted into the vent hole.

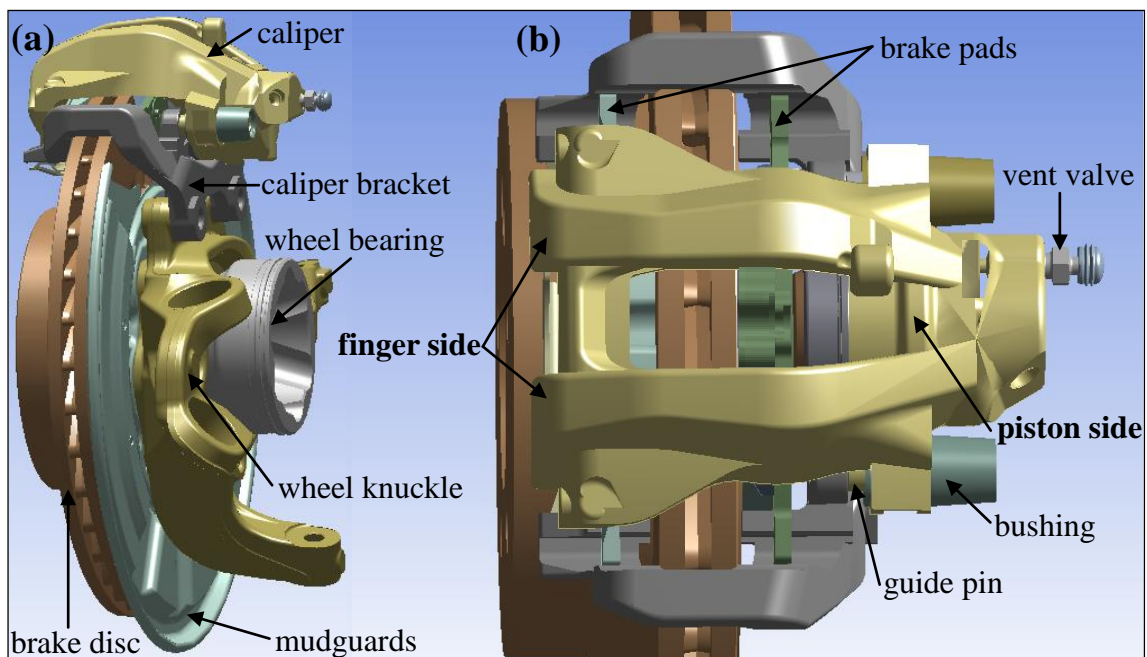


Figure 4-1: (a) The brake corner assembly and (b) the wheel brake system of a fist caliper brake



### 4.1.2 Definition of the characteristic parameters

DTV, LRO, BPV, BTV, temperature variation on the disc surfaces (hot spots), the vibrations at the wheel brake and the driver interface, as well as the drone noises near the wheel brake and inside the vehicle are the characteristic parameters used for testing and evaluating hot judder in this work. Regarding the notations, the values of DTV, LRO, BPV, BTV and temperature variation are separately denoted as  $\Delta d_D$ ,  $\Delta z_D$  (referring to the cylindrical coordinate system of the brake disc  $(r, \varphi, z)$ , the coordinate  $z$  corresponds to the axial direction of the brake disc),  $\Delta p_B$ ,  $\Delta M_B$ , and  $\Delta T_D$  in the following.

According to the definition by Engel with the illustration in Figure 4-2 that DTV is the difference between the maximum Disc Thickness (the initial disc thickness, DT2) and minimum Disc Thickness (DT1), and LRO is the “peak-to-peak” amplitude of the disc waviness. The disc surface geometry at a disc radius is measured by two displacement sensors placed at the opposite positions of the two disc sides. Given the distance signals  $d1(r, \varphi)$  and  $d2(r, \varphi)$ , DTV and LRO are separately calculated by:

$$\Delta d_D(r) = \max_{0 \leq \varphi < 2\pi} (d1(r, \varphi) + d2(r, \varphi)) - \min_{0 \leq \varphi < 2\pi} (d1(r, \varphi) + d2(r, \varphi)) \quad (2.9)$$

$$\Delta z_D(r) = \max_{0 \leq \varphi < 2\pi} (d1(r, \varphi) - d2(r, \varphi)) - \min_{0 \leq \varphi < 2\pi} (d1(r, \varphi) - d2(r, \varphi)) \quad (2.10)$$

Since the disc surface geometries at more than one radius are measured during the brake dynamometer tests and the road tests of vehicle C, the DTV and LRO values used in the analyses are the average of those at all the radii, denoted as  $\overline{\Delta d_D}$  and  $\overline{\Delta z_D}$  respectively.

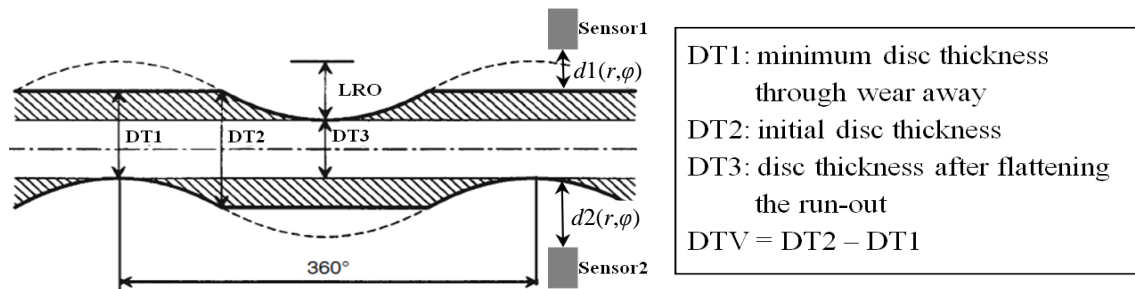


Figure 4-2: The definitions and measuring method of DTV and SRO<sup>141</sup>

Following the definitions of DTV and LRO, which are actually both peak-to-peak values (maximum values - minimum values for a sine signal), the values of BPV, BTV, and disc surface temperature variation are also defined as the peak-to-peak values in this work. Nevertheless, the amplitudes of vibrations and noises are the conventional amplitudes in the following order analyses and spectral analyses.

<sup>141</sup> cf. Engel: Systemansatz zur bremsenregter Lenkunruhe, 1998, p.80.

## 4.2 Methodology for transferability investigation

In order to investigate the transferability of hot judder test from the brake dynamometer to real vehicles, the hot judder behaviors of two brakes in the brake dynamometer tests and in the vehicle tests are compared (this part is called the “comparison test” in the following). Since great discrepancies have been found in the results of these two types of testing, further tests with modified stiffness of the wheel brake support at the brake dynamometer are carried out, so as to detect the influential factors for the discrepancies (this part is called the “modification test” in the following). Furthermore, because no evident high-order hot judder has been found in the vehicle tests with the two brakes in the comparison test, further vehicle tests with four passenger cars are carried out in order to identify the incidence of the high-order hot judder in the production brakes (this part is called the “identification test” in the following). The main methodology and results of the comparison test and the identification test have been published in the publications of the author<sup>142,143</sup>, which are not further cited in detail in the following.

### 4.2.1 Test strategy of the comparison test

As mentioned in the overall methodology, one front brake with the original brake pads and one rear brake with specifically produced pads are tested in the comparison test. The main specifications of the two brakes are listed in Table 4-1.

Table 4-1: Main specifications of the brakes used for the comparison test

Characteristics	Front brake	Rear brake
Caliper type	fist caliper	fist caliper
Disc type	ventilated	ventilated
Disc diameter	320 mm	320 mm
Disc thickness	32 mm	24 mm
Pad arc length	48°	42°
Number of piston	1	1
Piston diameter	46 mm	42 mm
Effective (geometric) friction radius	133.5 mm	141.5 mm

---

<sup>142</sup> Xu and Winner: Hot judder characteristics in passenger car, 2015

<sup>143</sup> Xu and Winner: An experimental comparison of hot judder behaviours, 2016

In the first place, drag braking applications and stop braking applications are carried out for the both brakes with the brake dynamometer. In the second place, the identical brake pads, calipers, caliper brackets, and knuckles used in the dynamometer tests are mounted into the vehicles and tested through vehicle tests. In order to avoid the influence of the disc wear-out states after the brake dynamometer tests, new discs are used in the two types of tests.

Since the front brake is dominant with 1<sup>st</sup> to 4<sup>th</sup> lower orders in all the tests, whereas the rear brakes with both kinds of brake pads show 9<sup>th</sup> to 15<sup>th</sup> higher dominant orders in the drag braking applications carried out at brake dynamometer, and because the focus of this work is on the high-order hot judder, in the third place, further vehicle tests with the help of the chassis dynamometer are only conducted for the rear brakes, where tests of both stop braking and drag braking applications are possible.

Therefore, for the front brake, hot judder behaviors in the road tests will be compared with those in the stop braking applications executed at the brake dynamometer; for the rear brake, hot judder behaviors in the three types of stop braking applications as well as in the two types of drag braking applications will be compared respectively. The overall test and comparison strategy is illustrated in Figure 4-3.

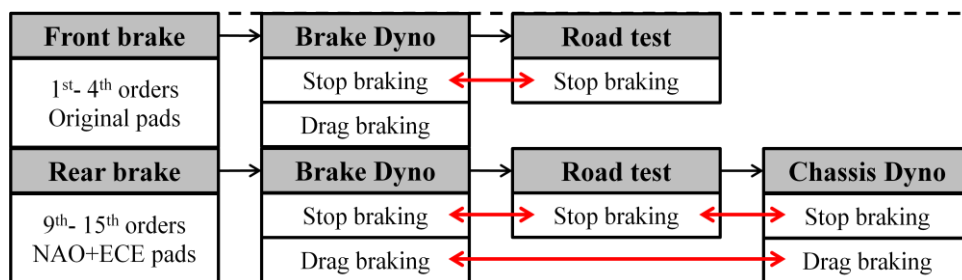


Figure 4-3: The overall test and comparison strategy of the hot judder comparison test

The corresponding test design for each test is displayed in Table 4-2. With respect to all stop braking applications, the initial disc surface temperature is always kept at 200 °C; four deceleration variations of 0.2, 0.3, 0.4, and 0.5 g are employed; three initial braking velocities of 175, 200, and 225 km/h are varied, except for the road test (from 175 and 225 km/h) and the brake dynamometer test of the rear brake (only from 225 km/h).

Regarding the drag braking applications, generally three velocity variations and four variations of braking pressure are applied, and the testing duration is determined by the disc surface temperature ranging from 100 to 500 °C. For the brake dynamometer tests of the rear brake, in addition to the braking applications with constant pressures, one test program with constant brake torques of 100, 150, 200, and 300 Nm is also conducted, with their corresponding average braking pressures roughly equivalent to the four varied pressures. For the chassis dynamometer test of the front brake, although only brake pressure is taken as control quantity, two different test programs are run: one program from the lowest velocity and braking pressure (175 km/h, 10 bar) to the highest

ones (225 km/h, 30 bar), and the other in the opposite direction. Besides, in order to detect the hot judder behaviors at lower velocities, 125 km/h has been run in the testing of the front brake. Restricted by the drag braking performance of the brake dynamometer, the maximum braking pressure is limited to 25 bar for the front brake and 30 bar for the rear brake.

Table 4-2: Test design of hot judder comparison tests

Front brake	Brake dynamometer test				Road test	
	Stop braking		Drag braking		Stop braking	
	$v_0$ (km/h)	175, 200, 225	$v$ (km/h)	125, 175, 225	$v_0$ (km/h)	175, 225
$a_0$ (g)	0.2, 0.3, 0.4, 0.5	$T$ (°C)	100 to 500	$a_0$ (g)	0.2, 0.3, 0.4, 0.5	
$T_0$ (°C)	from 200	$p$ (bar)	10, 15, 20, 25	$T_0$ (°C)	from 200	

Rear brake	Brake dynamometer and chassis dynamometer test				Road test	
	Stop braking		Drag braking		Stop braking	
	$v_0$ (km/h)	225	$v$ (km/h)	175, 200, 225	$v_0$ (km/h)	175, 225
$a_0$ (g)	0.2, 0.3, 0.4, 0.5	$T$ (°C)	100 to 500	$a_0$ (g)	0.2, 0.3, 0.4, 0.5	
$T_0$ (°C)	from 200	$p$ (bar)	10, 15, 20, 30	$T_0$ (°C)	from 200	

Moreover, because new brake discs are used for each of the tests, before all the tests a run-in program composed of 60 stop braking applications from 80 to 30 km/h with a constant braking pressure of 30 bar and an initial disc surface temperature of 100 °C has been executed for the dynamometer tests. Accordingly, a similar run-in program consisting of 30 stop braking applications from 80 km/h to standstill with a deceleration of about 0.4 g and the same initial disc surface temperature of 100 °C has also been carried out for the road tests.

## 4.2.2 Test setups of the comparison test

### Brake dynamometer test

The brake dynamometer used in this investigation is the FZD dynamometer, its general working and data acquisition principles for hot judder testing can refer to the introduction by Sardá<sup>144</sup>. The hydraulic control system and the test setup for the front brake testing at the brake dynamometer are shown in Figure 4-4. This dynamometer can be conducted by the brake torque, the brake pressure, or the brake deceleration. The control

<sup>144</sup> Sardá: Wirkungskette von Hotspots und Heißrubbeln, 2009, p.38–53.

of these parameters is realized through the control valve labeled with number 10 in Figure 4-4. Between the control valve and the caliper a throttle valve (in the grey box labeled with number 11) is mounted in the brake line, in order to attenuate the transmission of the pressure variation from the caliper into the control valve. Otherwise, the dynamometer control system would be always trying to compensate the BTV or BPV, depending on the currently controlled parameter.

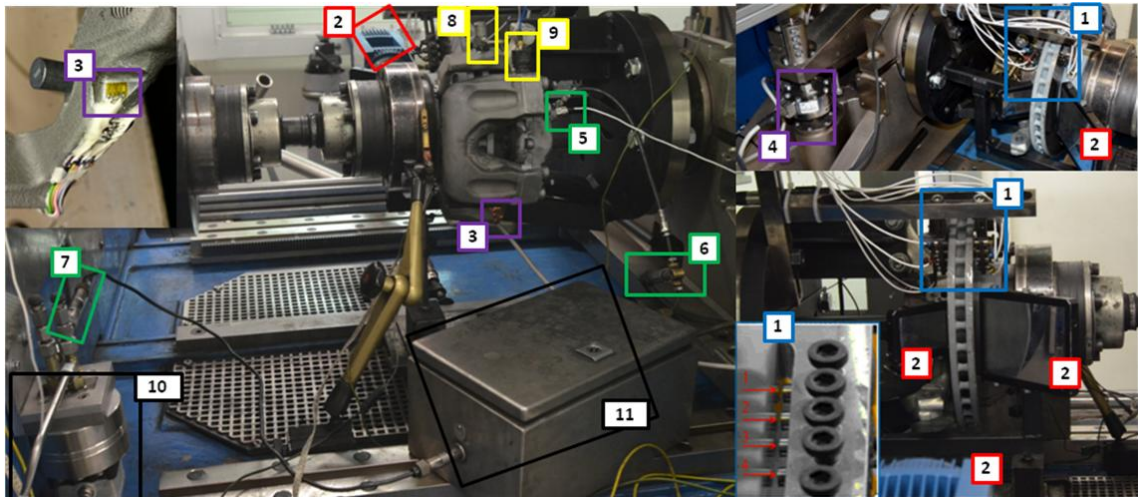


Figure 4-4: Test setup and control system of the brake dynamometer

Table 4-3: Measured quantities and specifications of the sensors applied to brake dynamometer

Nr.	Measured quantity	Sensor (producer, type)	Effective range
1	disc surface geometry (DTV and LRO)	capacitive displacement sensors, Capacitec, HPC-150-H	0-250 $\mu\text{m}$ , max. 400 $^{\circ}\text{C}$
2	Hot spots	infrared camera with mirror system, CEDIP Jade III MWIR	-40 - 900 $^{\circ}\text{C}$
3	BTV	strain gauges, HBM, 1-XY31-1.5/120.	-
4	BTV	force transducer	-
5	BPV at caliper vent hole	pressure transducer, Kulite, HKM-375(M)	0-70 bar
6	BPV near caliper	pressure transducer	-
7	BPV after throttle	pressure transducer	-
8	caliper bracket vibration	1-axis accelerometer, Kistler, 8610B100	$\pm 100\text{ g}$
9	caliper vibration	3-axis accelerometer, Kistler, 8766A50	$\pm 50\text{ g}$

Quantities relevant to hot judder and their measuring sensors are listed in Table 4-3. Main working principles for measuring these quantities are as follows:

- **DTV/LRO:** Because the positions of hot spots in the radial direction of brake disc are constant neither in various brakes nor in subsequent braking applica-

tions with the same brake<sup>145</sup>, eight capacitive displacement sensors are applied, measuring the disc surface geometry at four different radii of the friction rings.

- **Hot spots:** an infrared camera with a mirror system design enabling the measurement of temperature distributions at both disc surfaces with only one camera. The temperature measurement is synchronized with the rotating speed of the dynamometer drive engine, measuring 125 positions per disc rotation and 250 pixels simultaneously in the disc radial direction.
- **BTV:** the brake torque is normally acquired by the force transducer in the torque measuring shaft assembly of the brake dynamometer. However, there is a resonance frequency at about 188 Hz in this measuring shaft assembly<sup>146</sup>, by which the BTV measurement around this frequency is strongly amplified. In order to avoid this effect and to have the identical BTV measuring equipment both at the brake dynamometer and in the vehicle, another measuring method named “strain gauge caliper bracket” has been developed<sup>147,148</sup>. Strain gauges are arranged at the most sensitive positions of the caliper bracket according to the full Wheatstone bridge configuration and are calibrated with the torque measuring shaft assembly of the brake dynamometer under static conditions.
- **BPV:** three pressure transducers are installed in order to measure the brake pressure: the first one directly at the vent hole of the brake caliper, the second one in the brake line near the caliper and the last one near the control valve. By comparing the pressure variations before and after the throttle, the attenuation effect of the throttle can be revealed.
- **Caliper and caliper bracket vibrations:** one 3-axis accelerometer is adopted measuring the caliper vibrations in three directions and a single 1-axis accelerometer is mounted at the caliper bracket gauging its circumferential vibration.

Besides these quantities, the disc surface temperature is monitored by a sliding contact thermocouple (type K) and it is employed as the trigger signal (start and finish trigger signal in the drag braking applications as well as start trigger signal in the stop braking applications). The rotational speed that is essential for the order analysis is determined by a Hall sensor which gives one impulse per disc rotation. Except for the measurement of hot spots, the sampling rate of all the other signals is set to 10 kHz. The dynamometer test setup for testing the rear brake is similar with that for the front brake testing, which is attached in Figure B-1.

---

<sup>145</sup> Sardá: Wirkungskette von Hotspots und Heißrubbeln, 2009, p.54–70.

<sup>146</sup> Fischer et al.: Effects of different friction materials on hot judder, 2013, p.5–6.

<sup>147</sup> cf. Bauer: Einflusses einer Messvorrichtung auf Bremsmomentschwankungen, 2012

<sup>148</sup> cf. Kämmer: Prüfmethodik zur Bestimmung von Bremsmomentschwankungen, 2013

## Vehicle tests

In the vehicle tests, the identical strain gauge caliper brackets, the pressure transducer at the caliper vent hole, and the two accelerometers at the caliper and the caliper bracket are separately mounted into the front left brake and the rear left brake of the test vehicles. The disc's surface temperature and rotational speed are also acquired following the same principles as those in the brake dynamometer tests. For the vehicle test at the chassis dynamometer, in addition to these sensors, a pyrometer is installed measuring the temperature variations on one radius of the disc friction ring (see Figure 4-5), because the pyrometer responds faster to the temperature changes than the thermocouple.

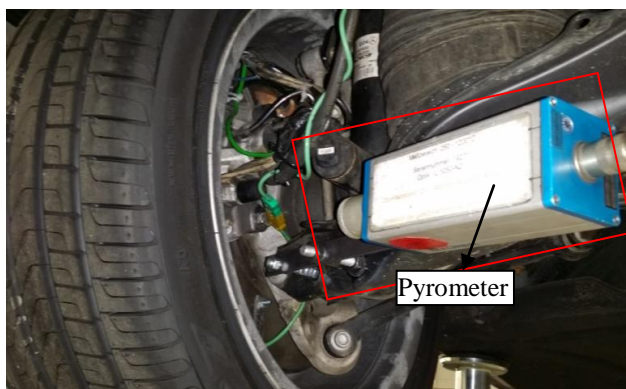


Figure 4-5: Installation position of the pyrometer

Both the hydraulic layout and the control method in the chassis dynamometer vehicle tests (see Figure 4-6) are similar to those in the brake dynamometer tests. But they are different with those in the vehicle road tests. During each road vehicle test the driver is trying to keep the brake pedal at a constant position and the brake pressure is generated through the normal vehicle braking system (the brake booster and the master cylinder instead of the control valve and the throttle of the brake dynamometer).

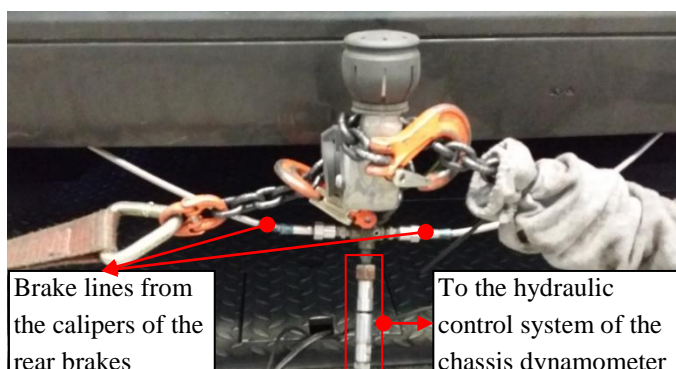


Figure 4-6: The brake lines from the rear brakes are directly connected to the hydraulic control system of the chassis dynamometer

The differences of the hydraulic layout and the control method are supposed to be the main reason that could lead to various hot judder behaviors between the two types of

dynamometer tests and the road tests. Another deviation of the vehicle chassis dynamometer test from the vehicle road test is that the rear axle is disconnected to the powertrain during the chassis dynamometer test, because the test vehicles have All Wheel Drives (AWD).

The vehicle road tests with the initial braking speed of 175 km/h are performed on the runway of the test track in August-Euler-Airfield<sup>149</sup> (as illustrated in Figure 4-7), on which a maximum initial braking velocity of 180 km/h is possible for the test cars. The tests with the initial braking speed of 225 km/h are carried out on the runway of the Opel Test Center Pferdsfeld<sup>150</sup>, which is about 3000 m long and allows a maximum initial braking speed of approximately 230 km/h for the test vehicles.

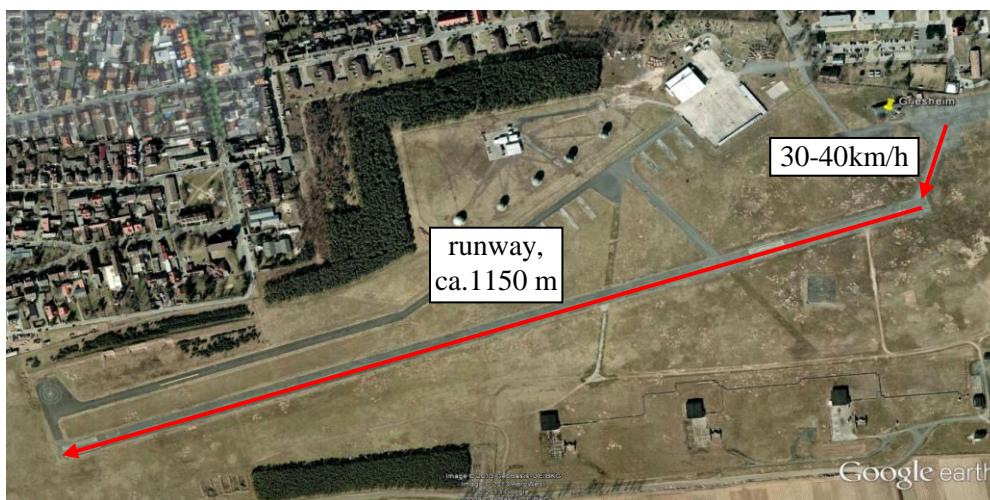


Figure 4-7: The test track in August-Euler-Airfield (Picture source: Google earth)

### 4.2.3 Methodology of the modification test

In the brake dynamometer test the caliper bracket is connected with the wheel knuckle that is fixed with the dynamometer through an adapter, whereas the knuckle is attached to the car body or the sub-frame through the suspension components in a vehicle. Therefore, the support stiffness of the wheel brake is different in these two test types.

In the comparison test of the rear brake, the adapter displayed in Figure 4-8 (a) is used. The three cuboid pillars (with which the knuckle is directly fixed) in the axial direction are reinforced by several ribs, by which the torsional stiffness of the adapter is greatly enhanced. In order to examine the influence of the wheel brake support stiffness on the hot judder behaviors, brake dynamometer tests with another adapter without any ribs (shown in Figure 4-8 (b)) are carried out. The torsional stiffness of this adapter is much

---

<sup>149</sup> <https://de.wikipedia.org/wiki/August-Euler-Flugplatz> , accessed at 16.09.2016

<sup>150</sup> [https://de.wikipedia.org/wiki/Fliegerhorst\\_Pferdsfeld](https://de.wikipedia.org/wiki/Fliegerhorst_Pferdsfeld), accessed at 16.09.2016



smaller. The test matrix of the brake dynamometer test for the rear brake (see Table 4-2) is repeated for this setup and a pair of Cu-free pads from Fischer's DOE is adopted.

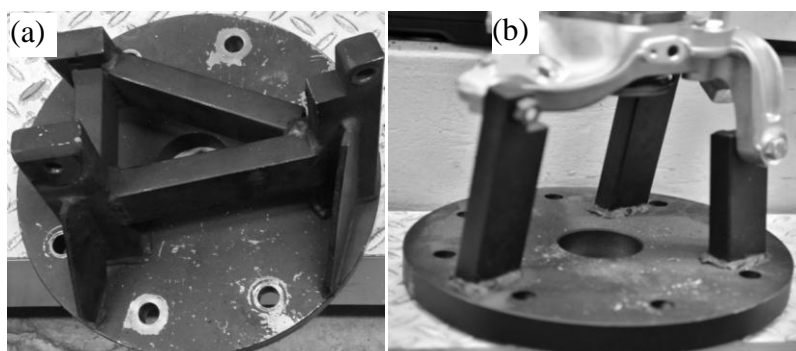


Figure 4-8: (a) The stiffer adapter and (b) the flexible adapter for the wheel brake

#### 4.2.4 Methodology of the identification test

Based on the good correlations between the vibrations of the caliper and the caliper bracket and the other hot judder characteristic parameters (DTV, LRO, BPV, and BTV)<sup>151</sup>, the hot judder situations in all the wheel brake of four passenger cars are identified by sticking accelerometers on the caliper and the caliper bracket. This method is much more efficient than by measuring other quantities of hot judder (e.g. hot spots, disc surface geometries, BTV or BPV) in the vehicle tests. Two 1-axis accelerometers (Kistler, 8610B50) are used and the circumferential vibrations of the caliper and caliper bracket are measured during the tests.

In addition, the disc surface temperature and the wheel rotational speed are also gauged. The tests are also performed on the runway of the test track in August-Euler-Airfield. The initial braking speeds are in the range between 160 and 180 km/h. For the testing of each wheel brake, three variations of braking deceleration (ca. 0.2, 0.3, and 0.4 g) and two variations of initial disc temperature (ca. 100 and 200 °C) are applied.

### 4.3 Methodology for the transfer behaviors

#### 4.3.1 The fundamental investigation strategy

The vibrations and drone noise caused by hot judder are transmitted by various transfer paths that often show complicated frequency dependence and non-linear properties. Instead of the concrete transfer paths, the global transmissions from the wheel brake to the driver interface disturbances are determined as the expression of the transfer behav-

<sup>151</sup> Xu and Winner: Hot judder characteristics in passenger car, 2015, p.6.

iors of high-order judder in this work. Six quantities of brake pedal pulsation in the actuation direction, the circumferential steering wheel oscillation, the drone noise inside the vehicle, and the car body vibrations in  $X$ ,  $Y$ , and  $Z$  directions (longitudinal, lateral and vertical directions with respect to the vehicle's coordinate system) are selected as critical driver interface disturbances of hot judder.

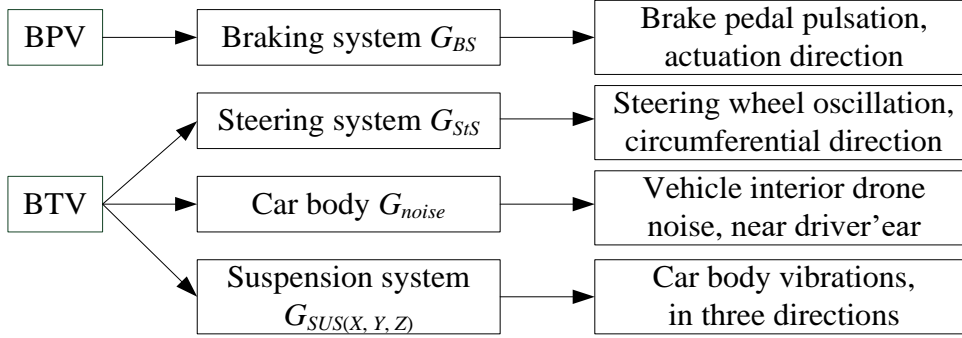


Figure 4-9: The six global transfer functions defined for the transfer behavior investigation

Consequently, assuming that under the hot judder occurring condition of light deceleration the transfer paths can be seen as Linear Time-Invariant (LTI) systems, six transfer functions of BPV/BTV from one wheel brake to the hot judder interface quantities (see Figure 4-9) are defined:

- In the braking system, BPV causing brake pedal pulsation in the actuation direction:

$$G_{BS}(f) = \left| \frac{a_{pedal,atu}(f)}{\Delta p_B(f)} \right|; \quad [G_{BS}(f)] = \frac{\text{m/s}^2}{\text{bar}} \quad (4.1)$$

- In the steering system, BTV causing circumferential steering wheel oscillation:

$$G_{StS}(f) = \left| \frac{a_{SW,circ}(f)}{\Delta M_B(f)} \right|; \quad [G_{StS}(f)] = \frac{\text{m/s}^2}{\text{Nm}} \quad (4.2)$$

- Drone noise transmission, BTV causing drone noise with a sound pressure  $p$  inside a vehicle:

$$G_{noise}(f) = \left| \frac{p_{interior}(f)}{\Delta M_B(f)} \right|; \quad [G_{noise}(f)] = \frac{\text{Pa}}{\text{Nm}} \quad (4.3)$$

- In the suspension system, BTV causing seat track vibrations (measurement of the car body vibrations) in the  $X$ ,  $Y$ , and  $Z$  directions:

$$G_{SUS(X,Y,Z)}(f) = \left| \frac{a_{ST(X,Y,Z)}(f)}{\Delta M_B(f)} \right|; \quad [G_{SUS(X,Y,Z)}(f)] = \frac{\text{m/s}^2}{\text{Nm}} \quad (4.4)$$

### 4.3.2 The novel test method: artificially modified discs

Because DTV/LRO of hot judder are temporary and dynamic, they will disappear when brake disc cools down and the positions of hot spots in both circumferential and radial directions of the disc surfaces alternate in the subsequent braking applications<sup>152</sup>. Besides, it is difficult to calculate the transfer functions with two or even four inputs of hot judder excitations from the two or four wheel brakes of a vehicle. Moreover, as inspected by the identification test with production passenger cars that it is difficult to find the hot judder with one single dominant high order in the production brakes (see the investigation in 4.2.4), or even in the brakes with specifically produced brake pads that show evident high-order hot judder in the brake dynamometer tests (see the comparison test in 4.2). Therefore, in order to identify the transfer functions of high-order hot judder with a higher signal-to-noise ratio and higher quality, brake discs that are artificially modified by using the numerical control machine into desired surface shapes simulating the high-order DTV/LRO are taken as the solution. As high-order hot judder around 10<sup>th</sup> order is the research objective established in this work, the 10<sup>th</sup> DTV or LRO have mainly been imitated. For example, Figure 4-10 shows two discs with 60  $\mu\text{m}$  “10<sup>th</sup> order” DTV (grooves at corresponding positions on both sides of the disc) and 100  $\mu\text{m}$  “10<sup>th</sup> order” LRO (grooves at alternating positions on both sides of the disc), respectively.

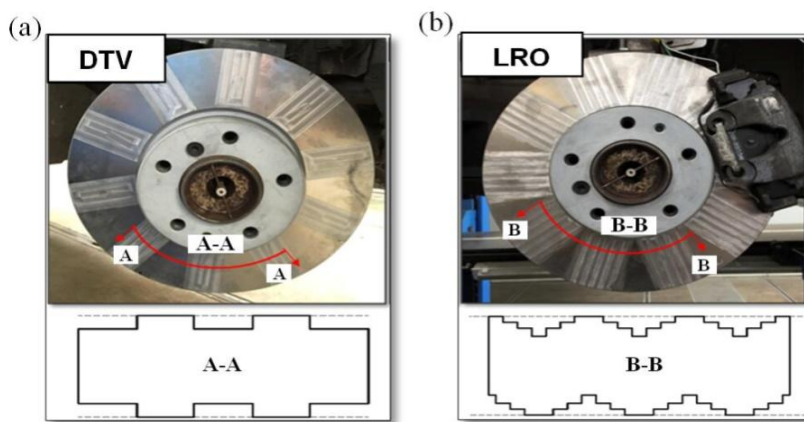


Figure 4-10: Discs with 10<sup>th</sup> order artificial DTV or LRO: (a)  $\Delta d_D \approx 60 \mu\text{m}$ ; (b)  $\Delta z_D \approx 100 \mu\text{m}$

### 4.3.3 Test vehicles and modified discs

In order to compare the transfer behaviors of high-order hot judder in different passenger cars, one compact car (vehicle A) and two mid-size luxury cars (vehicle B and C) that are all equipped with fist caliper disc brakes are tested. Main technical data of the three vehicles are listed in Table 4-4.

<sup>152</sup> Sardá: Wirkungskette von Hotspots und Heißrubbeln, 2009, p.54–70.

Table 4-4: Technical data of the three vehicles under test

Component/Feature	Vehicle A	Vehicle B	Vehicle C
class	compact	mid-size luxury car	mid-size luxury car
production year	2004	2002	2011
<b>Car body</b>			
construction	5-door sedan	5-door sedan	5-door sedan
permitted weight	1960 kg	2150 kg	2370 kg
<b>Engine</b>			
type	L4-cylinder petrol; front, transversely	V8-petrol; front, lengthwise	V6-petrol engine; front, lengthwise
engine displacement	1984 cm <sup>3</sup>	3498 cm <sup>3</sup>	3498 cm <sup>3</sup>
nominal power	110 kW at 6000 rpm	180 kW at 5800 rpm	225 kW at 6500 rpm
nominal torque	200 Nm at 3500 rpm	345 Nm at 3800 rpm	370 Nm at 2400-5000 rpm
<b>Drive train</b>			
type	AWD, permanent	standard drive	AWD, permanent
gearbox	6 speed manual	5 speed manual	5 speed Manumatic
<b>Tire</b>			
size	205/55 R16	235/45 R17	245/45 R17 95W
rim size	6.5Jx16 ET50	8.0Jx17 ET25	8.0J x 17 ET48
<b>Front axle</b>			
type	MacPherson strut	double wishbone, coil spring -strut	double wishbone, air spring
total toe	- 0°10' ± 0°10'	+ 0°14' ± 0°10'	+ 0°17' ± 0°17'
camber	- 0°30' ± 0°30'	- 0°13' ± 0°30'	- 0°55' ± 0°36'
caster	+ 7°34' ± 0°30'	+ 6°36' ± 0°30'	+ 7°01' ± 0°50'
kingpin inclination	+14°40'	+ 13°0'	-
kingpin offset	-	positive	-
<b>Rear axle</b>			
type	twist beam axle	multi-link independent, coil spring -strut	multi-link independent, air spring
total toe	- 0°10' ± 0°13'	-	- 0°10' ± 0°13'
camber	- 1°20' ± 0°30'	-	- 1°5' ± 0°50'
<b>Steering</b>			
type	rack-and-pinion steer- ing	recirculating ball steer- ing	rack-and-pinion steer- ing
mounting location	front axle, sub-frame	front axle, sub-frame	front axle, sub-frame
power steering	EPS	EPS	EPS
overall transmission	-	17.9	variable
<b>Brake</b>			
front brake	one-piston fist caliper, ventilated discs	one-piston fist caliper, ventilated discs	one-piston fist caliper, ventilated discs
rear brake	one-piston fist caliper, solid discs	one-piston fist caliper, ventilated discs	one-piston fist caliper, ventilated discs

All brakes of the three vehicles were tested by accelerometers mounted on the brake calipers, but none of them were detected with evident high-order hot judder. Since hot judder of the front brakes is more significant to the steering wheel oscillation than that of the rear brakes, the transfer behaviors of high-order judder from the front brakes are set to be the main focus in this investigation. Therefore, the front left brakes of the three vehicles are replaced by the modified discs with artificial DTV/LRO. However, vehicle tests with modified discs in the rear left brake of vehicle *C* are also conducted, in order to inspect the transfer behaviors from the rear brakes.

Besides, various brake discs are applied in the testing of the same vehicle, so as to investigate the influences of different disc surface geometries on the test results. Altogether seven modified discs are tested by using these three vehicles: one for the front left brake of vehicle *A*, two for the front left brake of vehicle *B*, one for the front left brake of vehicle *C*, and three for the rear left brake of vehicle *C*. The discs tested by vehicle *B* are displayed in Figure 4-10 and the ones used in the tests of vehicle *A* and *C* are shown in Figure 4-11. Particularly, one disc with “20<sup>th</sup>” order is tested by the rear brake of vehicle *C*, whereas all the other discs are with “10<sup>th</sup>” order.

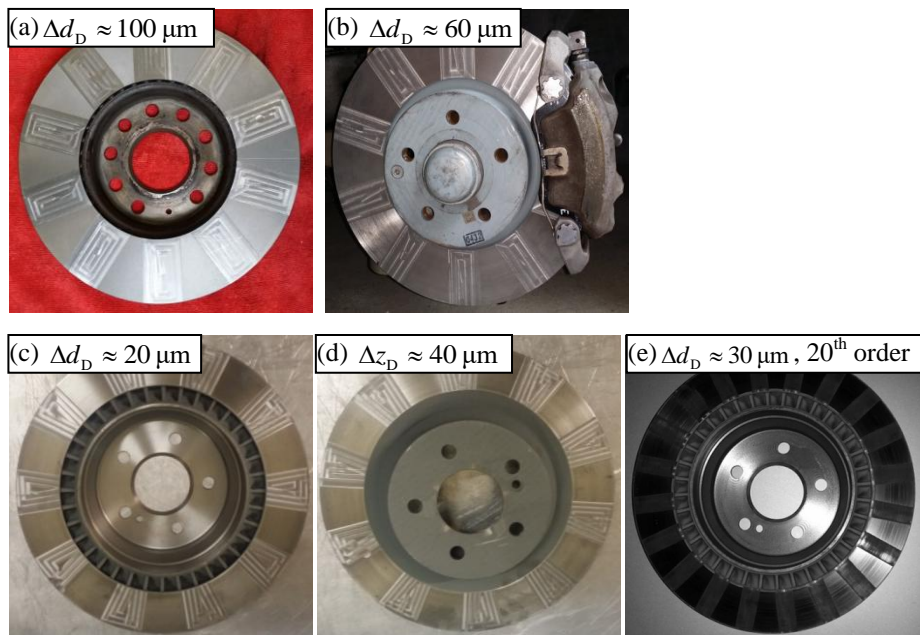


Figure 4-11: (a) The disc in the front left brake of vehicle *A*, (b) the disc in the front left brake of vehicle *C*, (c) (d) and (e) the three discs in the rear left brake of vehicle *C*

#### 4.3.4 Test setup

According to the defined global transfer functions, the sensors are distributed at corresponding positions on the wheel brake and the driver interface, as shown in Figure 4-12. For the measurement of BTV, strain gauges caliper brackets are applied in the front and rear brakes of vehicle *C*, whereas a Wheel Force Sensor (WFS, also called Measuring

Rim) from A&D company<sup>153</sup> is used vehicle *A* and *B*. The WFS measures the three forces ( $F_x$ ,  $F_y$ , and  $F_z$ ) and the three moments ( $M_x$ ,  $M_y$ , and  $M_z$ ) at the wheel with reference to the wheel coordinate system. It provides the wheel rotational speed and rotational angle information as well. BPV is acquired by a pressure transducer, mounted at the vent hole of the brake caliper. Vibrations of the brake pedal, the seat track, and the steering wheel are gauged with accelerometers. Drone noises near the juddering wheel brake and near the driver's ear inside the vehicle are measured by condenser microphones. The microphones have been calibrated with a sound calibrator (Reten Electronics Schallpegelkalibrator RQ 159) before usage. The calibrator generates a reference SPL of 110 dB with a reference frequency of 1 kHz.

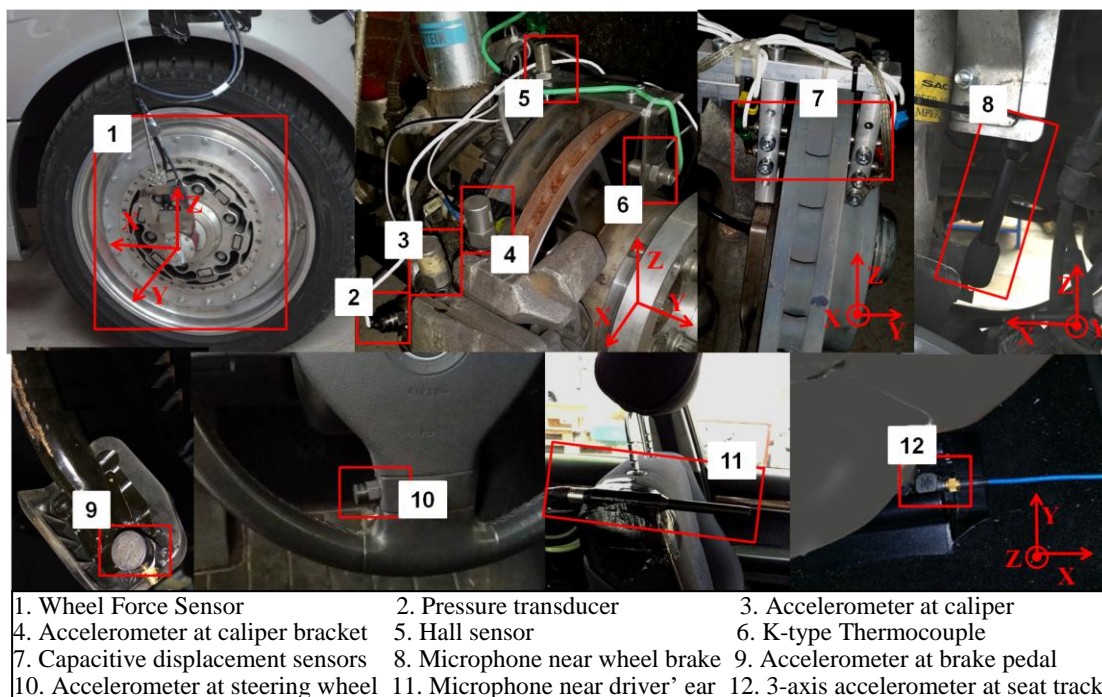


Figure 4-12: Sensor distribution of the vehicle tests

Besides the quantities that are relevant for the investigation of the high-order judder transfer behaviors, the surface geometries at two friction rings of the front left disc in vehicle *C* are measured by four capacitive displacement sensors. The surface temperature of the modified discs is also detected by a sliding thermocouple. The wheel rotational speed is supplied by the WFS in vehicle *A* and *B*, but it is acquired with a Hall sensor in vehicle *C*. In addition, the vibrations of the brake caliper and the caliper bracket in the disc's circumferential direction are measured with accelerometers. Main specifications of the applied sensors are listed in Table 4-5.

<sup>153</sup> A&D Company: <http://www.aandd.jp/products/dsp/wfs.html>, accessed at 29.05.2016.

Table 4-5: Specification of the sensors used in the vehicle tests

Measured quantity	Sensor (producer, type)	Effective range
BTV	Wheel Force Sensor, A&D	$\pm 4.5$ kNm ( $M_Y$ )
BPV	pressure transducer, Kulite, HKM-375(M)	0-70 bar
sound pressure near wheel brake and near driver's ear	microphones, Superlux, ECM999	20-20 kHz, 0-128 dB
brake pedal pulsation and steering wheel oscillation	1-axis accelerometer, Kistler, 8612B5	$\pm 5$ g
seat track vibrations	3-axis accelerometer, Kistler, 8766A5	$\pm 5$ g
caliper and caliper bracket vibrations	1-axis accelerometer, Kistler, 8610B100	$\pm 100$ g
disc surface geometry	capacitive displacement sensor, Capacitec, HPC-150-H	0-250 $\mu$ m, max. 400 °C
disc surface temperature	thermocouple, type K	0 to +900 °C
wheel rotational speed	Hall sensor, Hamlin 55075	1 impulse per revolution

### 4.3.5 Data acquisition system

Two compact QuantumX (see Figure 4-13) from Hottinger Baldwin Messtechnik GmbH (HBM)<sup>154</sup> are employed as the data acquisition system in the vehicle tests. QuantumX MX840A and QuantumX MX1601B are universal amplifiers, providing separately 8 and 16 individually configurable channels. Every channel supports over 15 different transducer technologies and the QuantumX has the unique capability to acquire signals from any analog sensor.

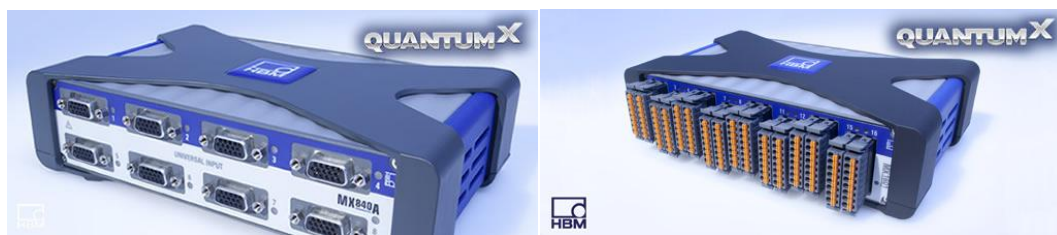


Figure 4-13: (a) QuantumX MX840A (b) QuantumX MX1601B (Picture sources: HBM)

The two modules can be connected together by Firewire and synchronized through NTP (Network Time Protocol), as illustrated in Figure 4-14. The output signals from the two QuantumX are transferred to a laptop via Ethernet and the data acquisition software used in the tests is Catman Easy, also from HBM.

<sup>154</sup> HBM: <http://www.hbm.com/en/>

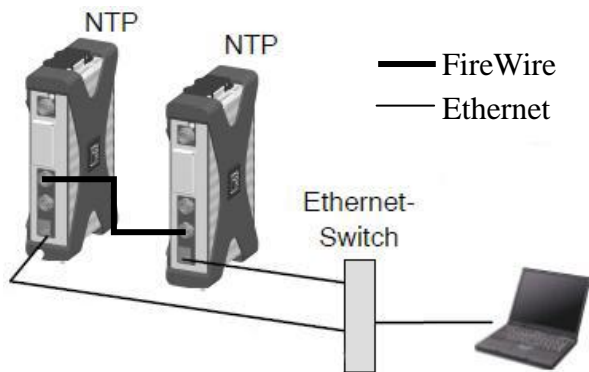


Figure 4-14: Synchronization of the QuantumX (Picture sources: HBM)

One essential advantage of the QuantumX MX840A is that its first connector is compatible with CAN bus, which allows an easy synchronization of the WFS signals (CAN bus signals) with the signals from other sensors (analog signals). The sampling rate is set to 4800 Hz for all the sensors during the tests. Because the maximum sampling rate of the WFS is limited to 1000 Hz, the output signals of it (e.g. the BTV signal) are resampled by the nearest-neighbor interpolation algorithm.

This data acquisition system is also used in all the other vehicle tests involved in this work, for example, the comparison test and the identification test in 4.2.2.

### 4.3.6 Test maneuver

The vehicle tests are carried out on the runway of the test track in August-Euler-Airfield as well. Regarding the driving maneuver, the test cars were always speeded up with the maximum accelerations to a highest speed that is permitted by the length of the runway and then were immediately changed to the neutral gear, afterwards they were directly slowed down to standstill with the aimed decelerations. The test maneuvers for the above mentioned comparison test and identification test are the same with this one.

The specifications of the braking maneuver are listed in Table 4-6. The initial braking speeds are between 160 and 180 km/h depending on the aimed decelerations and performances of the test cars. 50 tests have been done for each configuration with various decelerations from 0.1 to 0.4 g. Thermal effect is not necessary for the modified discs, so each test is started from an initial disc surface temperature of about 50 °C.

Table 4-6: Test maneuver of the vehicle test

Variable	Value
Initial braking speed	160 to 180 km/h
Deceleration	0.1 g to 0.4 g
Initial disc surface temperature	50 °C



## 4.4 Methodology for subjective rating

### 4.4.1 Subjective evaluation system

Because the vehicle acoustics and the human response to noises have already been well investigated, the critical values of SPL for driver's perception are selected by literature research on the general vehicle interior noise level, the masking characteristics, and the humans' subjective perception of noise.

In order to determine the perception threshold values of the accelerations at the driver interface, subjective ratings are executed during the vehicle tests. The subjective evaluation system (Table 4-7) is established based on the 2-level evaluation system traditionally used in the automobile industry. It consists of 10 scales and each scale corresponds to a subjective score. The descriptions of perception are after those in Table 3 of VDI 2057 Part 1<sup>155</sup> and the descriptions of comfort are after those in Annex C of ISO 2631-1<sup>156</sup>.

Table 4-7: Subjective evaluation system

Criterion <sup>157</sup>	Description of evaluation <sup>157</sup>	Description of perception <sup>155,156</sup>	Subjective score
Vehicle in industry standard	currently optimal	not perceptible	10
	very good	threshold of perception	9
	good	just perceptible	8
	still good	easily perceptible, not uncomfortable	7
	satisfying	easily perceptible, threshold of comfort	6
	sufficient	easily perceptible, a little uncomfortable	5
Vehicle under industry standard	deficient	strongly perceptible, fairly uncomfortable	4
	bad	strongly perceptible, uncomfortable	3
	very bad	extremely perceptible, very uncomfortable	2
	totally insufficient	extremely perceptible, extremely uncomfortable	1

<sup>155</sup> VDI 2057 Part 1, 2002-09, p.25.

<sup>156</sup> ISO 2631-1, 1997-05-01, p.25.

<sup>157</sup> cf. Schlecht: Minimierung der Schwingungsempfindlichkeit, 2012, p.47.

### 4.4.2 Subjective rating strategy

Subjective ratings have been conducted for all the driving tests of the three vehicles (vehicle *A*, *B*, and *C*) with the seven modified discs, and for the vehicle tests of the rear brake with a normal brake disc and NAO pads from the comparison test. .

The subjective evaluation strongly depends on the training and experience of test persons. Evaluators must well know how to apply values of a rating. Therefore, considering the large number of vehicle tests, only six persons who have good knowledge about hot judder and the characteristics of the vibrations caused by brake judder have performed the subjective rating. Because one or more peaks could be clearly perceived during one braking process, two subjective scores were given for each test: one for the strongest vibration peak, the other for the general vibration level during the whole braking period aside from the peak. Vibrations of the car body, brake pedal, and steering wheel were separately rated by using the same evaluation system shown in Table 4-7. The subjective evaluation has been focused on the high-order judder induced vibrations. Disturbances from stochastic road excitations were subjectively excluded as far as possible.

## 4.5 Order analysis of hot judder

Order analysis is one of the most important methods used in the following chapters. Therefore, some definitions and phenomena related to the order analysis of hot judder are collectively clarified in this section as a universal methodology.

### 4.5.1 Definition and clarification of the dominant order

The dominant order of hot judder is sometimes neither the same among different characteristic parameters, nor consistent during the entire braking application. For example, Figure 4-15 shows a result of the rear brake with the ECE pads in the drag braking application of the brake dynamometer test.

High amplitudes can be found in the 10<sup>th</sup> to 14<sup>th</sup> orders of BTV, BPV, DTV and LRO. But there is no single order that is always bigger than the other orders. In order to have one unique dominant order for each signal, only the order that has the maximum amplitude during the entire braking time is defined as the dominant order. By this definition, the dominant order of BTV, BPV, and LRO is the 11<sup>th</sup> order, whereas the dominant order of DTV is the 12<sup>th</sup> order in Figure 4-15.

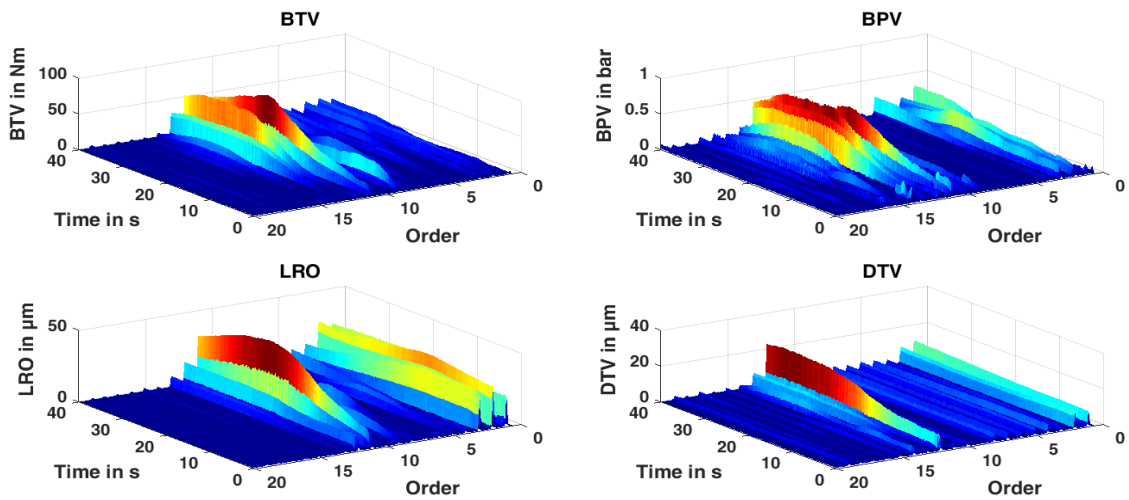


Figure 4-15: Order analysis of a brake dynamometer drag braking application with 225 km/h and 100 Nm (equivalent to 10 bar), the rear brake with the ECE pads in the comparison test

In order to clarify the discrepancy of the dominant orders and the occurrence of the adjacent orders, a thermal image of one disc-rotation at the braking time of 30 s from this test is shown in Figure 4-16. In this test, the temperature variation is much bigger at the finger-side friction ring than that at the piston-side friction ring (but not always so for other tests). 12 hot spots are clearly to see at the finger-side friction ring, but the number of hot spots at the piston-side friction ring can be counted as 11 or 12. Besides, hot spots generally distribute at alternating positions on the two sides, which explains why the amplitude of LRO is bigger than that of DTV for the dominant order. But the distributions on both sides are not absolutely homogenous. In order words, the distances between every two neighbouring hot spots are not a constant value.

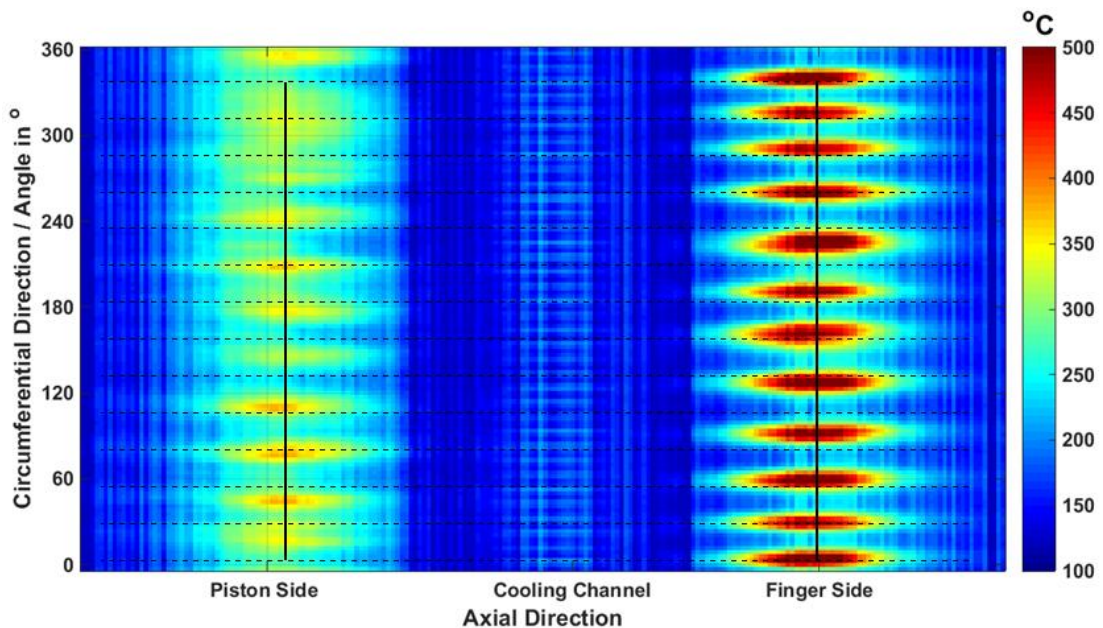


Figure 4-16: Hot spots on the rear brake with ECE pads, drag braking with 225 km/h, 100 Nm, corresponding to  $t = 30$  s of Figure 4-15

For the same rotation, the temperature variations on both sides of the disc at the same disc radius marked by the two black solid lines in Figure 4-16 are displayed in Figure 4-17. The antiphase effect can also be seen from the two curves of temperature variation. The order analyses of the temperature variations (peak-to-peak value) indicate that the 11<sup>th</sup> and 12<sup>th</sup> orders are stronger than the other orders on the piston side, while the 10<sup>th</sup> to 14<sup>th</sup> orders are obviously greater on the finger side for this rotation. The uneven distribution of hot spots generally explains the emergence of the adjacent orders as well as the discrepancy of the dominant orders among DTV, LRO, BPV, and BTV.

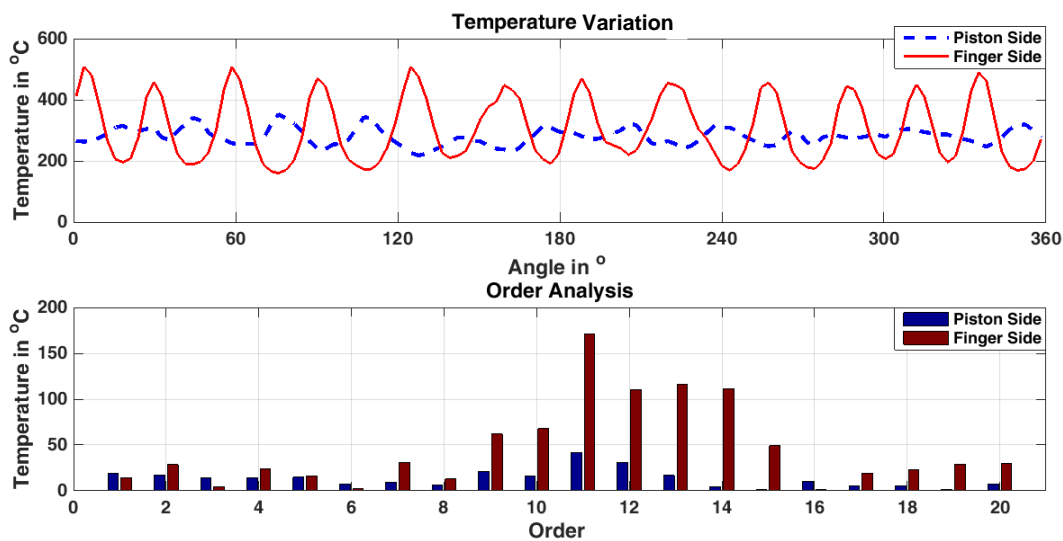


Figure 4-17: Temperature variations at the disc radius marked by the two black solid lines in Figure 4-16 and their order analyses

#### 4.5.2 Mechanism of adjacent orders

As discussed above, unevenly distributed hot spots can lead to adjacent orders of the dominant order. However, adjacent orders can also be induced by “abnormal hot spots” that are obviously stronger or weaker than the other hot spots, as well as by some particular patterns of hot spots forming Amplitude Modulation (AM). The mechanisms of the adjacent orders caused by these circumstances are clarified through order analysis of corresponding artificial signals in the following.

##### Uneven distribution of hot spots

In the thermal images, the occasions that the distances among some hot spots are evidently broader (broader hot spots) or narrower (narrower hot spots) than those among the other hot spots can be frequently detected. The situations of uniform distribution of ten hot spots, non-uniform distribution with two broader hot spots (one hot spot is missing in comparison with the uniformly distributed ten hot spots), and non-uniform distri-

bution with three narrower hot spots (one extra hot spot in the middle of two hot spots) are separately imitated by:

$$y(\varphi) = 100 \sin(10\varphi), \quad 0 \leq \varphi \leq 2\pi \quad (4.5)$$

$$y(\varphi) = \begin{cases} 100 \sin(10\varphi), & 0 \leq \varphi \leq 0.4\pi; 0.8\pi \leq \varphi \leq 2\pi; \\ 100 \sin(5\varphi), & 0.4\pi < \varphi < 0.8\pi \end{cases} \quad (4.6)$$

$$y(\varphi) = \begin{cases} 100 \sin(10\varphi), & 0 \leq \varphi \leq 1.2\pi; 1.6\pi \leq \varphi \leq 2\pi; \\ 100 \sin(15\varphi), & 1.2\pi < \varphi < 1.6\pi \end{cases} \quad (4.7)$$

The three signals and their order analyses are shown Figure 4-18. Only the signals of one disc rotation are given by the three equations above and the number of hot spots is simulated by the number of waves per disc rotation. It is evident that although the numbers of hot spots are different, the dominant orders of these three signals are all the 10<sup>th</sup> order, which is the dominant frequency of the signals. This indicates that the dominant order of hot judder is not always corresponding to the number of hot spots. Besides, both broader and narrower hot spots can lead to adjacent orders. Specifically, lower adjacent orders are mainly generated by the broader hot spots, whereas higher adjacent orders are chiefly caused by the narrower hot spots. In both cases, the amplitude of the dominant order is reduced, comparing with that of the uniformly distributed hot spots.

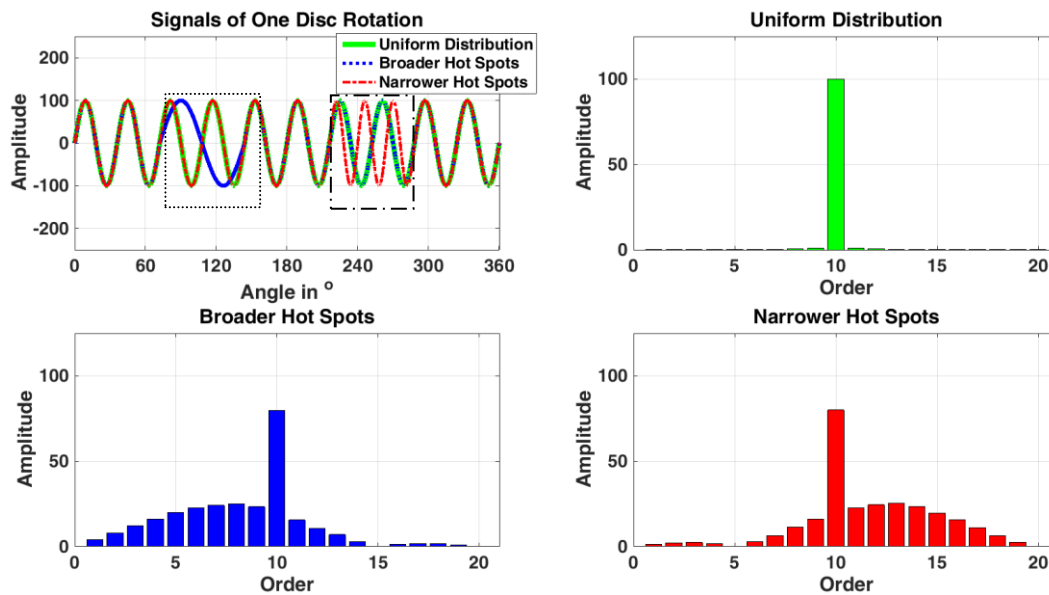


Figure 4-18: Mechanisms of the adjacent orders caused by uneven distribution of hot spots

### Abnormal hot spots

Similarly, the signals of ten uniform hot spots, ten equally distributed hot spots with two stronger ones or two weaker ones are separately simulated by:

$$y(\varphi) = 100 \sin(10\varphi), \quad 0 \leq \varphi \leq 2\pi \quad (4.8)$$

$$y(\varphi) = \begin{cases} 100 \sin(10\varphi), & 0 \leq \varphi \leq 0.8\pi; 1.2\pi \leq \varphi \leq 2\pi; \\ 200 \sin(10\varphi), & 0.8\pi < \varphi < 1.2\pi \end{cases} \quad (4.9)$$

$$y(\varphi) = \begin{cases} 100 \sin(10\varphi), & 0 \leq \varphi \leq 0.8\pi; 1.2\pi \leq \varphi \leq 2\pi; \\ 30 \sin(10\varphi), & 0.8\pi < \varphi < 1.2\pi \end{cases} \quad (4.10)$$

The signals and their order analyses are displayed in Figure 4-19. Both lower and higher adjacent orders are generated by the two kinds of abnormal hot spots, with the stronger hot spots intensifying and the weaker hot spots attenuating the dominant order. Examples of the narrower hot spots and weaker hot spots are attached in Figure B-2.

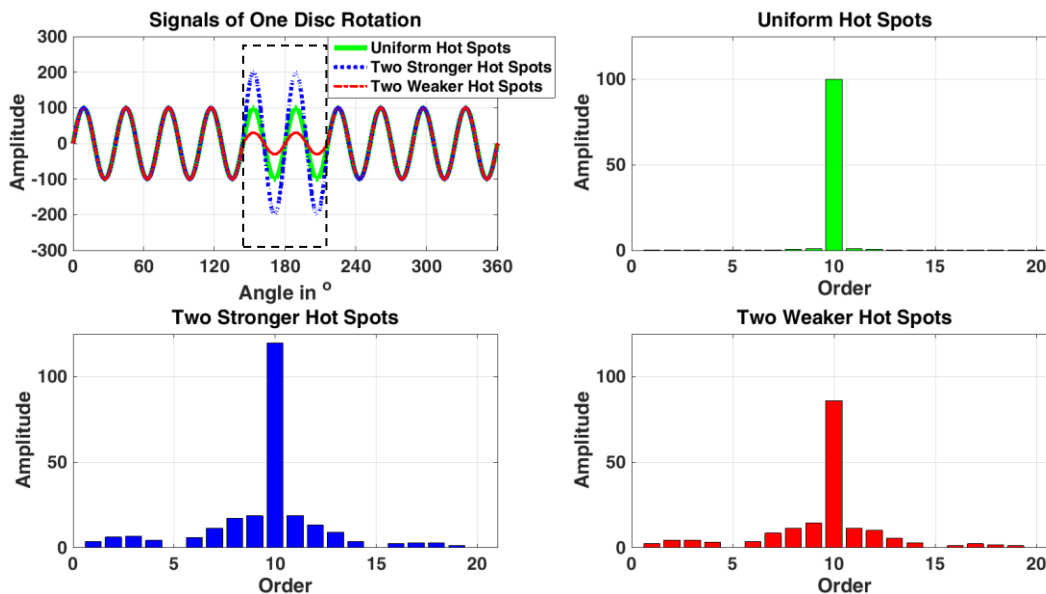


Figure 4-19: Mechanisms of the adjacent orders caused by abnormal hot spots

### AM of hot spots

Figure 4-20 displays a thermal image of one test from Fischer's DOE<sup>158</sup>. It shows clearly 11 or 12 hot spots on both sides of the brake disc. However, the hot spots at the disc positions of approximately 330° to 50° and 180° to 280° are obviously stronger than those at the other regions. Due to the "regular" distribution of hot spots AM is formed.

<sup>158</sup> Fischer et al.: Ordnungsanalyse von Heißrubbeln, 2015

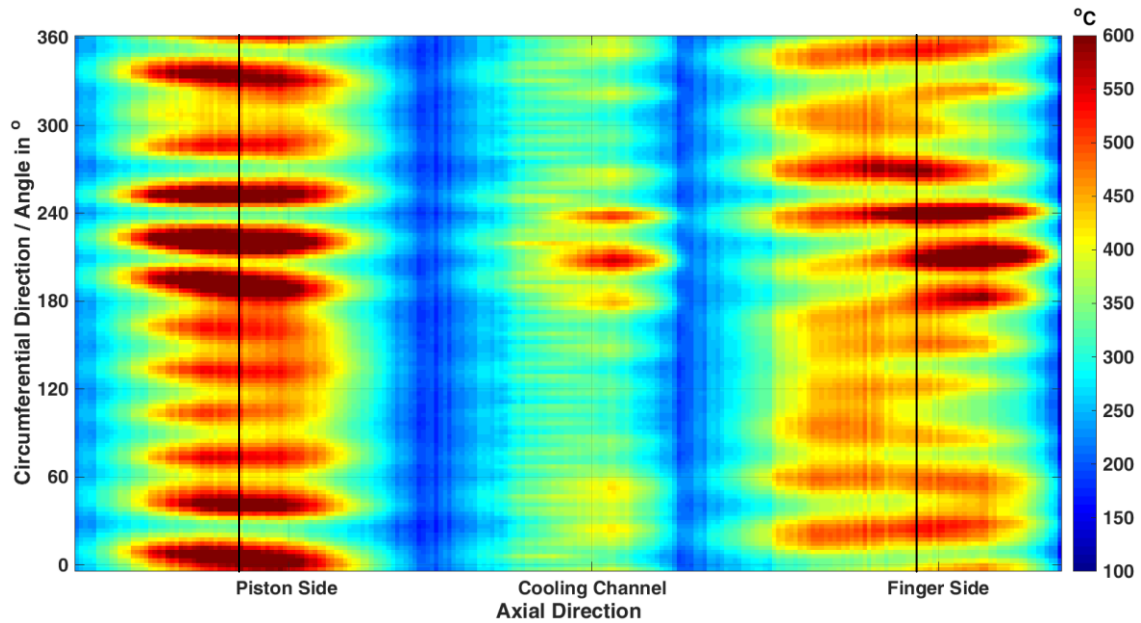


Figure 4-20: Thermal image of one drag braking application with 225 km/h and 250 Nm, 21 s

The thermal variations at the two disc radii marked by the two black solid lines in Figure 4-20 and their order analyses are shown in Figure 4-21. In order to demonstrate the AM caused by this hot-spots pattern, the thermal variations are imitated by the modulated signals composed of a “12<sup>th</sup> order” carrier signal (simulating the 12 hot spots) and a “1<sup>st</sup> order” modulation waveform (simulating the two regional intensifications):

$$y_{piston}(\varphi) = (15 + 140 \sin(\varphi + 0.2\pi)) \cdot \sin(11\varphi + 1.7\pi) + 520 \quad (4.11)$$

$$y_{finger}(\varphi) = (12 + 80 \sin(\varphi + 0.2\pi)) \cdot \sin(11\varphi + 0.7\pi) + 500 \quad (4.12)$$

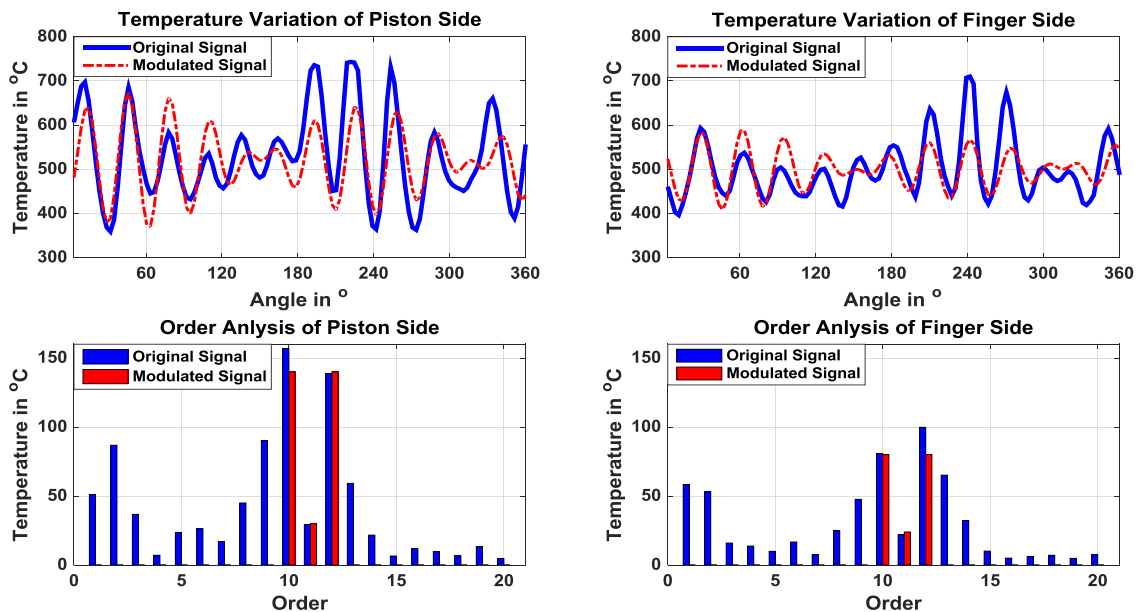


Figure 4-21: Thermal variations and order analyses of the thermal image and the modulated signals

The modulated signals and their order analyses are also added in Figure 4-21. For both original signals and modulated signals, the values in the figures of the order analyses are all peak to peak values. The forms of the thermal variation curves are roughly followed by the modulated signals. In the case of AM, two adjacent orders are induced and they are symmetrically distributed around the order of the carrier signal  $N_{carrier}$  with an interval of the order of the modulation waveform  $N_{modulation}$  :

$$N_{adjacent} = N_{carrier} \pm N_{modulation} \quad (4.13)$$

Taking the two modulated signals in equation 4.13 and 4.14 for example, the 10<sup>th</sup> and 12<sup>th</sup> adjacent orders are produced, with their amplitudes equal to the amplitudes of the modulation waveforms. Besides, since both the amplitudes of hot spots and the distances between hot spots are not uniform, generally the 9<sup>th</sup> to 14<sup>th</sup> adjacent higher orders are induced, which can be seen from the order analyses of the thermal variations in Figure 4-21 and the order analyses of BTV, BPV, LRO, and DTV in Figure B-6.

### 4.5.3 Mechanism of lower-order hot judder

#### Regional thermal increase

In some disc brakes, the macroscopic hot spots are not easily to be excited. Instead, the hot judder effect is mainly reflected by the thermal increases at some specific regions of the brake disc. For example, Figure 4-22 gives the evolution of the hot spots (at 10, 20, 30, and 40 s separately) of the front brake used in the comparison test during one drag braking application. Thermal gradients in the region from about 20° to 70° in the circumferential direction firstly emerge on the brake disc surfaces, and they are always much stronger than the other regions during the entire braking process. Some macroscopic hot spots only become visible after a very long braking time (see the thermal image at 40 s, for example). In such circumstances, the thermal variations are dominant with the lower orders.

For example, the thermal variations at the two disc radii marked by the two black lines in the 30 s thermal image of Figure 4-22 present mainly the 1<sup>st</sup> to 3<sup>rd</sup> order (Figure B-5). Hot judder of this brake is dominant with lower orders, which also can be seen from the order analyses of BTV, BPV, LRO, and DTV from the same test (Figure 4-23). Generally, the 1<sup>st</sup> to 4<sup>th</sup> lower orders are much stronger than the higher orders.



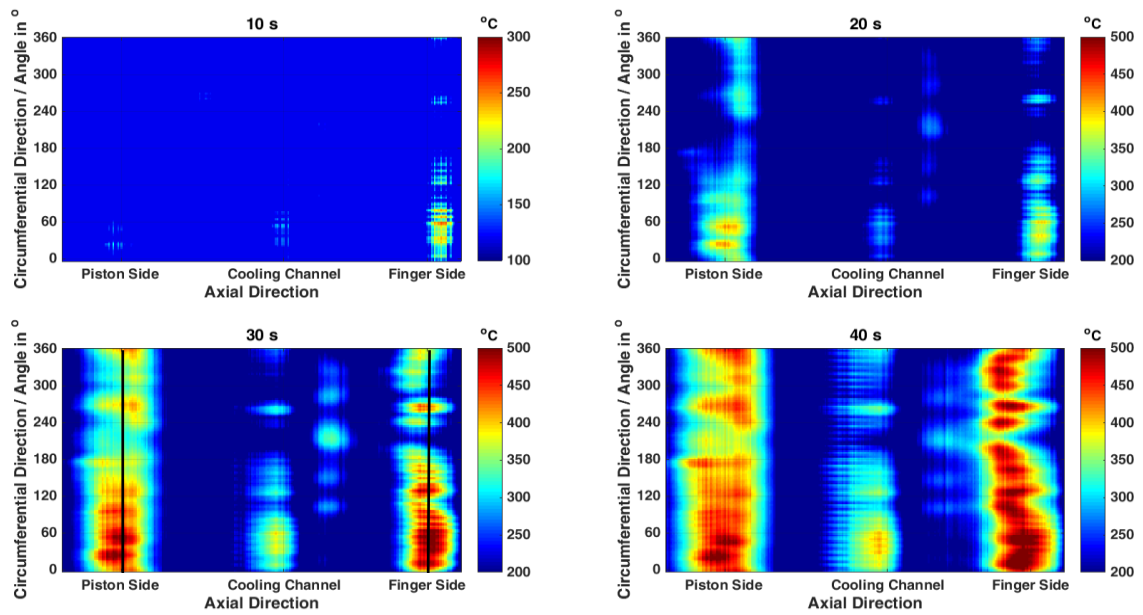


Figure 4-22: Thermal images of one drag braking application with 225 km/h and 10 bar, the front brake in the comparison test

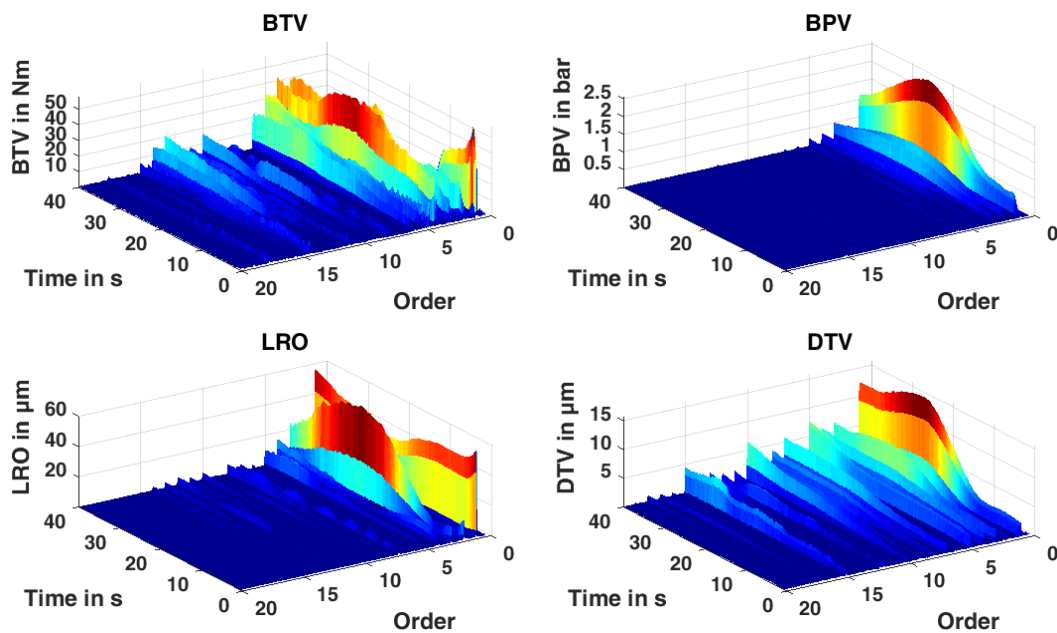


Figure 4-23: Order analyses of BTV, BPV, LRO, and DTV, drag braking of the front brake with 225 km/h and 10 bar

### Superposition of lower and higher orders

In some cases, although a high number of hot spots are excited, the average temperatures at some regions are higher than the other regions. As a result, the temperature variations are the superposition of lower and high orders. Still taking the test in Figure 4-20 for example, the average temperatures at the disc positions of  $330^\circ$  to  $50^\circ$  and  $180^\circ$  to  $280^\circ$ , which are also the positions of the stronger hot spots, are generally higher than

those at the other regions. In order to explain this effect, two “2<sup>nd</sup> order” signals are separately added to the modulated singles in equation 4.11 and 4.12, which are:

$$y_{piston}(\varphi) = 43\sin(2\varphi + 0.2\pi) \quad (4.14)$$

$$y_{finger}(\varphi) = 26\sin(2\varphi + 0.2\pi) \quad (4.15)$$

Consequently, two imitating signals are formed as:

$$y_{piston}(\varphi) = (15 + 140\sin(\varphi + 0.2\pi)) \cdot \sin(11\varphi + 1.7\pi) + 520 + 43\sin(2\varphi + 0.2\pi) \quad (4.16)$$

$$y_{finger}(\varphi) = (12 + 80\sin(\varphi + 0.2\pi)) \cdot \sin(11\varphi + 0.7\pi) + 500 + 26\sin(2\varphi + 0.2\pi) \quad (4.17)$$

The thermal variations at the two disc radii marked by the two black lines in Figure 4-20 and their order analyses, as well as the imitating signals and their order analyses are shown in Figure 4-24. Comparing Figure 4-24 and Figure 4-21, generally the imitating signals fit the original singles better than the modulated signals. Further, since the average temperatures at the disc positions of 180° to 280° are basically higher than those at the positions of 330° to 50°, the original signals should also contain the “1<sup>st</sup> order” signals. This is the reason for the 1<sup>st</sup> order of the original signals (see Figure 4-21 and Figure 4-24).

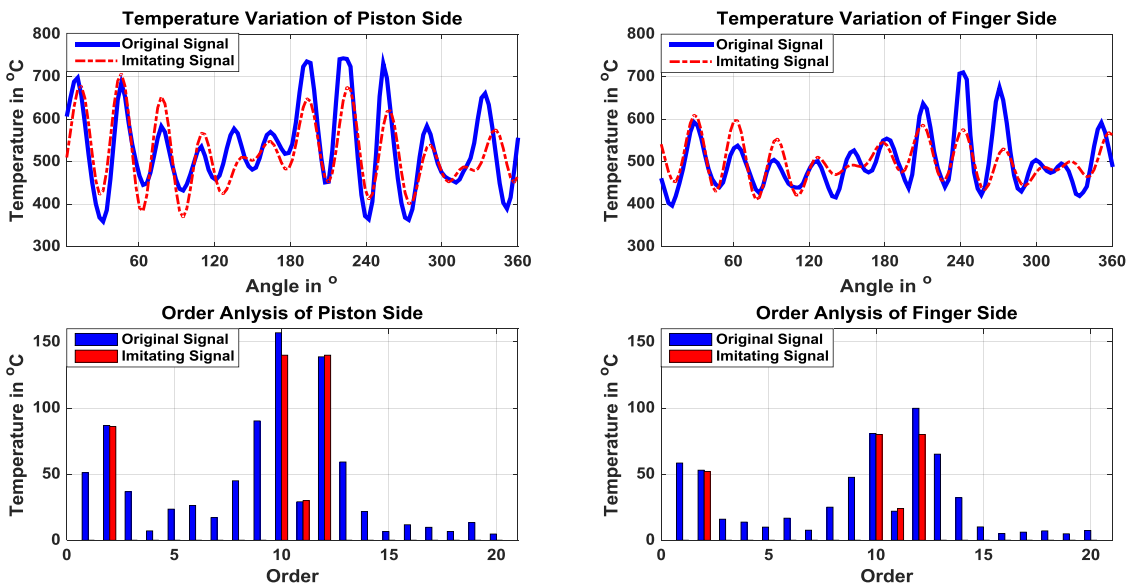


Figure 4-24: Thermal variations and order analyses (peak to peak values) of the thermal image in Figure 4-20 and the imitating signals

#### 4.5.4 Harmonic orders caused by the modified discs

The surface geometries of the modified discs are machined in rectangular forms instead of sine waves. Besides, the ratios between the crests and troughs are not constant at different disc radii for some disc. For example, the ratio of the “10<sup>th</sup>” order 100 μm DTV disc of vehicle A for the radius marked by the dot dash line is 30 % : 70 % (Figure

4-25). From the order analysis of this rectangular signal, it is clear that besides the 10<sup>th</sup> order, higher harmonic orders of 20<sup>th</sup>, 30<sup>th</sup>, 40, 50<sup>th</sup> and even higher order are induced. Although the amplitude of each higher harmonic order is dependent on the forms of the disc surfaces which are changing during braking and on the ratios between the crests and troughs, evident higher harmonic orders, especially the 20<sup>th</sup> and the 30<sup>th</sup> order, are induced in most of the tests with all the modified discs.

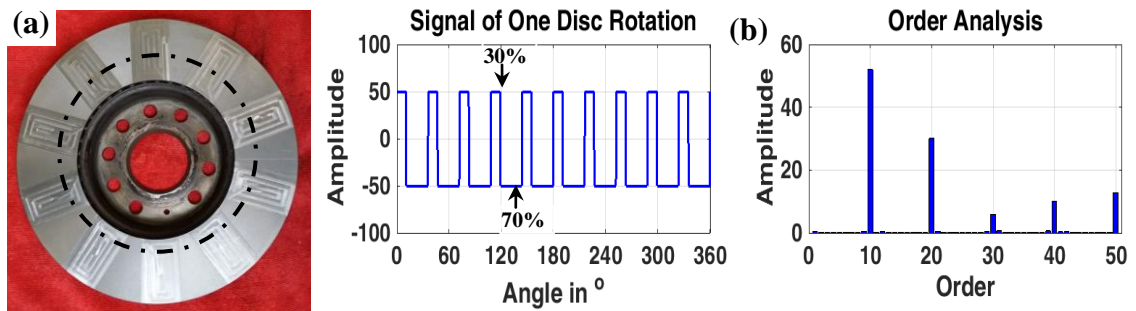


Figure 4-25: (a) The 100 μm DTV disc of vehicle A and (b) the simulated surface form (rectangular signal) and its order analysis

# 5 Transferability from dynamometer test to vehicle test

## 5.1 Evaluation strategy for comparison test

Vibrations at the caliper and the caliper bracket are strongly influenced by some resonance frequencies in the three types of tests, especially in the vehicle tests. Amplitude, frequency and dominant order of the vibrations are not comparable. Therefore, only BTV and BPV are employed as comparison parameters. Specifically, order behaviors of BTV and BPV will be used as qualitative comparison criterion, and amplitudes of the dominant orders of BTV and BPV will be used as quantitative comparison criterion.

Brake judder is actually always a combination of cold and hot judder. In order to compare the behaviors of hot judder, the cold judder effect needs to be excluded. For this sake, evolutions of the first order and the dominant orders of BTV, BPV, LRO, and DTV during a drag braking application (the same test as shown in Figure 4-15) are displayed in Figure 5-1. The lower parts that appear immediately after the beginning of braking are caused by cold judder. The higher parts are the thermal effects that are attributed to hot judder. The thermal increases from the cold judder portion to the maximum amplitude as marked by the arrows in Figure 5-1 will be adopted for the following amplitude comparisons.

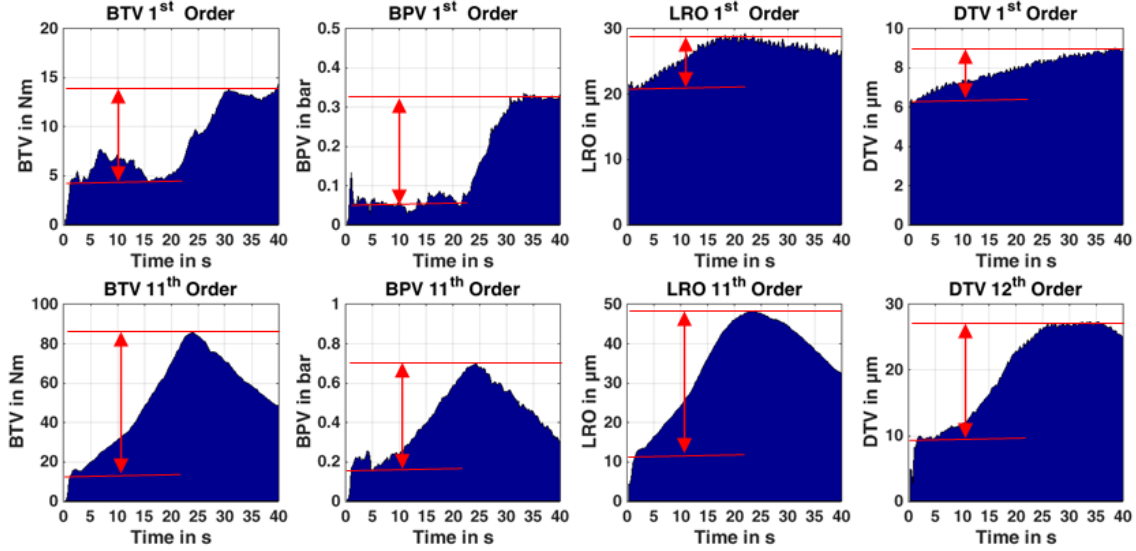


Figure 5-1: Thermal increases of brake judder during a drag braking application with 225 km/h and 100 Nm, the rear brake with ECE pads

## 5.2 Comparison of the front brake

As seen from a test result of the front brake shown in Figure 4-23, high amplitudes are mainly the lower orders in the drag braking applications, for example, the 1<sup>st</sup> to 3<sup>rd</sup> order of BPV and LRO, and the 1<sup>st</sup> to 5<sup>th</sup> order of BTV and DTV in the demonstrated test. Although a few big orders can also be found in some signals (e.g. the 13<sup>th</sup> order of BTV, 10<sup>th</sup> and 15<sup>th</sup> orders of DTV in Figure 4-23) of certain tests, hot judder of the front brake during drag braking is mainly indicated by the thermal increases of the lower orders, especially the first three orders.

During stop braking, evident high-order hot judder is occurring in none of the tests (both dynamometer and vehicle tests) with the front brake. The major orders are generally the 1<sup>st</sup> to 4<sup>th</sup> orders in all the tests (see Figure 5-2, for example). However, the dominant order varies, not only between the brake dynamometer tests and road tests, but also among the dynamometer tests or among the road tests. Still taking the tests in Figure 5-2 for example, the dominant order of the brake dynamometer test is the first order, whereas the second order is the dominant order in the vehicle road test. Although both tests were executed with the same initial braking speed, deceleration and initial disc surface temperature.

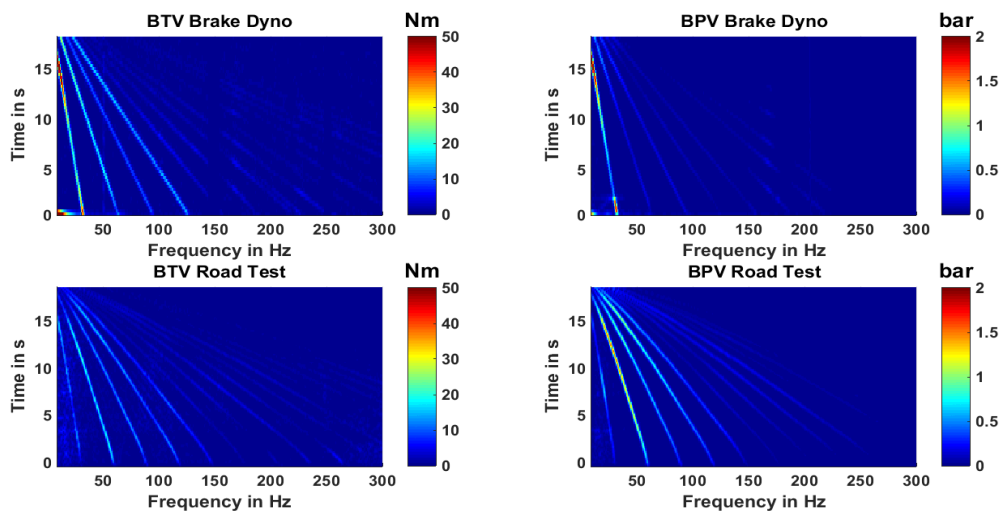


Figure 5-2: Comparison of BTV and BPV orders of the front brake during stop braking from 225 km/h to standstill with 0.3 g and an initial disc surface temperature of 200 °C

Because thermal increases of BTV and BPV are very small in all the tests of the front brake with the initial braking speed of 175 km/h, only the test results with the initial braking speed of 225 km/h are used for the amplitude comparison. As a result, thermal increases of BTV and BPV of the dominant orders are compared in Figure 5-3. Although the tendencies of thermal increases are similar between the two test types, hot judder intensity is generally much stronger in the brake dynamometer tests than that in the vehicle road tests.

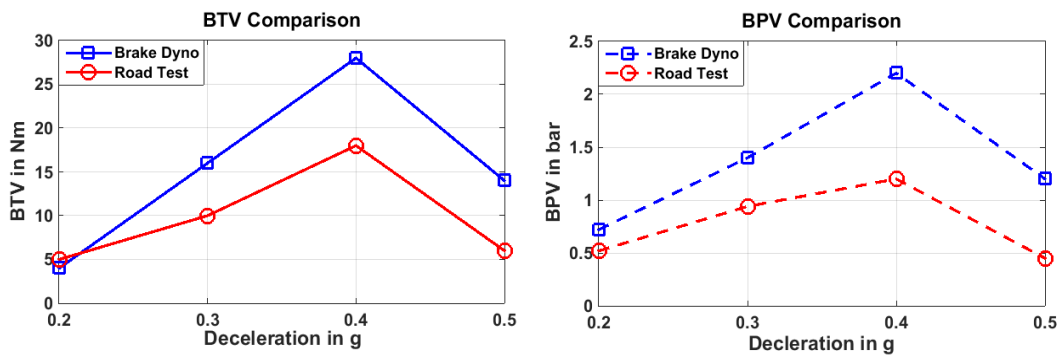


Figure 5-3: Comparison of the thermal increases of BTV and BPV, stop braking applications of the front brake, from 225 km/h with an initial disc surface temperature of 200 °C

## 5.3 Comparison of the rear brake

### 5.3.1 Drag braking application

The rear brake is dominant with higher orders in all the drag braking applications carried out at the brake dynamometer (see one example in Figure 4-15), and the higher dominant orders are also reproduced in the vehicle drag braking tests performed at the chassis dynamometer. Dominant orders of BTV and BPV from the 9<sup>th</sup> to 15<sup>th</sup> order are observed for the two types of brake pads. Hence, for comparing the hot judder behaviors of the rear brake in drag braking applications, thermal increases of BTV and BPV amplitudes of the higher dominant order as well as the higher dominant order of BTV are taken into account.

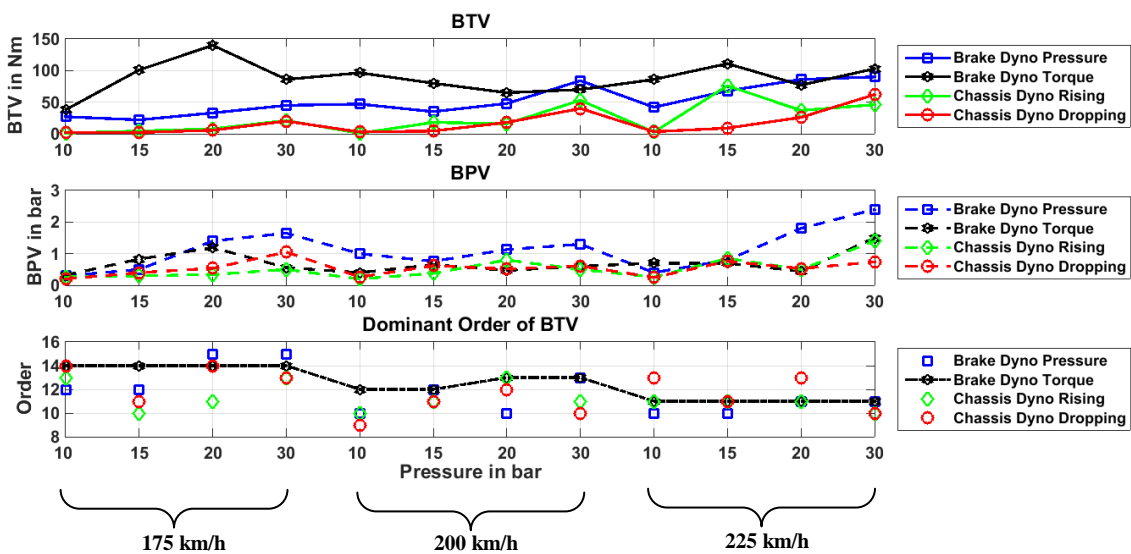


Figure 5-4: Comparison of the thermal increases of BTV and BPV, and the dominant orders of BTV, drag braking applications of the rear brake with ECE pads carried out at the brake dynamometer and the chassis dynamometer, from 100 to 500 °C

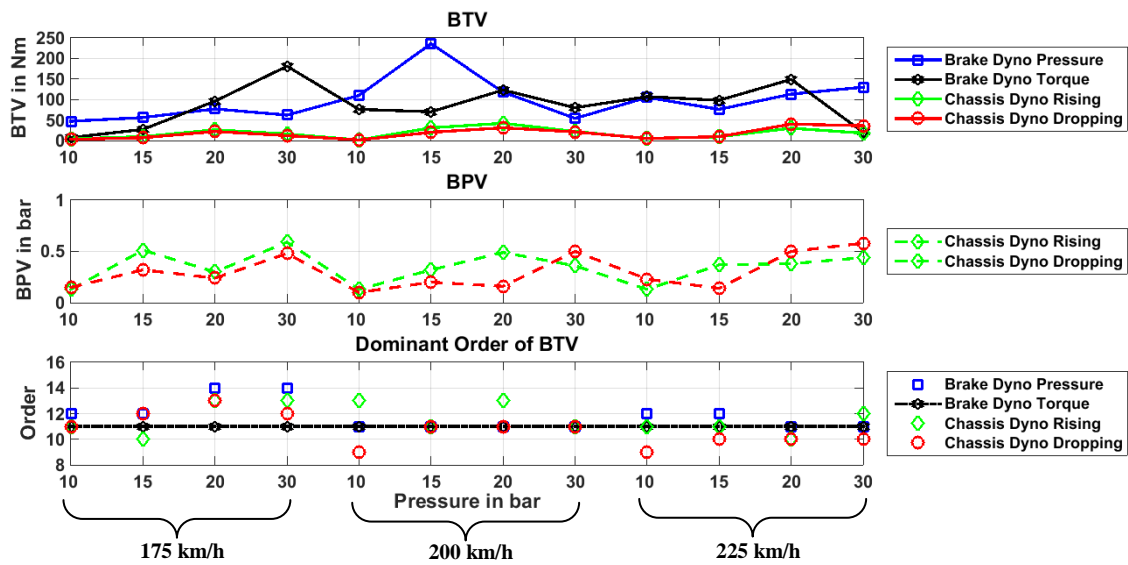


Figure 5-5: Comparison of the thermal increases of BTV and BPV, and the dominant orders of BTV, drag braking applications of the rear brake with NAO pads carried out at the brake dynamometer and the chassis dynamometer, from 100 to 500 °C

Results of the two types of brake dynamometer tests (with constant pressure or constant torque) and the two test programs of chassis dynamometer tests (in the sequence of rising velocity and pressure or in the adverse sequence) regarding the two pairs of brake pads are respectively shown in Figure 5-4 and Figure 5-5. The BPV values at the brake dynamometer for the tests with the NAO pads are much smaller than the vehicle test results, so they are not shown in Figure 5-5. From the results in the two figures, following conclusions can be drawn:

- Comparing the two different control methods at the brake dynamometer, BTV and BPV behaviors of the two pairs of pads show great discrepancies in many operating points, not only for the amplitudes but also for the dominant orders. This is true especially for the tests with the ECE pads. Hot judder behaviors at the brake dynamometer are strongly influenced by the control method: with constant pressure or with constant torque.
- Regarding the two test programs at the chassis dynamometer, thermal increases of BTV and BPV are basically reproducible. Amplitudes of BTV and BPV are comparable at most operating points for the both pads. Sequence of the test conditions does not show evident influences on the hot judder intensity.
- On the whole, hot judder intensity is much stronger in the brake dynamometer tests than that in the chassis dynamometer vehicle tests when comparing the amplitudes of BTV and BPV. Considering the similar hydraulic systems in the brake dynamometer and the vehicle, this effect is most likely to be caused by the different cooling rates of the brake discs (the cooling rate in the vehicle was

higher than that in the brake dynamometer in the tests performed under the same testing conditions) or the different supporting stiffness of the wheel brakes.

- The dominant order of BTV is not constant in the tests with both pads. It varies not only among different operating points, but also among various tests at the same operating point. Besides, some phenomena exhibited in the brake dynamometer tests conducted with constant brake torque are neither reproducible in the chassis dynamometer tests, nor reproducible in the dynamometer tests with constant brake pressure. For example, the constant frequency phenomenon in the tests with the ECE pads (the judder frequency keeps constant under changing velocities, e.g. 175 km/h with the 14<sup>th</sup> order, 200 km/h with the 12<sup>th</sup> or 13<sup>th</sup> order, and 225 km/h with the 11<sup>th</sup> order all happen around 340 Hz, see the dotted line in the third plot of Figure 5-4), and the constant order phenomenon in the tests with the NAO pads (the judder order keeps constant under varying velocities, see the dotted line in the third plot of Figure 5-5).

### 5.3.2 Stop braking application

Generally hot judder is more likely to be excited in the drag braking applications, because there is higher thermal energy input into the brake disc by longer braking with a high constant rotational speed. One example of the rear brake test results with the ECE pads in the three types of stop braking applications is shown in Figure 5-6.

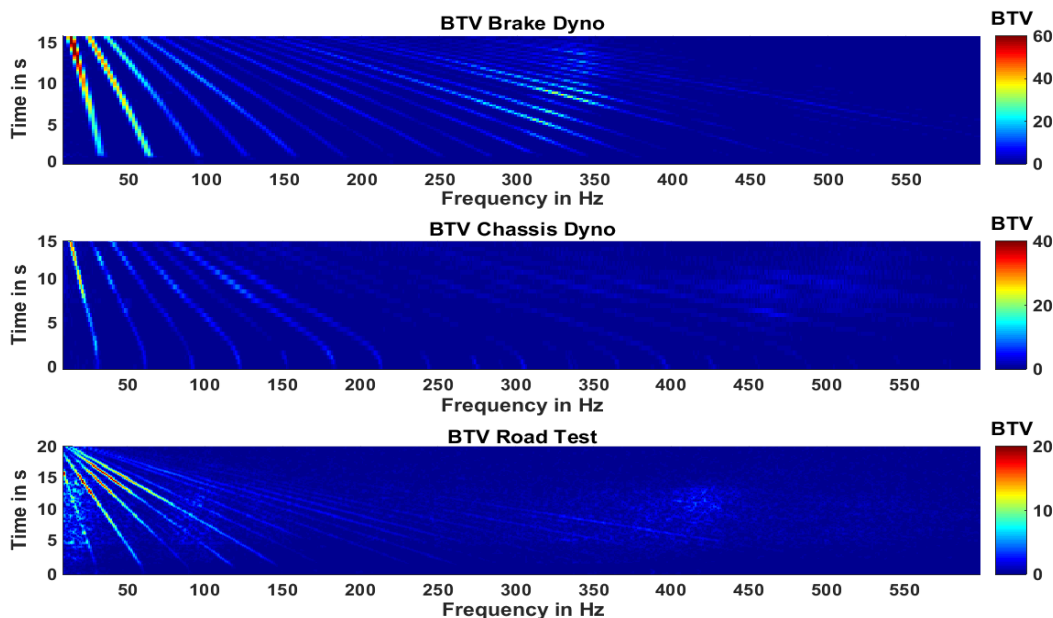


Figure 5-6: Hot judder behaviors in the stop braking applications of the rear brake with the ECE pads, from 225 km/h and 200 °C with 0.3 g

Although they are all dominant with the lower orders (1<sup>st</sup> to 5<sup>th</sup> order), some peaks around the frequency of 340 Hz are visible in the brake dynamometer test. By this



phenomenon and the constant frequency phenomenon of the drag braking applications executed with the ECE pads, it is speculated that hot judder of the rear brake is closely associated with a resonance frequency at about 340 Hz. In addition, by further comparing the thermal increases in the lower dominant order of BTV and BPV displayed in Figure 5-7, it can be concluded that hot judder occurring propensity in the three kinds of tests is: brake dynamometer test > vehicle chassis dynamometer test > vehicle road test.

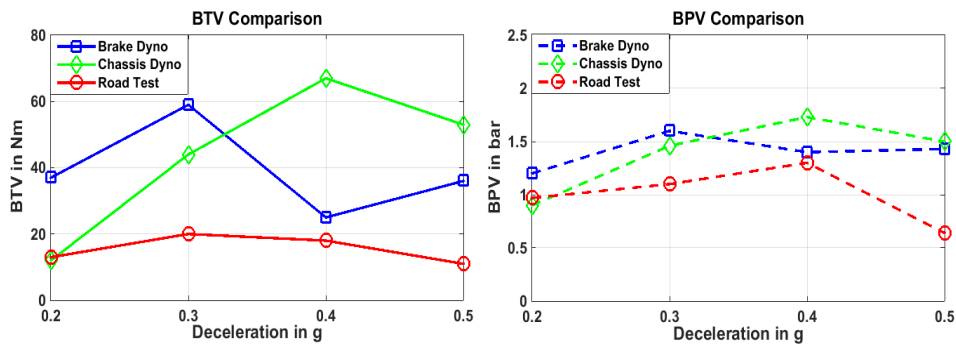


Figure 5-7: Comparison of BTV and BPV amplitudes, stop braking applications of the rear brake with ECE pads, from 225 km/h with an initial disc surface temperature of 200 °C

## 5.4 Results of the modification test

In order to examine the influence of the stiffness of knuckle adapter on the hot judder behaviors, thermal increases of the dominant orders and the dominant orders of BTV, BPV, LRO, and DTV are compared for the test results by using the two adapters. Figure 5-8 shows the comparison of the thermal increases. The test results of the drag braking application with the two test programs (constant pressure, or constant torque) are shown. Although there are great discrepancies at some operating points, the dependency of thermal increases on the adapter stiffness is not definite.

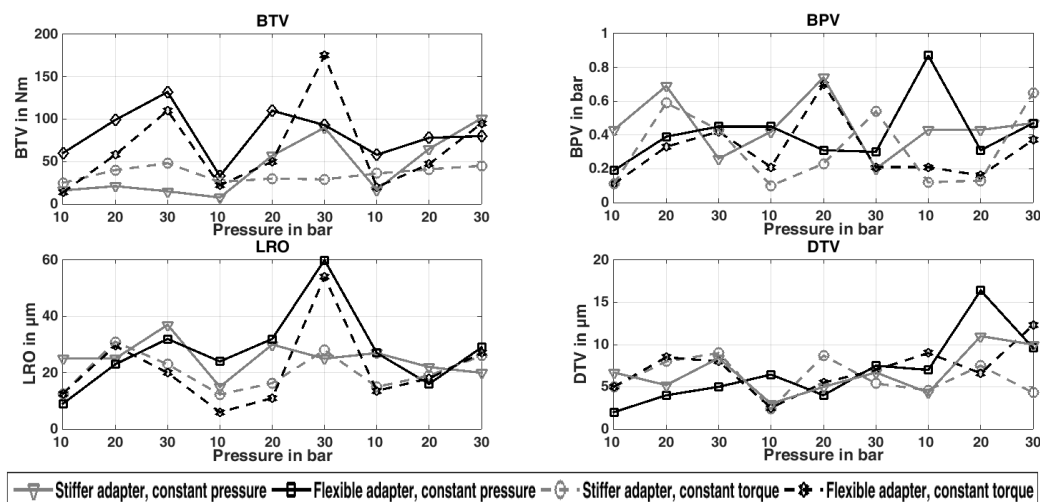


Figure 5-8: Influence of the knuckle adapter stiffness on hot judder intensity

In order to indicate the dependency, discrepancy of the thermal increase is calculated by using Equation 5.1 and displayed in Figure 5-9.

$$Discrepancy_x = \frac{(x_{stiffer} - x_{flexible})}{(x_{stiffer} + x_{flexible}) / 2}, \quad (x = BTV, BPV, LRO, DTV) \quad (5.1)$$

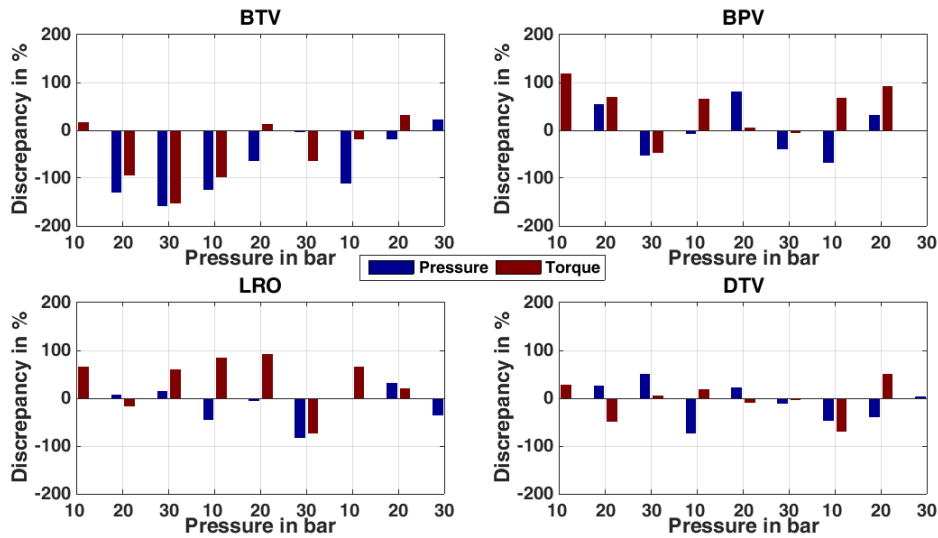


Figure 5-9: Dependency of thermal increases on the knuckle adapter stiffness

Besides, the influence of the adapter stiffness on the order behaviors is also not uniform. 11-16 hot spots are generated in the drag braking applications, but the dominant orders are neither reproducible among the tests with the same adapter under various testing conditions, nor reproducible between the tests with the two different adapters under the same testing conditions (see Figure C-).

## 5.5 Results of the identification test

As main result of the identification test, no evident high-order hot judder has been detected in all the wheel brakes of the four passenger cars. In most brakes, only low-order judder was found, as indicated by a test result of the front left brake of “vehicle B” in Figure 5-10 (a). High order judder was only detected in the front left brake of “vehicle C”, as shown in Figure 5-10 (b). However, there was no single order that is always remarkable at all frequencies in this brake. Some orders are only visible when passing through the resonance frequencies of the vehicle. The vehicle B and C mentioned here are the same with those vehicle B and C used in the investigation of high-order judder transfer behaviors.

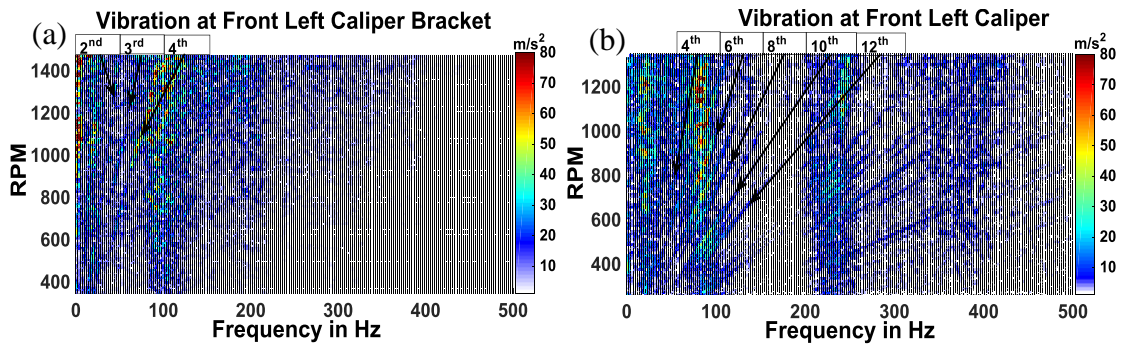


Figure 5-10: (a)Vibration at front left caliper of vehicle *B*, from 180 km/h and 185°C with 0.31g  
 (b)Vibration at front left caliper bracket of vehicle *C*, from 175 km/h and 205 °C with 0.33 g

---

## 6 Transfer behaviors of high-order judder

In this chapter, the transfer behaviors of the high-order judder are studied by identifying the global transfer functions from BPV/BTV to the driver interface quantities through vehicle roads tests with modified discs. Based on the coherence analysis, the global transfer functions are computed by extracting the order lines of input and output signals from their spectral diagrams. Since 50 tests have been carried out for each configuration, statistical qualities of the identified transfer functions are investigated. As a result, the sample means are adopted as the final transfer functions of corresponding transfer paths. Moreover, the reproducibility of the calculated transfer functions is studied by examining the influential factors, such as different orders, discs, and the braking deceleration. The basic analysis methodology is mainly demonstrated by using one example of the test with vehicle *B*. Besides, the transfer mechanisms of drone noise are clarified based on the assumed transfer paths.

### 6.1 Determination of transfer functions

#### 6.1.1 Time signals and spectral analysis

One test of vehicle *B* with 60  $\mu\text{m}$  artificial DTV disc shown in Figure 4-10 (a) is taken as example in the following. The braking maneuver of this test is decelerating with 0.31  $g$  from 180 km/h to standstill. The time courses of velocity, deceleration, BTV, and BPV are displayed in Figure 6-1. Braking pressure and braking deceleration were held relatively constant during the entire braking process. The amplitudes of BTV and BPV were also fairly constant, which means the thermally induced DTV was minor for the tests with the initial braking temperature of 50  $^{\circ}\text{C}$ .

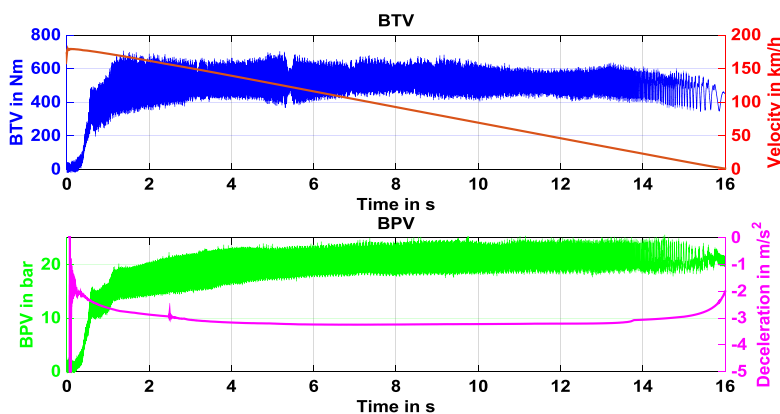


Figure 6-1: BTV and BPV time signals of one test with vehicle *B*,  $\Delta d_D \approx 60 \mu\text{m}$

Figure 6-2 shows the spectral analyses of the relevant signals. They are calculated by short-time Fourier transform with a Hanning window of 0.25 s and an overlap of 50%. Besides the 10<sup>th</sup> order, higher harmonic waves of 20<sup>th</sup>, 30<sup>th</sup> and even higher orders are also visible. For example, the 10<sup>th</sup>, 20<sup>th</sup>, 30<sup>th</sup>, and 40<sup>th</sup> order of BTV are indicated in the spectral diagram. Because the sampling rate of the WFS is 1 kHz, folding of higher orders is caused due to the aliasing effect. An antialiasing filter is used to the signals acquired by the WFS (e.g. BTV and the three forces in Figure 6-2), so as to eliminate the folding effect. The basic principle of the antialiasing filter is explained in C.2, by taking the BTV signal for example.

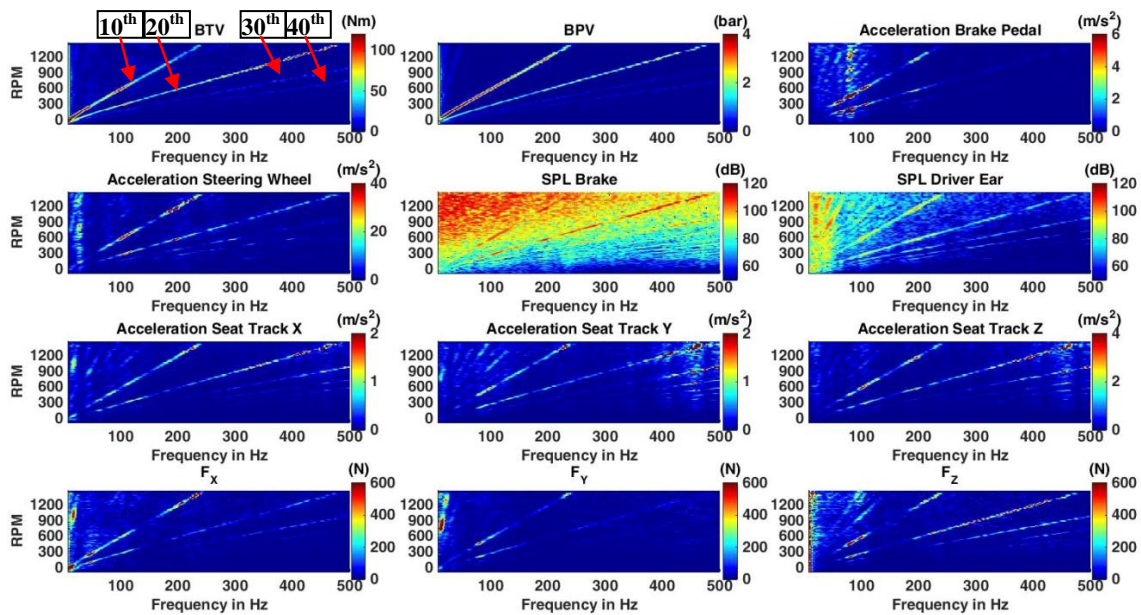


Figure 6-2: Spectral diagrams of the test result with vehicle *B*,  $\Delta d_D \approx 60 \mu\text{m}$

Regarding the vibrations at the driver interface, the steering wheel oscillation is strongest, followed by the brake pedal pulsation, while the seat track vibrations are much less. Concerning the vibrations at the seat track, the longitudinal and transverse vibrations are of comparable order of magnitude, with vertical vibration much stronger. However, the wheel force variation in the transverse direction is generally smaller than that in the longitudinal directions. This means that vehicle *B* is more sensitive in the transverse direction than in the longitudinal direction for the one-side excitation of high-order judder. The transmission sensitivity of the transfer paths will be further depicted by the transfer functions in the following.

With respect to the drone noise, the 10<sup>th</sup>, 20<sup>th</sup> and higher orders are clearly visible in the wheel brake SPL spectrum and the vehicle interior SPL spectrum, despite the high vehicle noise level (mainly on account of the wind noise and the tire-road noise) during the tests. It illustrates that drone noise caused by the high-order judder is evidently stronger than the other noises for this configuration, especially in the frequency range higher than 100 Hz. Thus it was easily hearable from the whole vehicle noises. Besides,

a few resonance frequencies can be dug out from some driver interface signals. The vibrations and noise are intensified by the resonances. The resonance effects of the driver interface signals can be better seen in the time signals in Figure C-4.

### 6.1.2 Coherence analysis

A high coherence is the precondition for a useful transfer function consideration. The coherence between two signals is a real-valued function of frequency, defined as<sup>159</sup>:

$$C_{xy}(f) = \frac{|P_{S_{xy}}(f)|^2}{P_{S_{xx}}(f)P_{S_{yy}}(f)} \quad (6.1)$$

where  $x$  and  $y$  are two signals with the same length,  $P_{S_{xx}}(f)$  and  $P_{S_{yy}}(f)$  are the power spectral densities of  $x$  and  $y$ , and  $P_{S_{xy}}(f)$  is the cross power spectral density of  $x$  and  $y$ . Values of coherence will always satisfy  $0 \leq C_{xy}(f) \leq 1$ , which indicates how well two signals correspond with each other at each frequency. For linear systems, the coherence function can be interpreted as the fractional portion of the mean square value at the output  $y(t)$  that is contributed by the input  $x(t)$  at frequency  $f$ . Conversely, the quantity  $1 - C_{xy}(f)$  is a measure of the mean square value of  $y(t)$  not accounted for by  $x(t)$  at frequency  $f$ <sup>159</sup>.

Coherences between the inputs (BPV/BTV) and the outputs (accelerations or sound pressure) of the above defined transfer functions should be smaller than one, since:

- There is extraneous noise in the measurement of the inputs and outputs (e.g. the aliasing effect in the BTV measurement);
- The systems of the transfer paths are not absolutely linear;
- The outputs are not only caused by the input, but also by other unmeasured inputs (e.g. road excitation, engine vibration, brake judder from other brakes, out-of-balance tires and et al.).

Coherence analyses among the input signals and output signals of the sample test are shown in Figure 6-3. These diagrams are generated by computing the coherences between the input and output signals with sliding windows of every ten disc rotations and overlaps of nine rotations. For the coherence calculation between BTV and the drone noise, sound pressure instead of the logarithmic quantity of SPL is used. In all the diagrams, coherences for the 10<sup>th</sup> and 20<sup>th</sup> orders are higher than 0.8 at most frequencies. Therefore, both the 10<sup>th</sup> and the 20<sup>th</sup> order signals can be used for the estimation of the transfer functions.

---

<sup>159</sup> Bendat und Piersol: Random data, Section 6.1.2, 2010, p.180.

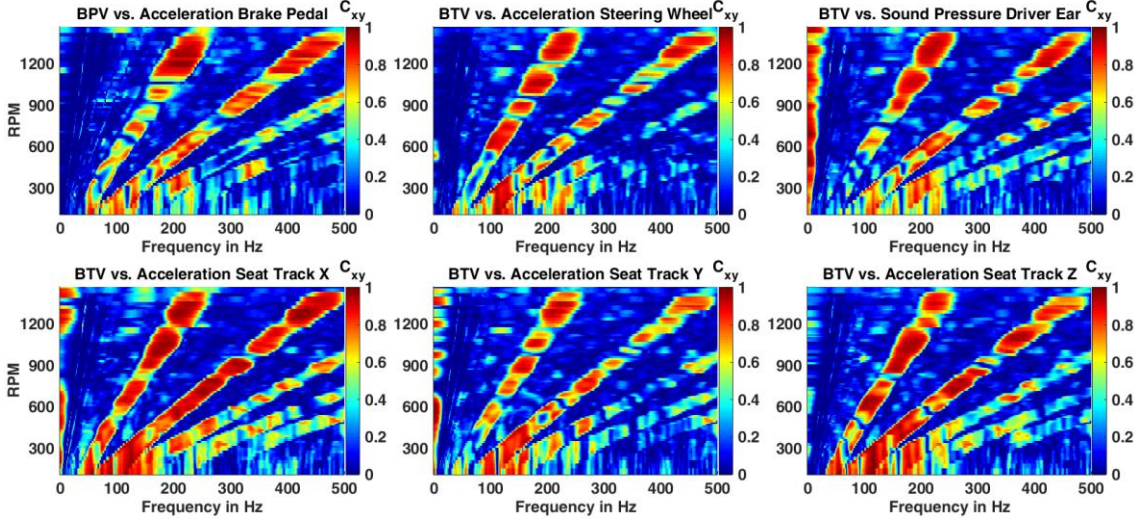


Figure 6-3: Coherence analyses among the signals of the sample test, one test of vehicle *B*,  $\Delta d_p \approx 60 \mu\text{m}$

### 6.1.3 Calculation of the transfer functions

Transfer functions of the 10<sup>th</sup> order and 20<sup>th</sup> order are separately calculated by dividing the 10<sup>th</sup> and 20<sup>th</sup> order lines of the input signals with the output signals in the frequency domain. The order lines in the frequency domain are the projections of the order lines in the spectral diagrams of Figure 6-2 onto the frequency axis.

Regarding the order line extraction method, specifically, for each rotational speed  $n_j$  and order  $N$ , one corresponding frequency can be calculated by  $f_{n_j, N}^* = n_j \times N$ . Because the frequency resolution used in the spectral analysis is 1 Hz, the nearest integer frequency  $f_{n_j, N}$  of  $f_{n_j, N}^*$  is then defined as the center frequency. Since the values on the rotational speed axis of the spectral diagrams are the average values of each time window, the point  $(f_{n_j, N}, n_j)$  might not exactly lie on the  $N^{\text{th}}$  order line in the  $[f, n]$  matrix. In order to find the point exactly on the order line, amplitudes of the five points centered with the center frequency on the same rotational speed line are compared. The one with the maximum amplitude is finally determined as the target point of the order line, which can be expressed as:

$$(f_{\text{target}}, n_j) = \max(\text{Amp}(f_i, n_j)), \quad f_i = f_{n_j, N} - 2, f_{n_j, N} - 1, f_{n_j, N}, f_{n_j, N} + 1, f_{n_j, N} + 2 \quad (6.2)$$

where  $j$  is the index of the rotational speed array  $\mathbf{n}$ . Taking the 10<sup>th</sup> order line of BTV signal for example, the whole process is illustrated in Figure 6-4.

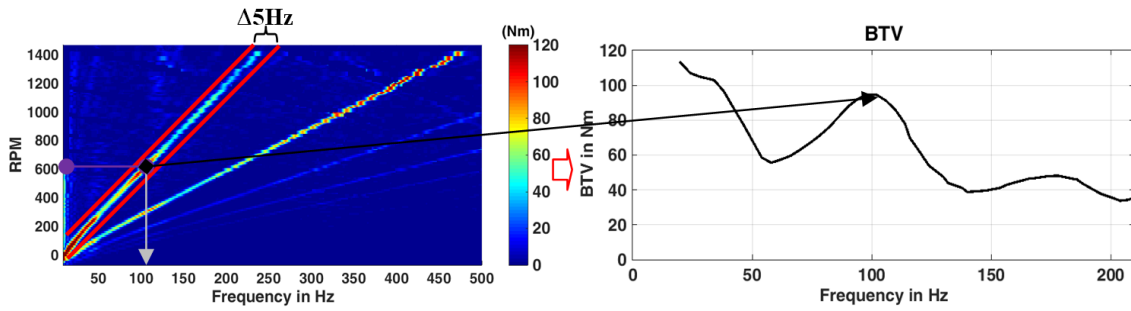


Figure 6-4: Order line extraction process

By using this method, for example, the transfer functions of BTV causing the vertical seat track vibrations are calculated with the 10<sup>th</sup> order lines for all of the 50 tests, as displayed in Figure 6-5. The curves are relatively close to each other, except in the ranges of resonance frequencies and in the initial phases of the braking applications.

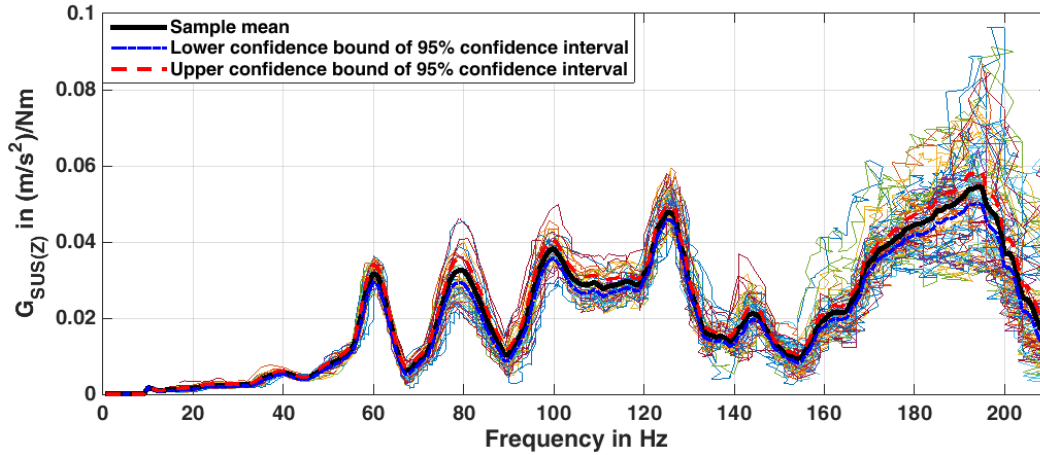


Figure 6-5: Transfer functions of BTV causing vertical seat track vibration, 50 tests of vehicle *B*,  $\Delta d_D \approx 60 \mu\text{m}$

Since 50 tests have been carried out for each configuration, statistical quality of the test results is studied. It is supposed that the test results of the transfer function as a population  $X$  that follows the normal distribution, which is suitable for the statistical estimation of measured quantities containing errors. Given this assumption, the maximum likelihood and confidence interval of the 50 transfer functions can now be calculated. For a normal distribution  $N(e, \sigma^2)$ , the maximum likelihood of  $e$  and  $\sigma^2$  are calculated with:

$$\hat{e} = \frac{1}{Ns} \sum_{i=1}^n X_i \quad (6.3)$$

$$\sigma^2 = \frac{1}{Ns} \sum_{i=1}^n (X_i - \bar{X})^2 \quad (6.4)$$

where  $Ns$  represents the sample size. The sample mean  $\bar{X}$  and the sample variance  $S^2$  are calculated with:



$$\bar{X} = \frac{1}{N_s} \sum_{i=1}^n X_i \quad (6.5)$$

$$S^2 = \frac{1}{N_s - 1} \sum_{i=1}^n (X_i - \bar{X})^2 \quad (6.6)$$

It is obvious that for a normal distribution, the maximum likelihood of expectation  $\hat{e}$  is equal to the sample mean  $\bar{X}$ . Thus the pivotal quantity  $U = \frac{\bar{X} - e}{S / \sqrt{N_s}}$  has a Student's  $t$ -distribution with  $N_s-1$  degrees of freedom<sup>160</sup>. The confidence interval of  $e$  with a confidence level of  $1 - \alpha$  is  $[\bar{X} - \frac{S}{\sqrt{N_s}} t_{\frac{\alpha}{2}}(N_s - 1), \bar{X} + \frac{S}{\sqrt{N_s}} t_{\frac{\alpha}{2}}(N_s - 1)]$ , where  $t_{\frac{\alpha}{2}}(N_s - 1)$  is the  $(1 - \frac{\sigma}{2})$  quantile of the  $t(N_s - 1)$ -distribution. For example, for 50 tests with the 95% confidence level:  $(N_s = 50, \alpha = 5) \rightarrow t_{2.5}(49) = 2.010$ .

Consequently, the maximum likelihood (which is equal to the sample mean) and the 95% confidence interval are computed and also added to Figure 6-5. On the whole, the 95% confidence interval obtained with the 50 tests is only a narrow band. Hence, to make things simpler, the sample means (i.e.  $\bar{X}$ ) are used as the representative transfer functions of the transfer paths.

Moreover, in order to have a wider frequency range, the 20<sup>th</sup> order is used to calculate the final transfer functions. As a result, the six transfer functions of the three vehicles (drone noise was not measured in vehicle A) are calculated and displayed in Figure 6-6.

The discs used in the calculations for each vehicle are: 100  $\mu\text{m}$  DTV disc (Figure 4-11 (a)) in the front left brake of vehicle A, 60  $\mu\text{m}$  DTV disc (Figure 4-10 (a)) in the front left brake of vehicle B, 60  $\mu\text{m}$  DTV disc (Figure 4-11 (b)) in the front left brake of vehicle C, 30  $\mu\text{m}$  DTV disc (Figure 4-11 (e)) in the rear left brake of vehicle C.

From the curves of the transfer functions, following conclusions can be drawn:

- Regarding the transferability of the three vehicles from the front left brakes to the driver interfaces, although the shapes of the transfer function curves in each transfer path show clear differences among different vehicles, their overall amplitudes are generally on a similar level. And the transfer function curves are relatively flat on the whole after 100 Hz, especially for those from BTV to the steering wheel oscillation and from BTV to the seat track vibrations in the three directions. It reflects that the transmissibility of the transfer paths does not greatly change in the high-frequency range. However, comparing the sensitivity of

<sup>160</sup> Rees: Essential statistics, Section 9.5, 2001, p.89.

vehicle *C* to the high-order judder occurring in the front left brake and the rear left brake, it is generally much higher for the front brake than the rear brake, except for the transmission of drone noise.

- Generally, the sensitivity of the steering systems is much higher than that of the suspension systems for the transfer of the high-order judder from the front brakes. With respect to the high-order judder in the rear brake, although the steering wheel oscillation is also excited (see the spectral diagram of one test with 40  $\mu\text{m}$  LRO disc in the rear left brake of vehicle *C* in Figure C-5), the transferability of the steering system is not obviously higher than that of the suspension system. Hence, the steering wheel oscillation should be resulted in by the yaw motion of the whole vehicle due to the one-side judder excitation.
- Concerning the sensitivities of the suspension system in the three directions, the vehicles are generally more sensitive in the vertical and transverse directions than in the longitudinal direction. It is especially true when only considering the transmissions from the front brakes.
- In addition, there are plenty of resonance frequencies in all the transfer paths, manifested by the peaks in the curves. Mitigation of these resonance effects would greatly reduce the sensitivity of vehicles to the high-order hot judder. The resonance frequencies in vehicle *C* were identified through a supervised master thesis<sup>161</sup>, in order to inspect the sources of the resonance frequencies.

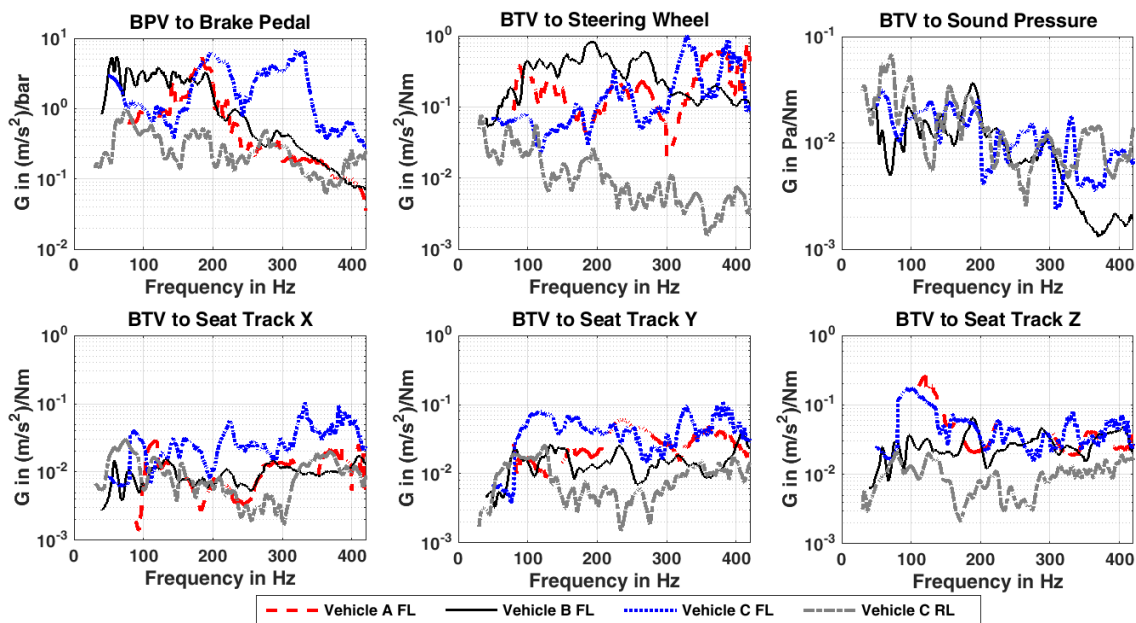


Figure 6-6: Transfer functions from BPV/BTV to the driver interface quantities for the three vehicles

<sup>161</sup> Du: Identifikation der Heißrubbeln-beeinflussenden Eigenfrequenzen, 2015

### 6.1.4 Reproducibility of the results

Still taking vehicle *B* as an example, in order to examine the reproducibility of the identified transfer functions, the 95 % confidence levels of the transfer functions of the same tests with the 60  $\mu\text{m}$  DTV disc calculated by the 10<sup>th</sup> and 20<sup>th</sup> order, as well as the results of the 60  $\mu\text{m}$  DTV and 100  $\mu\text{m}$  LRO discs calculated by the 20<sup>th</sup> order are respectively compared and shown in Figure 6-7 and Figure 6-8.

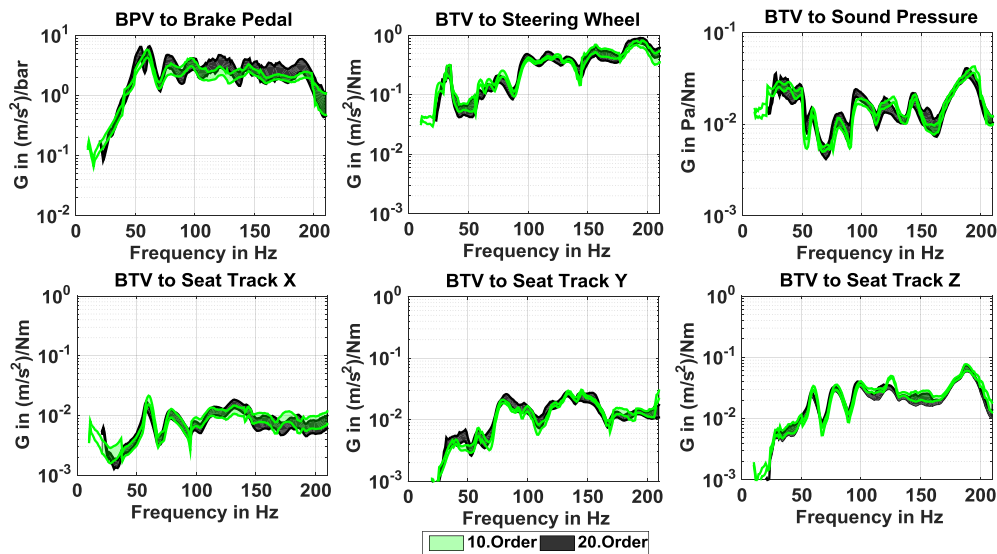


Figure 6-7: Comparison of transfer functions calculated by the 10<sup>th</sup> and 20<sup>th</sup> order,  $\Delta d_D \approx 60 \mu\text{m}$ , vehicle *B*

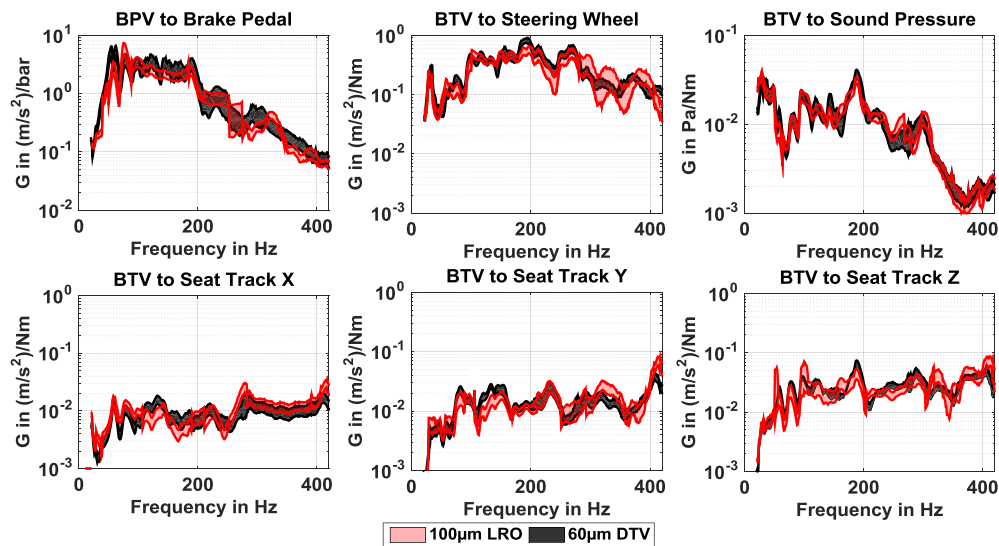


Figure 6-8: Comparison of the transfer functions identified by two different brake discs of vehicle *B*, calculated with the 20<sup>th</sup> order,  $\Delta d_D \approx 60 \mu\text{m}$ ,  $\Delta z_D \approx 100 \mu\text{m}$

Good reproducibility is manifested by the two kinds of comparisons. Overlaps exist between different tests and at most frequencies, where the conformity between the transfer functions calculated by the 10<sup>th</sup> and 20<sup>th</sup> orders of the same disc is generally higher than that between the transfer functions calculated by the two different discs. Therefore, the transfer functions calculated with the 20<sup>th</sup> order of one disc are representative for the vehicles.

Furthermore, in order to investigate the dependency of the transfer functions on the braking decelerations, correlation coefficients between them are calculated in the frequency domain. The Pearson product-moment correlation coefficient is used for this calculation. It is a measure of the linear correlation between two variables  $x$  and  $y$ , returning a value between -1 and +1, where -1 represents a total negative correlation, 0 no correlation, and +1 a total positive correlation<sup>162</sup>. For each frequency  $f$ , the correlation coefficient  $r_{aG(f)}$  between the braking decelerations and the transfer functions is calculated with

$$r_{aG(f)} = \frac{\sum_{i=1}^{50} (a_i - \bar{a})(G(f)_i - \overline{G(f)})}{\sqrt{\sum_{i=1}^{50} (a_i - \bar{a})^2} \sqrt{\sum_{i=1}^{50} (G(f)_i - \overline{G(f)})^2}} \quad (6.7)$$

for the entire 50 tests of each vehicle. Here  $\bar{a}$  and  $\overline{G(f)}$  are the means of the 50 decelerations and the 50 transfer functions for each frequency, respectively.

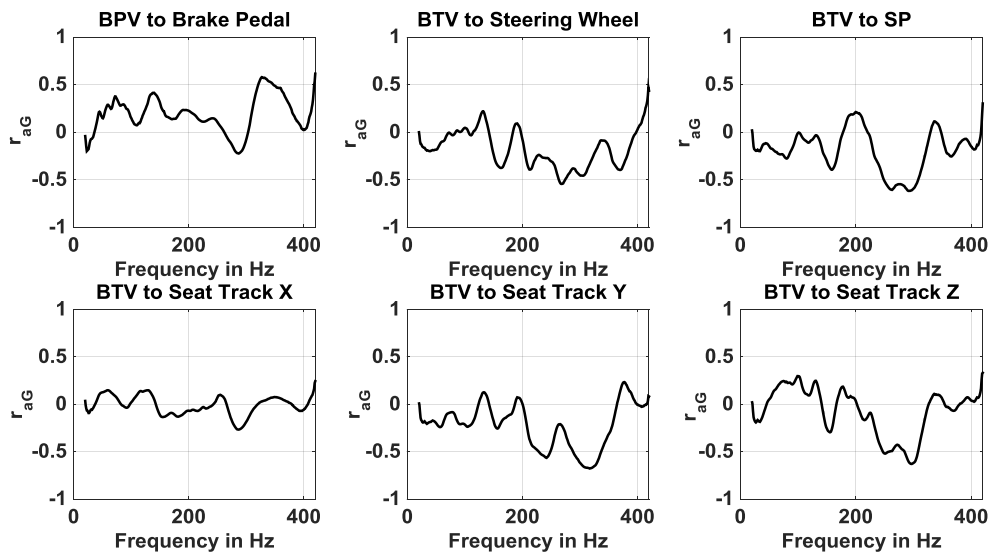


Figure 6-9: The correlation between the transfer functions and the braking decelerations in the frequency domain for vehicle  $B, \Delta d_D \approx 60 \mu\text{m}$

<sup>162</sup> Gibbons und Chakraborti: Nonparametric statistical inference, 2003, p.422.

Seeing the results of vehicle *B* in Figure 6-9 makes it clear that the correlation coefficients are mostly within  $\pm 0.5$ . This means that there is no defined dependency of the transfer functions on the deceleration. Therefore, a transfer function determined by only one measurement is not reliable; a number of tests with different decelerations are necessary to obtain a representative result.

## 6.2 Transfer mechanisms of drone noise

### 6.2.1 The assumed transfer paths of drone noise

Since the transfer paths of brake judder induced vibrations have been already well manifested by means of vehicle tests and simulations in the course of cold judder research, as seen in Figure 1-4. On the contrary, the transfer mechanisms of drone noise have been still not investigated.

According to the subjective judgments of the drivers and the passengers during the testing of the three vehicles, the drone noise transmitted into the vehicle interior can mainly be attributed to two mechanisms: direct noise emission from the disc/pads interfaces due to the variation of brake power, and this is the predominant cause for the vehicle interior drone noise; secondary radiation from the vibrations of certain vehicle interior accessories (especially the dashboard), which only plays a notable role when some remarkable resonance frequencies are excited. The drone noise that is directly radiated from the disc/pads interfaces is propagated through the car body into the vehicle interior. The dash board vibration is actually the result of the transmission of the vibrations caused by high-order judder from the wheel brake to the car body. Based on this subjective assumption, the transfer paths of drone noise are illustrated in Figure 6-10. In the following, the transfer mechanisms of the first path will be explored in detail, and the contribution of the dashboard vibration to the interior drone noise will be manifested by the coherence analysis between them. As a result, the assumed transfer paths will be confirmed.

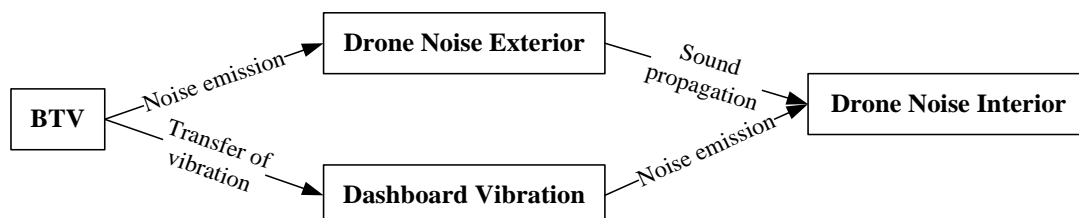


Figure 6-10: Transfer paths of the drone noise

## 6.2.2 Drone noise emission from the disc/pads interfaces

The ratio between the radiated sound power in the ambient air and the exciting mechanical power is defined as the acoustic efficiency<sup>163</sup>:

$$\zeta = \frac{P_{noise}}{P_{mech}} \quad (6.8)$$

Sound power is a theoretical value that is not directly measurable. A sound source produces sound power and this generates a sound pressure fluctuation in the air. Sound power is the distance independent cause, whereas sound pressure is the distance dependent effect. Sound intensity is the sound power per unit area. It can be calculated by<sup>163</sup>:

$$I = p \cdot v \quad (6.9)$$

where  $v$  is the particle velocity, which is the oscillating velocity of the particles around their rest positions. In the free field, where the sound pressure and the particle velocity are in phase, the specific acoustic impedance can be expressed as<sup>164</sup>:

$$Z_0 = \frac{p}{v} = \rho c \quad (6.10)$$

where  $\rho$  and  $c$  represent the density of a medium and speed of sound in the medium. It denotes the relationship between the particle velocity and the speed of sound in a medium. Therefore, the sound power in air can be calculated by:

$$P = I \cdot A = p \cdot v \cdot A = \frac{p^2 \cdot A}{\rho \cdot c} \quad (6.11)$$

Assuming that the propagation of the drone noise radiated from the disc/pads interfaces can be seen as spherical free field sound propagation with the spherical center located in the center of the brake caliper, sound power of the drone noise can be estimated by:

$$P_{noise} = \frac{p_{brake}^2 \cdot A}{\rho \cdot c} = \frac{4\pi \cdot d^2 \cdot p_{brake}^2}{\rho \cdot c} \quad (6.12)$$

where  $p_{brake}$  is the sound pressure acquired by the microphone located near the wheel brake (e.g. see the microphone in the upper right corner of Figure 4-12), and  $d$  is the distance between the microphone and the center of the brake caliper ( $d \approx 0.2$  m in the tests of vehicle *B*). Besides, for air,  $\rho = 1.2$  kg/m<sup>3</sup> and  $c = 343$  m/s are used in the following calculation.

The exciting mechanical power for the drone noise is the variation of the brake power in the case of high-order judder. It is equal to  $\Delta M_B$  multiplied by the rotational speed  $n$ :

<sup>163</sup> Zeller et al.: Handbuch Fahrzeugakustik, 2012, p.116.

<sup>164</sup> Zeller et al.: Handbuch Fahrzeugakustik, 2012, p.120.

$$P_{mech} = \Delta M_B \cdot n \quad (6.13)$$

Therefore, taking the 20<sup>th</sup> order for example, the acoustic efficiency of drone noise radiation can be calculated in the frequency domain. As a result, the sample mean and the confidence bounds of 95% confidence interval computed by the 50 tests of vehicle *B* with the 60  $\mu\text{m}$  DTV disc are shown in Figure 6-11. A narrow confidence interval is obtained at all frequencies, which also manifests that sound power of the drone noise is ascribable to the brake power variation. The acoustic efficiency of the front brake of vehicle *B* is approximately  $0.4 \times 10^{-4}$ , especially seeing from the range of 100 to 350 Hz.

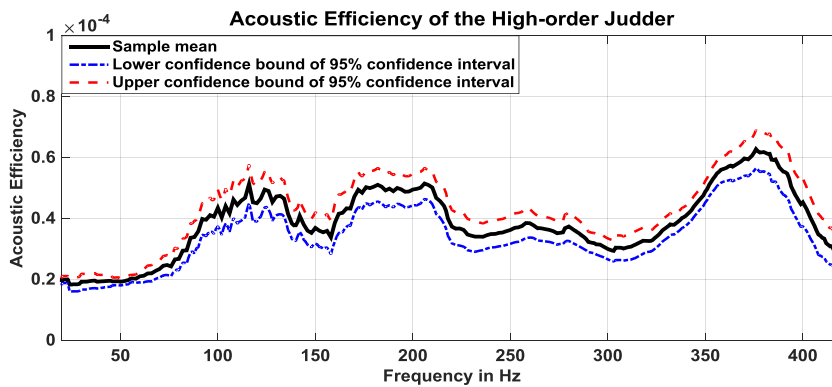


Figure 6-11: Acoustic efficiency of the high-order judder,  $\Delta d_d \approx 60 \mu\text{m}$ , vehicle *B*

Further, in order to study the reproducibility of the acoustic efficiency identified by the 60  $\mu\text{m}$  DTV of vehicle *B* and to compare the acoustic efficiencies among different discs, the sample means calculated by the 60  $\mu\text{m}$  DTV and 100  $\mu\text{m}$  LRO discs of vehicle *B*, and the 60  $\mu\text{m}$  DTV disc in the front left brake of vehicle *C* are shown in Figure 6-12.

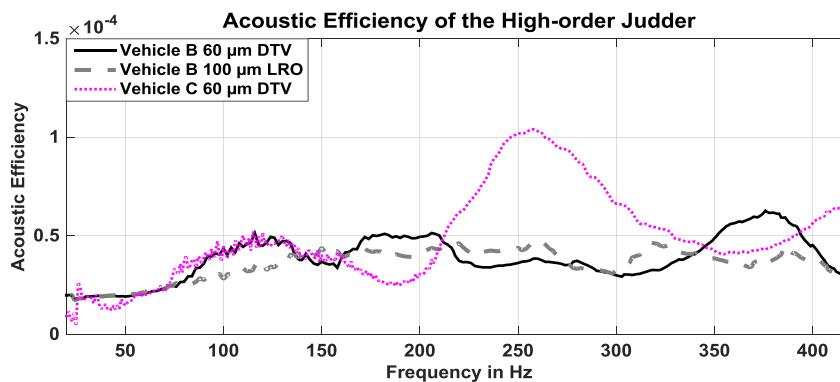


Figure 6-12: Acoustic efficiencies of the front brakes of vehicle *B* and *C*

The acoustic efficiency calculated by the 60  $\mu\text{m}$  DTV disc is generally reproducible by the 100  $\mu\text{m}$  LRO disc in vehicle *B*. The discrepancies at some frequencies should be resulted from the order line extraction process. Because the 20<sup>th</sup> order of the drone noise is not evidently stronger than the other noises in SPL spectral diagram (see one example

in Figure C-6), the extracted amplitudes of the 20<sup>th</sup> order line might be greater than the actual ones. Besides, the acoustic efficiency of the front brake of vehicle *B* is roughly on the same level with that of the front brake of vehicle *C*, except for the range from about 220 to 320 Hz, where there is a prominent peak in the acoustic efficiency of vehicle *C*.

### 6.2.3 Drone noise propagation from vehicle exterior to interior

The drone noise that is generated by the interactions between the brake disc and its pads is generally transmitted into the vehicle by three mechanisms<sup>165</sup>:

- Transmission directly through the solid car body;
- Transmission through the leakages, that is to say, transmission through the small leaks in the car body (Such leakages exist particularly in the areas surrounding the steering column, the pedals, the cable ducts and et al.<sup>166</sup>);
- Flanking transmission that is firstly exciting the structure-borne noise and then radiating as secondary airborne noise.

Due to the complexity of the car body structure, it is impossible to differentiate and thus separately calculate the amounts of the three transfer mechanisms in the drone noise transfer process without specialized testing and simulation. In addition, the drone noise transmitted into the vehicle is also strongly influenced by the reflections and the absorptions of the vehicle interior surfaces. Therefore, in order to study the drone noise transfer behaviors from the vehicle exterior (near the wheel brake) to the vehicle interior (near the driver's ear), the Level Difference is adopted:

$$\Delta L_p = L_{p,exterior} - L_{p,interior}^{167} \quad (6.14)$$

It represents the insulation effect of the car body against drone noise. The statistical analysis of the Level Difference in vehicle *B* calculated by the 50 tests with the 60  $\mu\text{m}$  DTV disc is shown in Figure 6-4. The 95% confidence interval is a narrow band as well, which reflects a good reproducibility of the 50 tests. The complicated frequency dependency and non-linear properties of drone noise transmission are indicated by Level Difference curves. However, on the whole, the Level Difference increases with rising frequency and the tendency can be fitted by the linear fit:

$$\Delta L_p = 0.094f/\text{Hz} - 1.5 \quad (6.15)$$

It means that the Level Difference raises approximately 10 dB with every 100 Hz increase of the drone noise frequency.

---

<sup>165</sup> cf. Zeller et al.: Handbuch Fahrzeugakustik, 2012, p.123.

<sup>166</sup> Zeller et al.: Handbuch Fahrzeugakustik, 2012, p.133.

<sup>167</sup> cf. Zeller et al.: Handbuch Fahrzeugakustik, 2012, p.125–126.



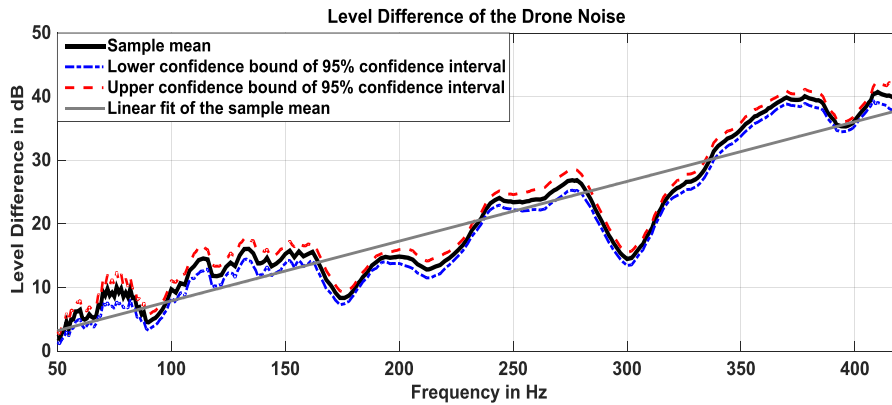


Figure 6-13: Level difference of the vehicle exterior and interior drone noises of vehicle *B*,  $\Delta d_p \approx 60 \mu\text{m}$

Sample means of the Level Difference in vehicle *B* calculated by two discs, and in vehicle *C* obtained by the  $60 \mu\text{m}$  DTV disc of the front brake are shown in Figure 6-14. The Level difference in vehicle *B* computed by the  $60 \mu\text{m}$  DTV disc is roughly reproduced by the  $100 \mu\text{m}$  LRO disc, considering the possible errors in the extracted 20<sup>th</sup> order lines of the exterior drone noises. Generally the insulation capability of vehicle *C* is on the same level with that of vehicle *B*. Besides, the Level Difference in vehicle *C* also exhibits the similar frequency dependency as in vehicle *B*.

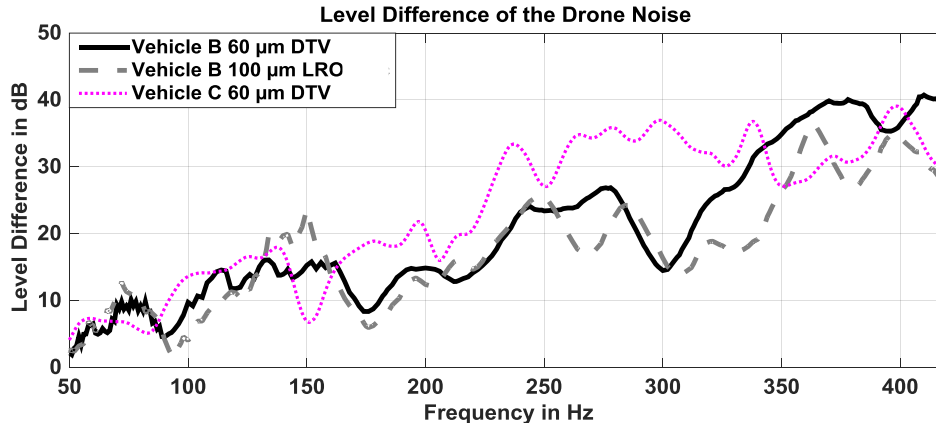


Figure 6-14: The Level Differences in vehicle *B* and *C*

#### 6.2.4 Coherence between interior drone noise and dashboard vibration

During the tests with the three vehicles, it was subjectively determined that some vehicle interior components, especially the dashboard, were also making some noises when extraordinary resonances were excited. In order to study the relationship between the dashboard vibration and the vehicle interior drone noise, the dashboard vibration of vehicle *B* was measured by a 1-axis accelerometer (Kistler, 8610B100). The position of the accelerometer is displayed Figure 6-15.



Figure 6-15: Measurement of the dashboard vibration in vehicle *B*

Taking one test of vehicle *B* with the 100  $\mu\text{m}$  LRO disc for example, spectral analyses of BTV, dashboard vibration, vehicle exterior noise, and vehicle interior noise are shown in Figure 6-16. The test maneuver is decelerating with 0.24  $g$  from 160 km/h. Peaks at around 190 Hz can be found from the 10<sup>th</sup>, 20<sup>th</sup>, and higher harmonic orders of the dashboard vibration and the vehicle interior drone noise, while they can hardly be detected in the spectral diagrams of BTV and the vehicle exterior noise. This phenomenon can be better seen from the extracted 10<sup>th</sup>, 20<sup>th</sup>, 30<sup>th</sup> and 40<sup>th</sup> order lines in Figure 6-17. In order to compare with the SPL curves that are expressed in dB, BTV and the dashboard vibration are also displayed in dB with references of 1 Nm and 1  $\text{m/s}^2$  respectively. Consequently, the peaks of the vehicle interior drone noise should be caused by the resonance of the dashboard.

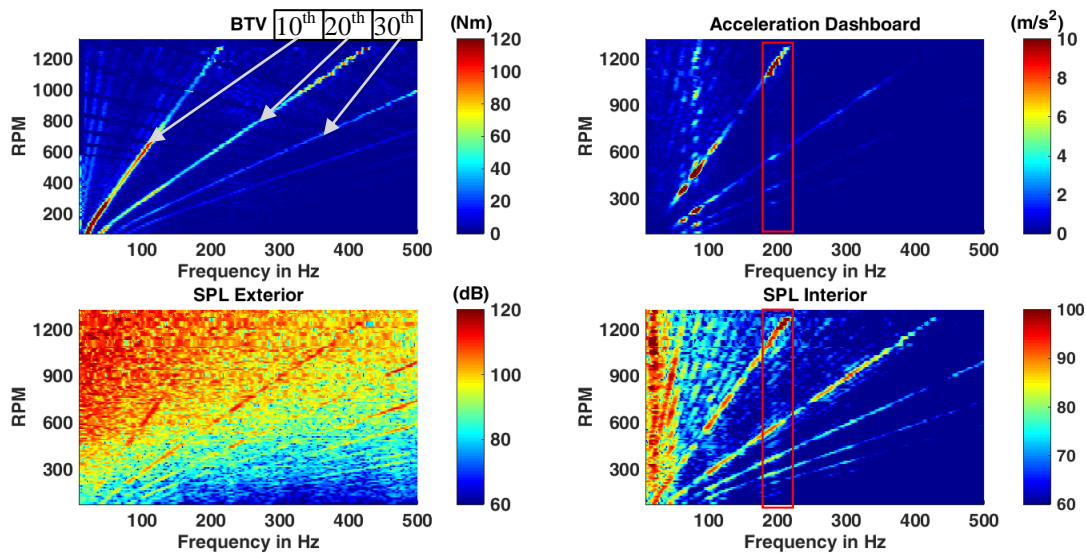


Figure 6-16: Spectral analyses of BTV, dashboard vibration, vehicle exterior and interior noises vehicle *B*,  $\Delta z_D \approx 100 \mu\text{m}$

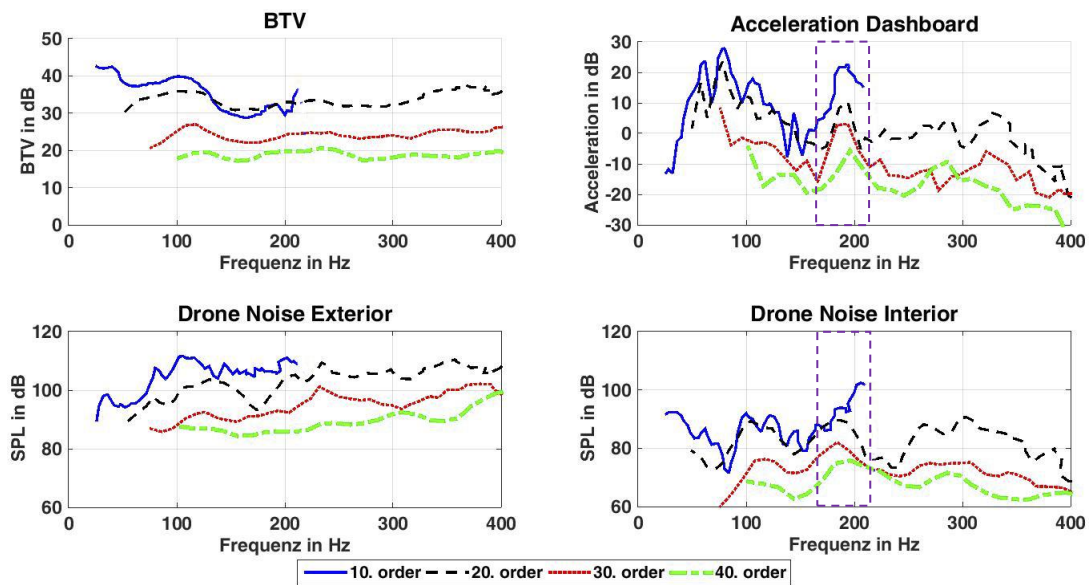


Figure 6-17: Order lines of BTV, dashboard vibration, vehicle exterior and interior drone noises vehicle  $B$ ,  $\Delta z_D \approx 100 \mu\text{m}$

Coherence analyses between the vehicle exterior noise and the vehicle interior noise, as well as between the dashboard vibration and the vehicle interior noise are respectively performed, in order to confirm the relationship. From the results in Figure 6-18, it is evident that the coherences between the 10<sup>th</sup>, 20<sup>th</sup>, and higher harmonic orders of the dashboard vibration and those of the vehicle interior drone noise are greatly strengthened around 190 Hz. Consequently, the contribution of the dashboard resonance to the vehicle interior drone noise is proved.

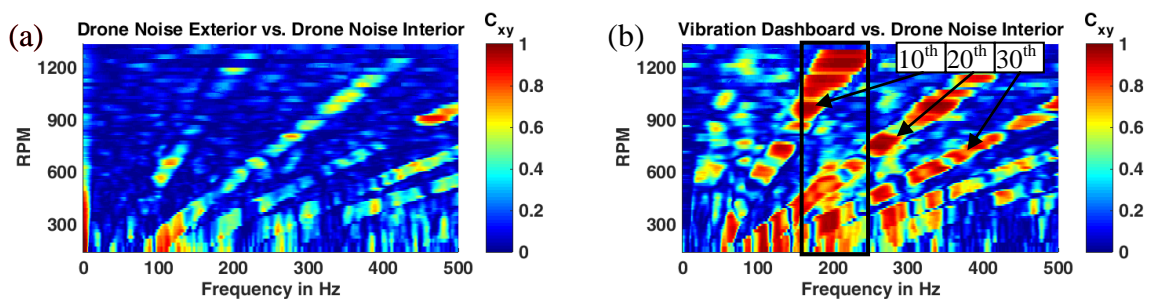


Figure 6-18: Coherence analyses of the sample test, vehicle  $B$ ,  $\Delta z_D \approx 100 \mu\text{m}$

## 6.3 Discussion

It is raised by Haverkamp et al. that the principle strategy of brake noises assessment can be classified into three categories<sup>168,169</sup>:

<sup>168</sup> Haverkamp: Brake Noise Assessment, 2005, p.2–3.

- a) Driver focused: optimizing brake noise as part of all perceivable attributes of the driving environment.
- b) Pedestrian focused: affecting the exterior appearance of a vehicle by exterior brake noise radiation.
- c) Component related: focusing on the noise source and helpful for the definition of component targets. Influences on the passengers cannot be predicted considering the complicated transfer behaviors. Correlation of component measurement results to customers' rating is limited.

Considering the occurring condition of high-order hot judder that is decelerating from high velocities, the pedestrian focused strategy is meaningless for the assessment of the drone noise. Besides, the driver focused and component related strategies are also the traditional strategies for assessing the vibrations caused by brake judder. The effects of the high-order judder on the driver's subjective perception depends on the judder intensity in wheel brakes (expressed by BTV and BPV) and the transfer behaviors, that is the vibration properties of the braking system, the steering system, the suspension system, some vehicle interior components, and the sound proofing property of the car body as well as the sound property of the passenger compartment. The global transfer functions computed in this chapter have established the links between the judder excitations and the driver, making it possible to predict the driver's perception to a given high-order judder excitation and vice versa to find out the BTV/BPV thresholds for perceiving the high-order judder.

In addition, from the global transfer functions and the transfer mechanisms of drone noise, it can be concluded that minimizing the overall sensitivity of the transfer paths, and especially diminishing the resonances of the transfer paths and the vehicle components that can be easily excited by brake judder, are the fundamental measures to reduce the transfer of high-order judder.

---

<sup>169</sup> Mauer and Haverkamp: Measurement and assessment of noise, p.4–5.

---

## 7 Perception of high-order judder

Based on the relationships between BPV/BTV and the driver interface quantities (the transfer functions), threshold values for perceiving the high-order judder are explored in this chapter. The critical values for perceiving the vehicle interior drone noise are selected by literature research on the vehicle interior noise level and the auditory masking characteristics, and the driver interface vibrations are determined by regression analysis between the objectively measured vibrations and the corresponding subjective ratings. According to the identified SPL and vibration values and the transfer functions, the threshold values of BPV/BTV are obtained and classified into different groups according to the occurring frequencies.

### 7.1 Determination of the critical SPL

#### 7.1.1 Vehicle interior noise level

In order to describe the noise emission of a vehicle, main sound sources are normally categorized into three groups: propulsion noise, tire/road noise (rolling noise) and wind noise<sup>170,171</sup>. The noises from these three groups of sound source are either directly transmitted into the vehicle interior as airborne noises (AN), or firstly transmitted as structure-borne noise (SN) through the chassis to the car body and then radiated as secondary noise from the car body, as shown in Figure 7-1.

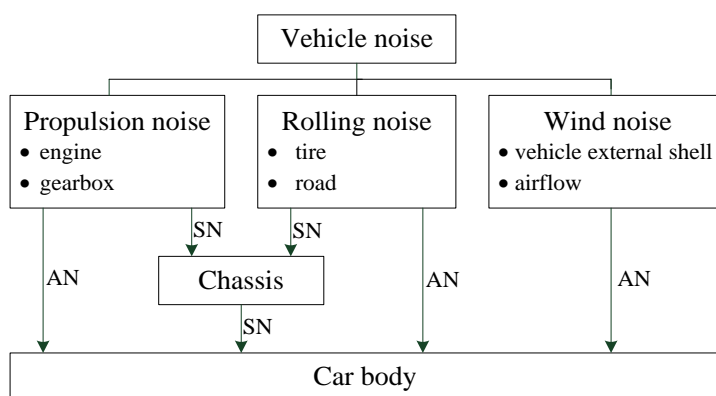


Figure 7-1: The main components of vehicle noises and their basic transfer mechanisms<sup>171</sup>

---

<sup>170</sup> Müller: Handbook of engineering acoustics, 2013, p.368.

<sup>171</sup> Zeller et al.: Handbuch Fahrzeugakustik, 2012, p.201.

Propulsion noises are caused by the engine, the transmission, the auxiliaries as well as the intake/exhaust cycle changes. The engine noise is chiefly dependent on the engine load and the engine rotational speed, as illustrated in Figure 7-2. In a comfort-oriented vehicle, the engine noise is generally lower than the rolling and wind noises, and is therefore hardly audible during constant-speed drives with the direct gear (e.g. the 5<sup>th</sup> gear). With increasing engine load, especially for the drives with lower gears in the lower velocity range, the engine noise is much higher than the rolling and wind noises, and thus it determines the vehicle overall noise level. However, at very high velocities (> 180 km/h), the rolling and wind noises can still exceed the full-load engine noise.<sup>172</sup>

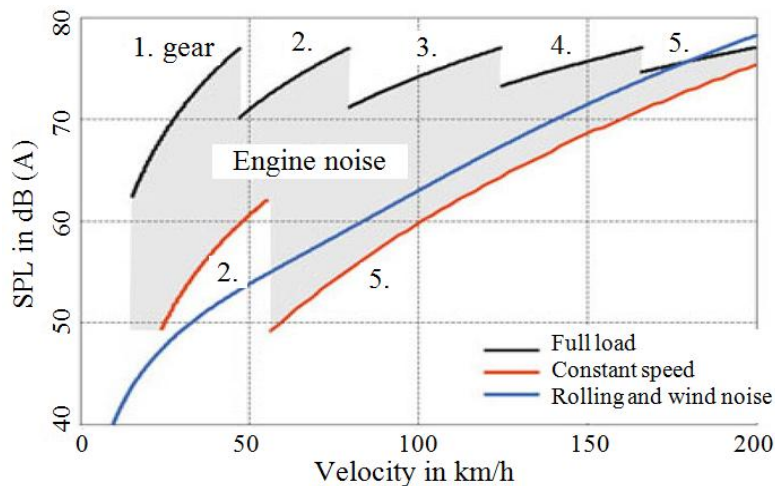


Figure 7-2: Engine noise in vehicle interior, in comparison with rolling noise and wind noise<sup>172</sup>

Rolling noise is caused by the interactions between the tire running surface and road. It increases with rising driving velocity. The sound intensity increases approximately with the 2<sup>nd</sup> power of the driving speed. It is the dominant noise during constant-speed drives in the moderate velocity range (ca. from 50 to 100 km/h). Wind noise occurs due to the interferences of the wind on the edges and splits of the vehicle surfaces. It also increases with rising driving velocity, and the sound intensity increases approximately with the 6<sup>th</sup> power of the driving speed. Therefore, the wind noise usually dominates the total noise level of a passenger car at higher speeds (> 100 km/h)<sup>172,173</sup>. Rolling noise and wind noise in dependence on the driving speed for a typical middle-class vehicle is displayed in Figure 7-3, in which both the measured and the approximated results are exhibited.

In a vehicle, these vehicle noises can be perceived in the frequency range from ca. 30 Hz to over 10 kHz. Propulsion noise can be heard as, for example, from the low-frequency idle running noise and humming noise to the high-frequency noises of the fuel gas system. Rolling noise can be presented as low-frequency boom or hum and

<sup>172</sup> Zeller et al.: Handbuch Fahrzeugakustik, 2012, p.202.

<sup>173</sup> Müller: Handbook of engineering acoustics, 2013, p.368-369.

high-frequency tire singing or wet sizzle. Wind noise is possibly to be perceived as low-frequency grumbling and high-frequency howling, squealing or whistling.<sup>174</sup>

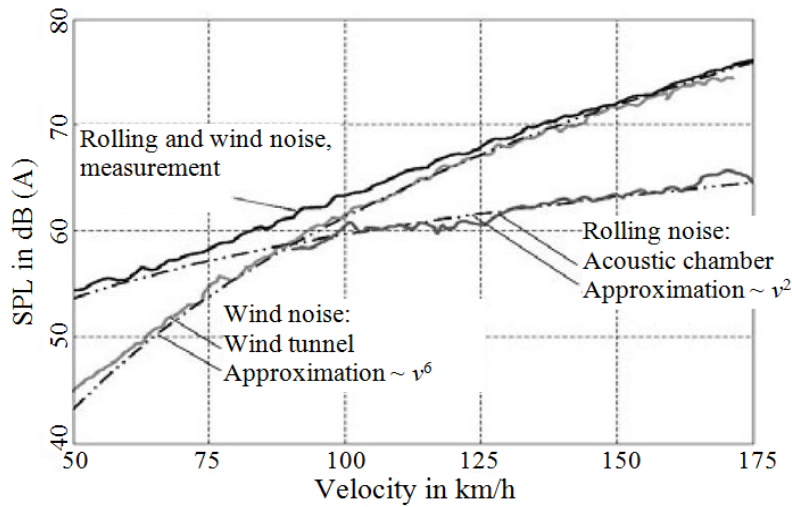


Figure 7-3: Rolling and wind noise in the interior of a middle class vehicle<sup>172</sup>

Due to the competitive pressure and the requirements of legislations, the total vehicle noise level has been greatly reduced in the last decades, and averagely 1.5 to 2 dB(A) have been diminished in the succeeding generations of the vehicles. The average noise level for the modern passenger cars is about 60 dB(A) during constant-speed drives with 100 km/h.<sup>175</sup> Seeing from Figure 7-2, the vehicle interior noise is approximately between 50 and 80 dB(A), increasing with the rotational speed and the engine load. This range can also be confirmed by the tests of vehicle *B* and vehicle *C* that were carried out during the investigation of the high-order judder transfer behaviors. For example, Figure 7-4 and Figure 7-5 shows the A-weighted noise levels inside vehicle *B* and vehicle *C* during the entire testing process. They are measured by the microphone near the driver's ear. Vehicle *B* is generally quieter than vehicle *C*. In the speedup phase from 50 to 180 km/h, the vehicle noise level is approximately from 50 to 70 dB(A) in vehicle *B* and 60 to 80 dB(A) in vehicle *C*. Besides, some orders of the engine noise and the high-order judder (caused by disc/pads contacts in the off-brake status) are particularly strong in the speedup phase of vehicle *C*.

<sup>174</sup> Genuit: Sound-Engineering im Automobilbereich, 2010, p.90-91.

<sup>175</sup> Zeller et al.: Handbuch Fahrzeugakustik, 2012, p.3.

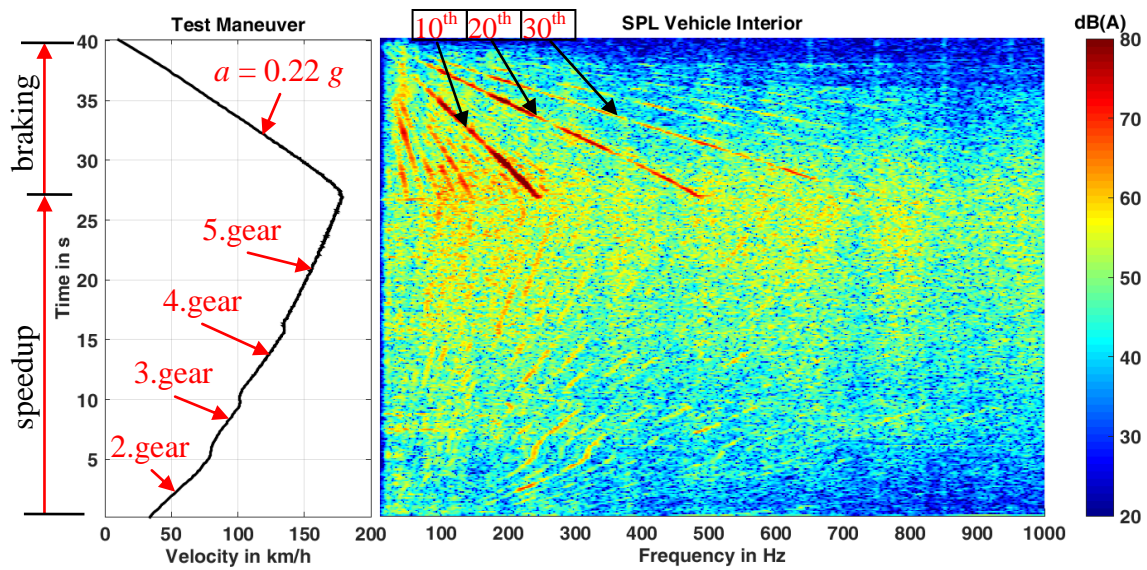


Figure 7-4: A-weighted noise level in vehicle *B* during one test,  $\Delta d_b \approx 60 \mu\text{m}$

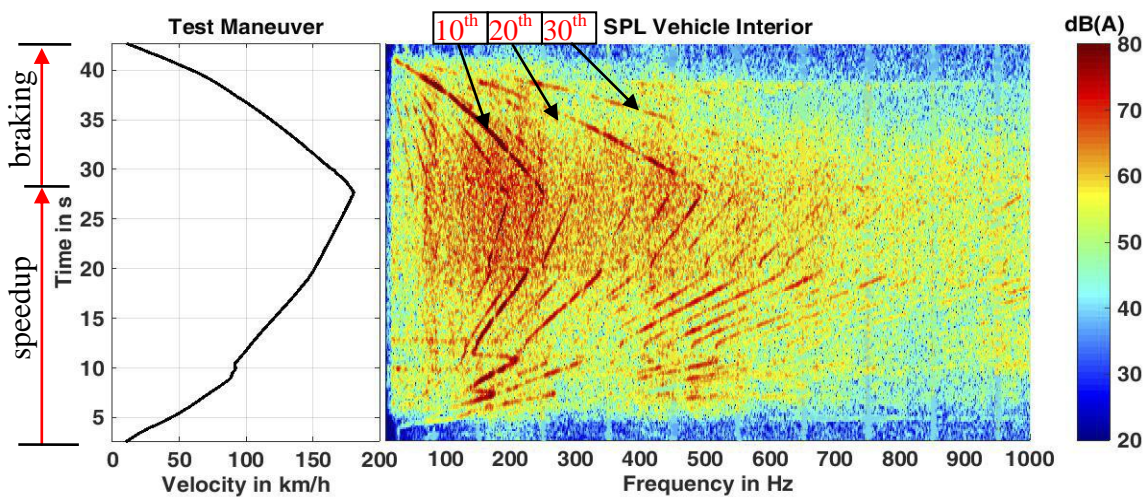


Figure 7-5: A-weighted noise level in vehicle *C* during a test,  $\Delta d_b \approx 60 \mu\text{m}$

### 7.1.2 Auditory masking and selection of the critical SPL

Auditory masking is the process by which the threshold of audibility for one sound is raised by the presence of another sound<sup>176</sup>, or how the sensitivity of one sound (called signal, or also often referred to as the test signal, probe signal, or maskee) is affected by the presence of another sound (called masker)<sup>177</sup>. The increase in the threshold or the threshold shift for one sound in the presence of another is called masking<sup>177</sup>.

<sup>176</sup> Rossing: Handbook of acoustics, 2014, p.477.

<sup>177</sup> Gelfand: Hearing, 2010, p.187–188.



The masking generated by a particular sound is strongly dependent on its intensity and spectrum. Regarding the masking produced by the pure tones, a series of masking patterns (or sometimes called masking audiograms) are shown in Figure 7-6. Each curve shows the amount of masking as a function of signal frequency produced by a masker with a given frequency and a given intensity.

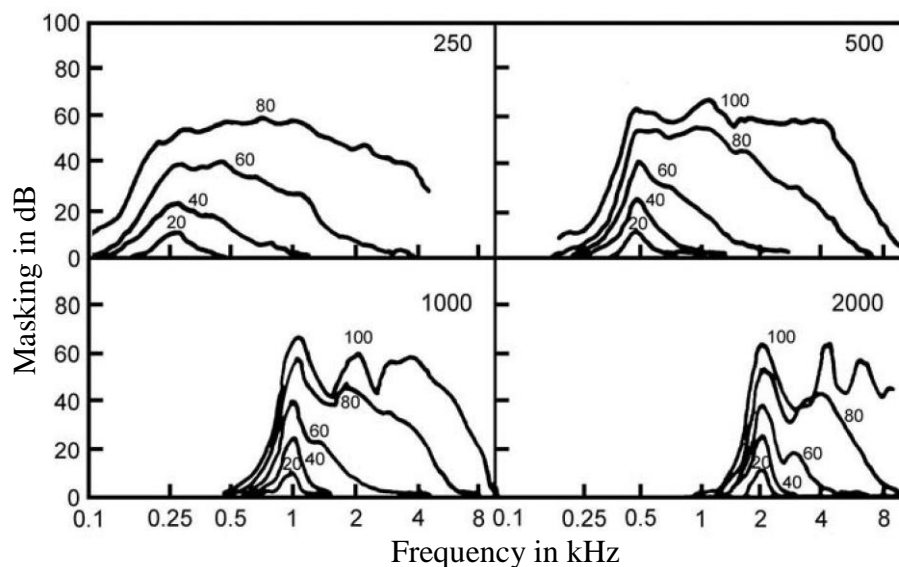


Figure 7-6: Masking patterns produced by some pure tone maskers. (Masker frequencies are indicated in each frame and the masker levels are indicated by the numbers on the curves)<sup>177</sup>

Following facts are reflected by the curves of the masking patterns<sup>177</sup>:

- The strongest masking happens in the immediate vicinity of the masker frequency and the amount of masking tapers with distance from this “center” frequency.
- Masking increases with rising intensity of the masker.
- The masking is roughly symmetric around the masker frequency for relatively low masker levels (20 and 40 dB). However, the masking patterns become asymmetrically wider with increasing masker intensity. There is evident spread of the masking effect upward in frequency but only a minimal effect downward in frequency. This phenomenon is normally called upward spread of masking.
- The masking patterns are wider for low-frequency maskers and are much narrower for high-frequency maskers, especially when the frequency axis is in logarithmic scale. In other words, high-frequency maskers are only effective over a relatively narrow frequency range near the masker frequency, but low-frequency maskers tend to be effective over a wider range of frequencies.

In order to demonstrate the pure tones masked by broadband noises, absolute threshold levels of the test tone at different frequencies in the presence of white noises is shown in Figure 7-7. The white noises are with different density levels from -10 to 50 dB in a step of 10 dB.

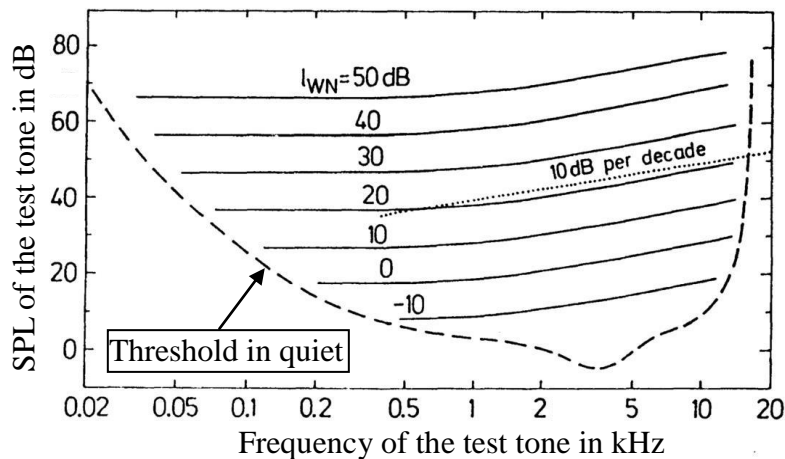


Figure 7-7: Masking contours of white noise markers with given density level  $l_{WN}$ , as a function of the test-tone frequency<sup>178</sup>

Several features can be summarized as following from the masking contours<sup>178</sup>:

- At low frequencies below 500 Hz, the threshold for perception of a tone is 17 dB above the density level of the masking noise. Those values are valid if the pure tone shows a level above 20 dB<sup>179</sup>.
- Over ca. 500 Hz, the masked thresholds rise with increasing frequency. The slope of this increase is about 10 dB per decade, illustrated by the dotted line.
- If the density level of the white noise masker is raised by 10 dB, the masked threshold of the pure tone is also shifted upwards by the same 10 dB. This indicates the linear behavior of masking produced by broad-band noises.
- At very low and very high frequencies, masked thresholds are the same as the threshold in quiet. The masking effects at these frequencies are not evident.

On the contrary to the masking by white noises, the threshold for perceiving a tone is generally below the density level of the pure-tone maskers, seeing from the masking patterns (Figure 7-6) in combination with the hearing threshold in quiet (Figure 2-21 and Figure 7-7). That is to say, the masking capacity of white noise is much higher than that of the pure tone. Vehicle noise is far away from a white noise with equal frequency distribution and a pure tone with a specific frequency. Therefore, smaller values (< 17 dB) have to be considered to define the minimum perceivable drone noise level above background noise<sup>179</sup>.

Besides, regarding the subjective perception of noise, the range from 50 to 70 dB(A) is evaluated as “fairly loud”, and the range from 70 to 90 dB(A) is evaluated as “loud” (see Table 2-4). Based on the overall consideration of the masking characteristics, the

<sup>178</sup> Fastl und Zwicker: Psychoacoustics: Facts and Models, 2007, p.62–63.

<sup>179</sup> Haverkamp: Brake Noise Assessment, 2005, p.3–4.

typical vehicle interior noise level (50-80 dB(A)), as well as the human's subjective perception of noise, as criteria for the drone noise evaluation, 60 dB (A) is chosen as the critical value at which drone noise starts to be hearable over other vehicle noises, or in other words, at which drone noise starts to be contributive to the total vehicle noise level that should be reduced; and 80 dB(A) is chosen as the critical value at which drone noise is dominant over the total vehicle noise level and therefore has to be mitigated.

## 7.2 Determination of the critical vibrations

### 7.2.1 Subjective rating and objective assessment

Seeing from the results of the subjective ratings done by the six test persons, it turns out to be that the vibration peaks received significantly lower scores than the overall vibration level. Besides, the ratings for the same configuration do not change much despite the variation of braking decelerations and the change of test persons, while there are obvious differences among varied configurations. Therefore, for each configuration only one test with 0.2  $g$  deceleration is picked out for the following regression analysis. Given eight different discs and two subjective scores for each disc, altogether eight tests with 16 scores are available for each driver interface vibration (the brake pedal pulsation, the steering wheel oscillation, and seat track vibrations). These values stand for the average scores for each test configuration.

Further, the measured vibrations are weighted with corresponding frequency weighting filters in order to perform the regression analysis between the vibrations and the subjective ratings. In correspondence with the subjective ratings for the overall vibration level and the transient peaks, the RMS value of the whole braking time and the MTVV are calculated for the eight tests. The time constant  $\tau$  is set to 1 s in the calculation of MTVV. Taking "comfort" as the criterion for a seated person in the car, the frequency weighting filter  $W_d$  is used for the assessment of the longitudinal and transverse seat track vibrations;  $W_k$  is applied for the assessment of the vertical seat track vibration and the brake pedal pulsation;  $W_{hi}$  is employed for assessing the steering wheel oscillation. Together with the A-weighting curve  $W_A$  for drone noise assessment, the adopted frequency weighting curves for the vibrations are shown in Figure 7-8. It is clear that in the frequency range of hot judder (10 to 600 Hz) the vibration weighting curves are unequivocally descending, whereas the A-weighting curve is ascending. In other words, in the frequency range of hot judder, the human sensitivity to the vibrations is dropping, while the sensitivity to drone noise is rising with increasing frequency. Moreover, human beings are generally much more sensitive to the vertical and the hand-arm vibrations than the horizontal vibrations in this frequency range, and the sensitivity to the hand-arm vibrations (the steering wheel oscillation) is evidently higher than that to the

whole-body vibrations (seat track vibrations and brake pedal pulsation) in the range higher than 100 Hz.

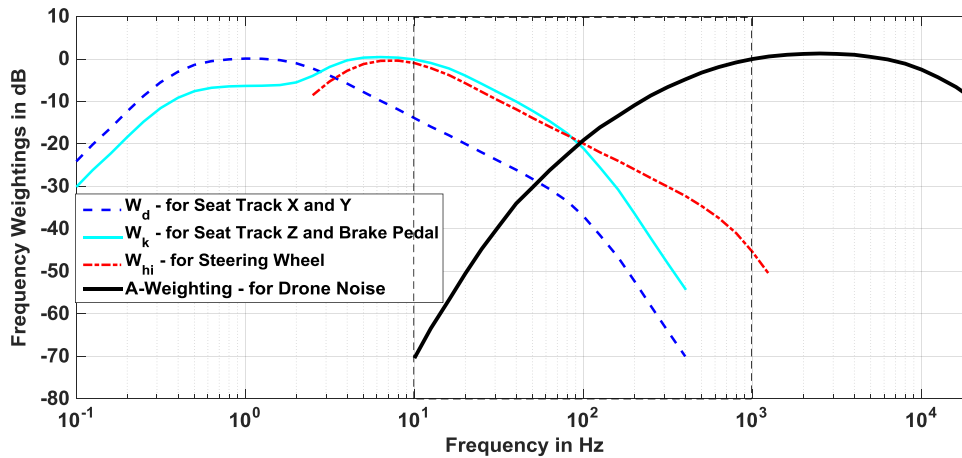


Figure 7-8: The applied frequency weighting filters for the high-order judder<sup>180,181,182</sup>

During the frequency weighting process, a 2<sup>nd</sup> order high-pass Butterworth filter with a 10 Hz cutoff frequency is applied to the time signals of all the vibrations in order to eliminate the static part induced by sensor drift, the influence of low-frequency road excitations, the low-frequency judder, and the influence of the imbalanced tire. Because the subjective rating for car body vibration is the integrated effect of the vibrations in three directions, the vibration total value of the frequency weighted accelerations is accordingly calculated by<sup>183</sup>:

$$a_{total} = \sqrt{k_X^2 a_{wX}^2 + k_Y^2 a_{wY}^2 + k_Z^2 a_{wZ}^2} \quad (7.1)$$

where  $a_{wX}^2$ ,  $a_{wY}^2$ ,  $a_{wZ}^2$  are the RMS values of the frequency-weighted acceleration for the seat track vibrations in X, Y, and Z directions, and  $k_X, k_Y, k_Z$  are multiplying factors, which are all equal to 1 for the comfort evaluation of a seated person.

## 7.2.2 Regression analysis

The correlation between the subjectively rated scores and the objectively assessed vibrations is calculated by polynomial regression, considering that the correlation may be not simple linear. Polynomial regression is actually a form of linear regression, in which the

<sup>180</sup> cf. VDI 2057 Part 1, 2002-09, p.17.

<sup>181</sup> cf. VDI 2057 Part 2, 2014-05, p.9.

<sup>182</sup> cf. DIN EN 61672-1, 2014-07, p.21.

<sup>183</sup> ISO 2631-1, 01.05.1997, p.12.

relationship between the independent variables  $x$  and  $y$  is modeled as an  $m^{\text{th}}$  degree polynomial. The polynomial regression model with one variable is expressed by<sup>184</sup>:

$$y = \beta_0 + \beta_1 x + \beta_2 x^2 + \beta_3 x^3 + \dots + \beta_m x^m + \varepsilon \quad (7.2)$$

In the equation,  $\varepsilon$  represents the random error. In fact, these models are all linear from the estimation point of view, since the regression function is linear in terms of the unknown parameters  $\beta_0, \beta_1, \beta_2, \dots$ . Treating  $x, x^2, x^3, \dots$  as being distinct independent variables, polynomial regression is also considered to be a special case of multiple linear regression. The regression models for the seat track vibrations, the brake pedal pulsation, and the steering wheel oscillation are tested by “ $F$ -test” and they all stratify the significance level of 1%.

Coefficient of determination  $R^2$  is applied to find the adequate degrees for the polynomial regression models by comparing the goodness of fit. It is a number that indicates how well data fit a statistical model and falls between 0 and 1. The higher the value of  $R^2$ , the better the model is at predicting the data. It is determined by<sup>184</sup>:

$$R^2 = 1 - \frac{\sum_{i=1}^{Ns} (y_i - \hat{y})^2}{\sum_{i=1}^{Ns} (y_i - \bar{y})^2} \quad (7.3)$$

where  $\hat{y}$  represents the calculated values of  $y$ ,  $\bar{y}$  is the mean of  $y$ , and  $Ns$  is the sample size. It is clear that  $R^2$  is increasing with higher degree of the regression model, because with higher degree more variables are added to model which makes a better fitting possible. The use of an adjusted coefficient of determination  $\bar{R}^2$  takes this phenomenon into account by involving the number of explanatory variables ( $x, x^2, \dots$ )  $k$  and it is defined as<sup>184</sup>:

$$\bar{R}^2 = 1 - (1 - R^2) \frac{Ns - 1}{Ns - k - 1} \quad (7.4)$$

In order to avoid a complicated regression model,  $\bar{R}^2$  is calculated only for the 1<sup>st</sup> to 3<sup>rd</sup> degrees of the polynomial regression model defined in Equation 7.2, and the results are listed in Table 7-1.

---

<sup>184</sup> Ostertagová: Modelling using Polynomial Regression, 2012, p.501–503.

Table 7-1: Adjusted coefficient of determination of the polynomial regression model

Evaluating variable	Adjusted coefficient of determination $\bar{R}^2$		
	1 <sup>st</sup> degree	2 <sup>nd</sup> degree	3 <sup>rd</sup> degree
Seat track vibrations	0.9729	0.9865	0.9904
Brake pedal pulsation	0.9348	0.9928	0.9923
Steering wheel oscillation	0.9661	0.9809	0.9831

Considering the three evaluating variables together, the 2<sup>nd</sup> is generally much more accurate than the 1<sup>st</sup> degree, while there is only a minor improvement when calculating with the 3<sup>rd</sup> degree. Therefore, the 2<sup>nd</sup> degree is chosen, with which  $\bar{R}^2$  is higher than 0.98 for the three evaluating variables. Consequently, regression analyses between the subjective scores and the objective assessments of the car body vibrations, the brake pedal pulsation, and the steering wheel oscillation have been conducted by using the 2<sup>nd</sup> degree evaluation model. From the results in Figure 7-9, it is clear that the test persons were most sensitive to the whole car body vibration, and least sensitive to the steering wheel oscillation.

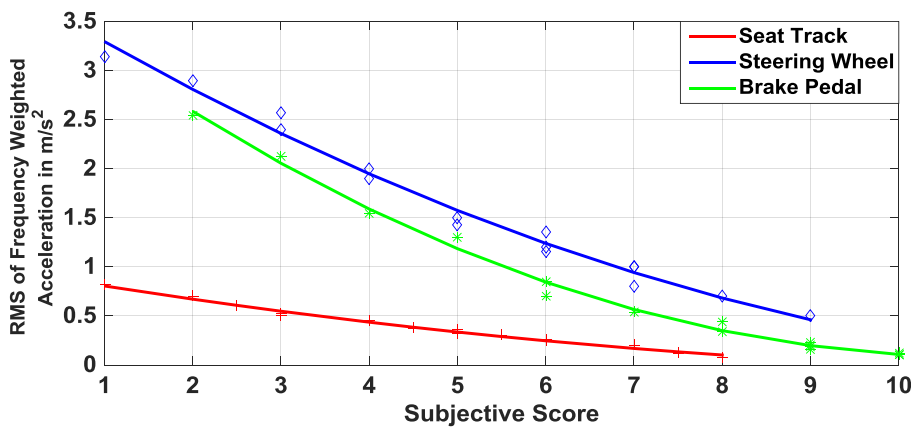


Figure 7-9: Regression analyses between the subjective ratings and the RMS values of the frequency-weighted vibrations caused by high-order judder

### 7.2.3 Threshold values of BPV and BTV

The subjective score of “8” in the subjective evaluation system (Table 4-7) is used as the evaluation criterion, with which the high-order judder is just starting to be perceived. It represents the perception threshold of high-order judder. Consequently, the threshold values (the RMS values of the frequency-weighted accelerations) for the vibrations of the seat track, the brake pedal, and steering wheel can be obtained from the regression models in Figure 7-9, and they are listed in Table 7-2.

Table 7-2: Perception threshold values of the driver interface vibrations

Driver interface vibration	Threshold value
Seat track vibration X, Y, Z	$a_{wt_e,ST,thres} = 0.10 \text{ m/s}^2$
Brake pedal pulsation	$a_{wt_e,pedal,thres} = 0.35 \text{ m/s}^2$
Steering wheel oscillation	$a_{wt_e,SW,thres} = 0.70 \text{ m/s}^2$

Based on the threshold RMS values of the frequency-weighted accelerations, the critical values of drone noise ( $L_{p,interior,critical} = 60, 80 \text{ dB(A)}$ ), the transfer functions in Figure 6-6 and the frequency weighting filters, the threshold values of BPV and BTV for perceiving the vibrations and the drone noise can be calculated in the frequency domain:

- The threshold values of BPV for perceiving the brake pedal pulsation:

$$\Delta p_{B,pedal,thres}(f) = \left| \frac{a_{pedal,thres}(f)}{G_{BS}(f)} \right| = \left| \frac{\sqrt{2}a_{wt_e,pedal,thres}/W_k(f)}{G_{BS}(f)} \right| \quad (7.5)$$

- The threshold values of BTV for perceiving the steering wheel oscillation:

$$\Delta M_{B,SW,thres}(f) = \left| \frac{a_{SW,thres}(f)}{G_{StS}(f)} \right| = \left| \frac{\sqrt{2}a_{wt_e,SW,thres}/W_{hi}(f)}{G_{StS}(f)} \right| \quad (7.6)$$

- The threshold values of BTV for perceiving the vehicle interior drone noise:

$$\Delta M_{B,noise,thres}(f) = \left| \frac{p_{interior,critical}}{G_{noise}(f)} \right| = \left| \frac{10^{\frac{\sqrt{2}p_0(L_{p,interior,critical}-W_A)}{20}}}{G_{noise}(f)} \right|; \quad p_0 = 2 \times 10^{-5} \quad (7.7)$$

- The threshold values of BTV for perceiving the seat track vibration in X and Y directions:

$$\Delta M_{B,ST(X,Y),thres}(f) = \left| \frac{a_{ST(X,Y),thres}(f)}{G_{SUS(X,Y)}(f)} \right| = \left| \frac{\sqrt{2}a_{wt_e,ST,thres}/W_d(f)}{G_{SUS(X,Y)}(f)} \right| \quad (7.8)$$

- The threshold values of BTV for perceiving the seat track vibration in Z direction:

$$\Delta M_{B,ST(Z),thres}(f) = \left| \frac{a_{ST(Z),thres}(f)}{G_{SUS(Z)}(f)} \right| = \left| \frac{\sqrt{2}a_{wt_e,ST,thres}/W_k(f)}{G_{SUS(Z)}(f)} \right| \quad (7.9)$$

In the equations above, the frequency weighting filters for the vibrations,  $W_d(f)$ ,  $W_k(f)$ , and  $W_{hi}(f)$  are the factors and they are generated by means of spline interpolation with

the values provided in Table 2 of VDI 2057 Part 1<sup>185</sup> and in Table D1 of VDI 2057 Part 2<sup>186</sup>; whereas the A-weighting filter  $W_A(f)$  is in dB and it is also formed through spline interpolation with the data given in Table 3 of DIN EN 61672-1<sup>187</sup>. For the seat track vibrations in three directions, the same threshold value  $a_{ST,thres} = 0.1 \text{ m/s}^2$  is used. As a result, the threshold values of BPV and BTV of the three vehicles are shown in Figure 7-10. In this figure, FL represents the front left brake, and RL the rear left brake. Similarly, by taking the other subjective scores in the subjective evaluation system, BPV and BTV values for the other corresponding perception levels can also be estimated.

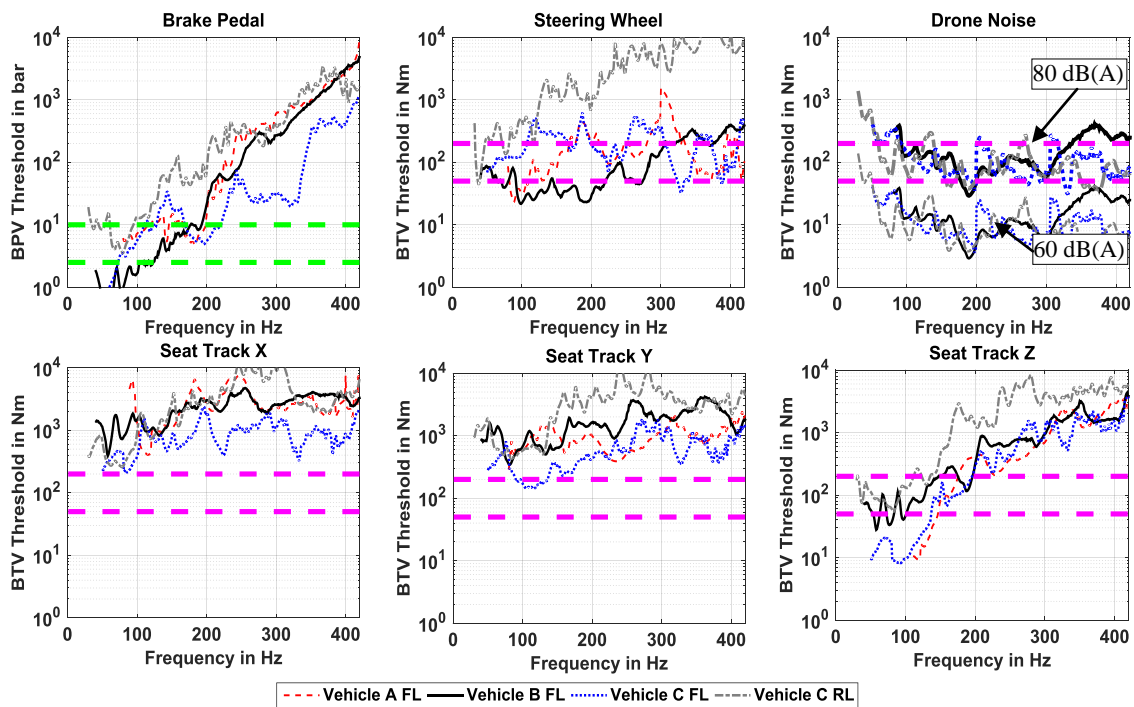


Figure 7-10: Threshold values of BPV and BTV for high-order judder perception

In order to explain the practical meanings of these curves, reference values of BTV and BPV are chosen according to their possible values. For this aim, statistical analyses of the BTV and BPV occurred during the 50 tests with the 100  $\mu\text{m}$  LRO disc of vehicle *B* have been conducted. BTV and BPV amplitudes of the 10<sup>th</sup> and 20<sup>th</sup> orders in the frequency domain with an interval of 20 Hz are shown in Figure 7-11 and Figure 7-12 by using the box plot.

A box plot is a way of graphically depicting groups of numerical data through their quartiles. In the box plot, the distribution of data is displayed based on the five values:

<sup>185</sup> VDI 2057 Part 1, 2002-09, p.19.

<sup>186</sup> VDI 2057 Part 2, 2014-05, p.18.

<sup>187</sup> DIN EN 61672-1, 2014-07, p.21.



minimum, first quartile, median, third quartile, and maximum. The central rectangle spans the first quartile to the third quartile (called the interquartile range, IQR). The median is given by a segment inside the rectangle and the locations of the minimum and maximum are shown by the "whiskers" above and below the box. The whiskers can be alternative values of the minimum and maximum of all of the data, or the lowest and highest data still within 1.5 IQR of the first and the third quartile. The data outside the whiskers are called outliers and plotted as individual points in the box plot.<sup>188</sup> For example, the first and third quartile, the median, the minimum and maximum or the whiskers, as well as the outliers are indicated in Figure 7-11.

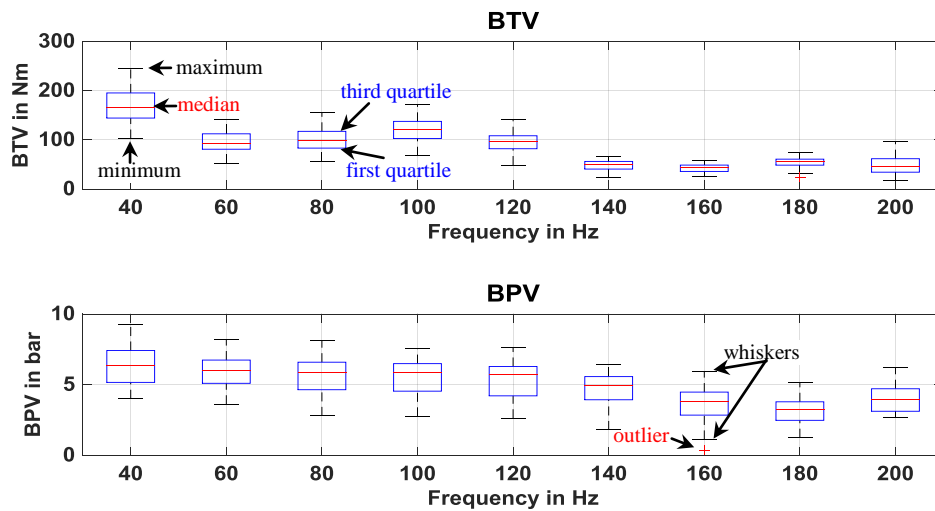


Figure 7-11: Box plot of the 10<sup>th</sup> order BTV and BPV amplitudes, vehicle  $B$ ,  $\Delta z_D \approx 100 \mu\text{m}$

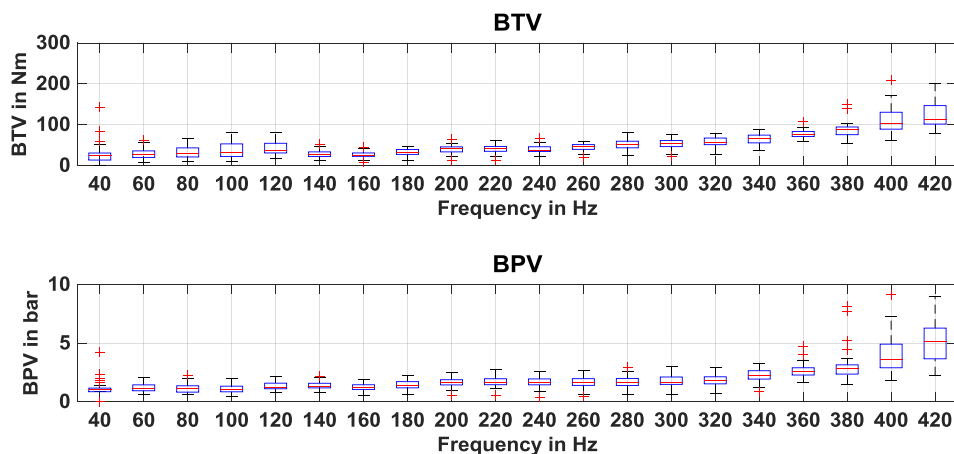


Figure 7-12: Box plot of the 20<sup>th</sup> order BTV and BPV amplitudes, vehicle  $B$ ,  $\Delta z_D \approx 100 \mu\text{m}$

Combining the results in Figure 7-11 and Figure 7-12, amplitudes of the 10<sup>th</sup> order BTV and BPV generally increase with dropping rotational speed, while BTV and BPV ampli-

<sup>188</sup> McGill et al.: Variations of box plots, 1978, p.12–16.

tudes of the 20<sup>th</sup> order decrease during the braking applications. Besides, the maximum amplitudes of the 10<sup>th</sup> order BTV and BPV are higher than those of the 20<sup>th</sup> order. These tendencies are also true when considering the results of the vehicle tests with the other modified discs. For example, the results with the 60  $\mu\text{m}$  DTV disc of vehicle *B* are displayed in Figure C-7 and Figure C-8.

The medians of BTV are mostly around 100 Nm, and the medians of BPV are around 5 bar, seeing from Figure 7-11. The BTV and BPV of the tests with the 100  $\mu\text{m}$  LRO disc of vehicle *B* are generally greater than the BTV and BPV of the tests with the other six modified discs used in this work. In the Fischer's DOE with normal discs and 50 different brake pad prototypes, 100  $\mu\text{m}$  LRO, 60  $\mu\text{m}$  DTV, 200 Nm BTV, and 10 bar BPV are almost the maximum values of the high-order judder occurring even during the drag applications (see Figure C-9). Therefore, giving an interval of [50%, 200%] for the 100 Nm and 5 bar, intervals of [50 Nm, 200 Nm] and [2.5 bar, 10 bar] are selected as references for evaluating the curves of the BTV and BPV threshold values, which are also drawn in Figure 7-10.

The upper values of 200 Nm and 10 bar denote the maximum possible hot judder intensity. Hot judder with BTV and BPV higher than these values is not expected to occur in the normal situations. The lower values of 50 Nm and 2.5 bar are almost the maximum values in the tests with the 20  $\mu\text{m}$  DTV, 30  $\mu\text{m}$  DTV, and 40  $\mu\text{m}$  LRO discs of the rear brake of vehicle *C*. They are used as the values to differentiate between the very strong hot judder that happens rarely in passenger cars after treatments in the phase of brake development and the hot judder that still happens even after the measures taken in the development phase.

Based on the reference values, the driver's perception of high-order judder can be roughly classified into three groups according to the frequency: higher 200 Nm or 10 bar, not perceptible; between 50 and 200 Nm, or between 2.5 and 10 bar, rarely perceptible; lower than 50 Nm or 2.5 bar, easily perceptible. The results are listed in Table 7-3. The results generally correspond to the subjective perceptions of the test persons during the all tests of the three vehicles.

Table 7-3: Classification of the perception of high-order judder induced vibrations and noise

Driver interface	Frequency range											
	from ca.50 to 100 Hz				from 100 to 200 Hz				higher than 200 Hz			
	<i>AF</i>	<i>BF</i>	<i>CF</i>	<i>CR</i>	<i>AF</i>	<i>BF</i>	<i>CF</i>	<i>CR</i>	<i>AF</i>	<i>BF</i>	<i>CF</i>	<i>CR</i>
Brake pedal	●	●	●	●	●	●	●	○	○	○	●	○
Steering wheel	●	●	●	●	●	●	●	○	●	●	●	○
Drone noise	-	●	●	●	-	●	●	●	-	●	●	●
Seat track <i>X</i>	○	○	○	○	○	○	○	○	○	○	○	○
Seat track <i>Y</i>	○	○	○	○	○	○	●	○	○	○	○	○
Seat track <i>Z</i>	●	●	●	●	●	●	●	○	○	○	○	○

\* ○ not perceptible      ● rarely perceptible      ● easily perceptible

*AF*: the front brake of vehicle *A*      *BF*: the front brake of vehicle *B*

*CF*: the front brake of vehicle *C*      *CR*: the rear brake of vehicle *C*

Combining Figure 7-10 and Table 7-3, following conclusions can be drawn with respect to the perception of the vibrations and drone noise induced by the high-order judder:

- The vibrations in the lower frequency range (< 200 Hz) are generally much more relevant to the driver's subjective perception than those in the higher frequency range. Regarding the vibrations at different driver interfaces, specifically:
  - Brake pedal pulsation is only likely to be perceived in the frequency range lower than 200 Hz, especially in the range lower than 100 Hz.
  - Steering wheel oscillation is most likely to be perceived in vehicle *B*, because only 20 to 100 Nm BTV is required in the frequency range up to 300 Hz. However, due to several resonance frequencies it is also possibly to be felt in vehicle *A* and *C*, although normally more than 100 Nm BTV is necessary except for bespoke resonance frequencies.
  - Although the transferability of the suspension system does not show great difference among the three directions (especially between the *Y* and *Z* directions, see Figure 6-6), the vertical car body vibration is generally easily to be perceived by the driver below 200 Hz, whereas the horizontal vibrations are almost unlikely to be felt in the frequency range higher than 50 Hz. This is owing to the different sensitivities of human beings to the vertical vibrations and the horizontal vibrations (Figure 7-8).
- On the contrary to the vibrations, drone noise can be very easily heard in the whole frequency range above 50 Hz, especially in the range above 100 Hz, for both vehicle *B* and *C*. 10 Nm BTV can already cause hearable noises and 50 Nm

BTV can sometimes result in unacceptable noises. Consequently, drone noise should be the main reason for potential customer complaints about high-order hot judder.

- Comparing with the excitations from the front brakes, the vibrations caused by the high-order hot judder in the rear brake are much less significant to the driver's perception at all the driver interfaces. However, the driver's sensitivity to the drone noises caused by the front brakes and the rear brake are nearly on the same level. Therefore, customer complaints about the high-order hot judder in rear brakes normally can only be attributed to the drone noise.

Besides, although the lower-frequency vibrations are much more significant to driver's perception than the higher-frequency vibrations, considering that lower orders can also be induced by some specific hot spot patterns as discussed in 4.5.3, in such circumstances, the hot judder with high-number hot spots may also lead to customer complaints because of the vibrations instead of the drone noise.

## 8 Conclusion and outlook

### 8.1 Conclusion

Based on the current situations that high-order hot judder has been detected in many dynamometer tests and it has been the focus of most hot judder researches, the practical influences of the high-order hot judder on the driver's subjective perception is established as the ultimate goal of this work. For this aim, two relating aspects are investigated in this work: the incidence of high-order hot judder in the vehicle tests and the perception thresholds of the high-order hot judder.

Concerning the incidence of high-order judder in vehicles, the transferability from the brake dynamometer tests to the vehicle tests performed on the test tracks and at the chassis dynamometer has been studied, by comparing the hot judder behaviors of one front brake and one rear brake among these tests. Hot judder was very sensitive to the test conditions (e.g. stop braking or drag braking, and the control methods of the tests) and the test equipments (brake dynamometer, chassis dynamometer, or test track). The front brake was dominant with the 1<sup>st</sup> to 4<sup>th</sup> lower judders in the tests. The rear brake was dominant with 9<sup>th</sup> to 15<sup>th</sup> higher dominant order in the drag braking applications carried out at the brake dynamometer and the chassis dynamometers, while it was dominant with 1<sup>st</sup> to 5<sup>th</sup> lower orders in the stop braking applications performed during the brake dynamometer tests, the vehicle chassis dynamometer tests, and the vehicle road tests. By comparing the thermal increases of BTV and BPV amplitudes and the dominant orders of BTV among the tests under similar testing conditions, it was manifested that the dynamometer test results cannot exactly represent the real hot judder characteristics in a vehicle and thus the hot judder behaviors are not transferable from the brake dynamometer tests to vehicle tests. However, hot judder seems more likely to happen at the brake dynamometer than in the vehicle tests. Therefore, the brake dynamometer is a helpful tool for detecting the potential occurrence of hot judder in the early phase of brake development, so as to prevent the happening in the vehicle. Although only two brakes are compared in this investigation, it is the first direct comparison of the hot judder behaviors among different tests with identical brake components. It provides a reference regarding hot judder testing for the brake manufactures.

Besides, four passenger cars have been inspected regarding the hot judder occurrence. No evident high-order hot judder was identified in all the production brakes of the four cars. It seems that the high-order hot judder could be well mitigated or even prevented, only by the measures taken in the wheel brakes.

The perception of high-order judder was mainly studied by investigating the global transfer behaviors from BPV/BTV to the driver interface. A novel test method was employed, which is identifying the global transfer functions by using artificially modified discs simulating the high-order DTV or LRO. Altogether three vehicles with seven different modified discs have been tested and the transfer functions of BPV causing the brake pedal pulsation and of BTV causing the steering wheel oscillation, the car body vibrations in the directions, and the drone noise near the driver's ear were identified. The threshold values of the driver interface vibrations were obtained by subjective ratings by test persons, two critical levels of drone noise were selected according to the general vehicle total noise level and humans' perception characteristics of noise. Based the threshold values of the driver interface quantities and the transfer functions, the threshold values of BTV and BPV were calculated. In the frequency range higher than 100 Hz, drone noise is the most possible reason causing customer complaints, since less than 10 Nm BTV can already bring hearable drone noise ( $> 60$  dB(A)), and 50 Nm BTV can sometimes result in unacceptable noise ( $> 80$  dB(A)). Comparing with drone noise, the vibrations caused by the high-order judder is less possibly to affect the driver. Generally more than 20 Nm BTV or 2.5 bar BPV are required to cause perceptible vibrations. The perceptible vibrations are more possibly as the steering wheel oscillation and the vertical vehicle vibration, other than the horizontal vehicle vibrations or brake pedal pulsation. Normally, for the high-order hot judder with a BTV smaller than 50 Nm, its induced high frequency vibrations ( $> 100$  Hz) could rarely cause customer complaints. However, lower orders can be resulted in due to some specific hot spot patterns. In such cases, hot judder with a high number of hot spots may also lead to customer complaints.

From the results of the transfer behaviors and the perception thresholds, following conclusions can be drawn regarding the mitigation strategies of high-order hot judder:

- The best ways to mitigate the vibrations at the driver's interface would be reducing the occurrence by the measures in the wheel brakes, since generally more than 50 Nm BTV is required for a perceptible vibration, and since as found in the comparison test and the identification tests with production brakes that preventing a fierce high-order hot judder in the vehicle is totally possible.
- The most efficient ways to reduce the drone noise would be improving the sound isolation capability of the vehicle, and avoiding the obvious resonances of vehicle components, for example, the resonance of the dash board.
- In order to reduce the transmission, avoiding the obvious resonances in the transfer paths should be the most effective method. However, integrated optimization of the axle kinematics, the chassis mounts, and the stiffness and damping of the steering system should be the best solution to improve the overall robustness against high-order hot judder, considering the existence of the plenty of peaks in every transfer path.

## 8.2 Outlook

The investigations about the incidence and transfer behaviors of high-order hot judder carried out in this work, brought out some new questions and research tasks. The transferability of hot judder tests from the brake dynamometer to the vehicles needs to be further examined by more other brakes, especially the brakes that also show evident high-order hot judder in stop braking applications. Besides, the influential factors of the transferability, like the hydraulic layouts of the braking systems, the control systems of the dynamometers, the cooling rate of the brake discs, and also the support stiffness of the wheel brakes need to be inspected by more specialized tests. For example, in order to exclude the influence of the suspension system on the hot judder behaviors,  $\frac{1}{4}$  car can be used in the brake dynamometer tests. The influences of the hydraulic layouts and the control system can be verified by modifying the hydraulic layout of the brake dynamometer (e.g. removing the throttle; shutting the hydraulic control system down, and exerting a constant braking pressure to the whole hydraulic system by a specially designed valve at the beginning of the braking application). The role that the cool rate plays can be testified by varying the cooling power of the brake dynamometer.

The transfer behaviors of only three vehicles have been studied by using modified discs simulating the 10<sup>th</sup> and the 20<sup>th</sup> order DTV or LRO. Further investigations with more vehicles and brake discs with the other surface forms, especially the brakes with normal discs that show strong high-order hot judder, would be helpful to draw more convincing conclusions. Besides, a validated whole vehicle MBS model would also be helpful to obtain more knowledge of the transfer behaviors, for example, the transfer behaviors of the specific components, or subsystems in the transfer paths, and the sources of the resonances in the global transfer functions.

Regarding the perception of high-order judder, the threshold values for hearing the drone noise can also be identified by subjective ratings. However, a reliable correlation between the subjective rating and the objective parameters of drone can only be obtained by a statistical result composed of various tests and subjective ratings by a considerable amount of test persons. This also applies to the vibrations. In the regression analysis of this research project, only six test persons were involved. The results could contain considerable errors comparing with the reality. The correlation obtained in this work needs to be verified by further investigations. However, the basic method used in the regression analysis provides a reference for further more specific investigations of the human perceptions to the vibrations caused by the high-order hot judder or the like.

Besides, since the lower-frequency vibrations are much more significant to driver's perception than the higher-frequency vibrations, the root causes of the lower orders produced by the hot judder with a high number of hot spots ought to be explored.

---

## **A Statistics of the hot judder investigations from literatures**

A statistic of 23 hot judder tests carried out by different authors is listed in Table A-1, in which the last name of the author, the publication year, the number of hot spots (dominant order of hot judder), the maximum number of hot spots (maximum dominant order of hot judder), the applied test equipment as well as the main test design are given. Most of the tests have been carried out at the brake dynamometer, only four out of the 23 tests are vehicle tests. Besides, around 10 hot spots have been detected by most authors.



Table A-1: Statistics of the carried out hot judder investigations

Year	Author	Nr. of hot spots	Max. Nr.	Equipment	Main test design
2001	Fieldhouse	2	2	dynamometer	drag braking, 1500, 1633 rpm; 4-5.5 bar
2008	Bryant	1-3	3	dynamometer	drag braking, 1200 rpm, 16 bar, 600 Nm
1997	Grochowicz	1-3	3	dynamometer	stop braking from 170 and 100 km/h
1968	Inoue	ca.1-4	4	dynamometer	stop braking from 100, 200 km/h; 0.3 g
2004	Panier	6	6	dynamometer	rising velocity from 60 to 300 km/h and from 60 to 120 km/h
2007	Kim	6	6	dynamometer	drag braking, 1800 rpm
2000	Kao	7	7	dynamometer	stop braking from 966 to 552 rpm, 0.19 g
2006	Bryant	8	8	vehicle	braking from 240 to 50 km/h, 0.2-0.4 g
2008	Cho	6-8	8	dynamometer	stop braking from 800 rpm to until ca. 2200 rpm with a step of 100 rpm
1998	Lee	ca. 9	9	vehicle	braking from 160 km/h, 0.2 g
2012	Kasem	mainly 9	9	dynamometer	stop braking with different initial speeds between 68 and 204 km/h
2015	Ruan	7-9	9	dynamometer	stop braking, 1000, 1250, 1500, 1750, 200 rpm; 5, 10, 20, 30 bar
2015	Okamura	7-9	9	dynamometer	stop braking from 220 to 0 km/h, 0.2 g
1998	Little	ca. 10	10	dynamometer	stop braking from 103 and 164 to 0 km/h, 15, 30bar
1998	Kubota	8-10	10	vehicle	braking from 200 to 50kmh, 0.29 g
2002	Yi	3-10	10	dynamometer	drag braking, 416, 555, 694, 833 rpm; 254, 191, 153,127 Nm
2010	Honner	10	10	dynamometer	drag braking, 1200 rpm
2008	Litos	8-10	10	-	-
1985	Kreitlow	7-11	11	vehicle/ dynamometer	stop braking from 170 to 60 km/h
1998	Steffan	11 and 13	13	dynamometer	stop braking from 155 to 0 km/h, 15 bar
2015	Fischer	mainly 9-15	15	dynamometer	drag braking 175, 200, 225 km/h; 5, 10 15, 20, 30 bar; 100, 150, 200, 250, 300 Nm
2008	Sardá	10-17	17	dynamometer	stop braking from 240 and 210 to 80 km/h, 10 bar or 310,420,530 Nm; drag braking with 140, 160, 200 km/h, 310,354, 248Nm
2003	Lee	1-20	20	vehicle	stop braking from 64.4, 80.5, 96.6,104.7, 112.7 km/h; 0.2 g and 0.5 g

---

## B Test and evaluation methodology

### B.1 Dynamometer setup of rear brake test

Figure B-1 shows the brake dynamometer test setup for the rear brake testing in the comparison test of chapter 4. Similar quantities are measured and similar sensors are adopted as those in the tests of the front brake.

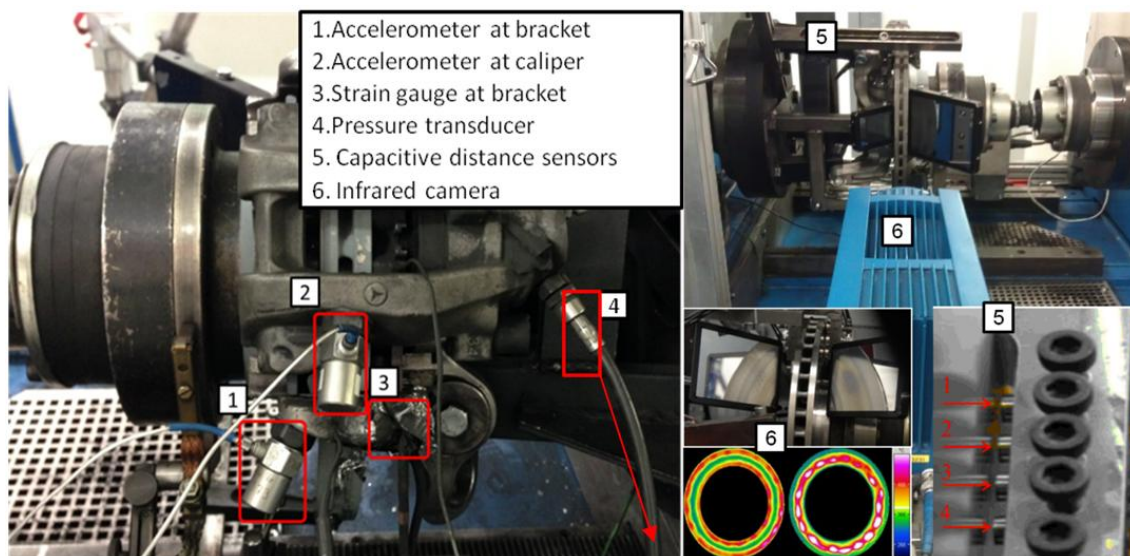


Figure B-1: Brake dynamometer test setup for the rear brake testing

### B.2 Examples of non-uniform hot spots

A thermal image of one dynamometer test from Fisher's DOE<sup>189</sup> is shown in Figure B-2. The thermal image is the 700<sup>th</sup> rotation (ca. 22.6 s) of a drag braking application with 225 km/h and 200Nm. The examples of narrower hot spots and weaker hot spots are indicated on the piston-side disc. Order analyses of the thermal variations at the two disc radii marked by the black lines (outer ring and inner ring) in Figure B-2 are displayed in Figure B-3, and order analyses of BTV and DTV of this test are exhibited in Figure B-4. From these results it is clear that various adjacent orders are resulted in the different signals. Due to the irregular hot spot distribution on the finger side disc, the

---

<sup>189</sup> Fischer et al.: Ordnungsanalyse von Heißrubbeln, 2015

adjacent orders of BTV and DTV are not exactly correlated with those of the thermal variations.

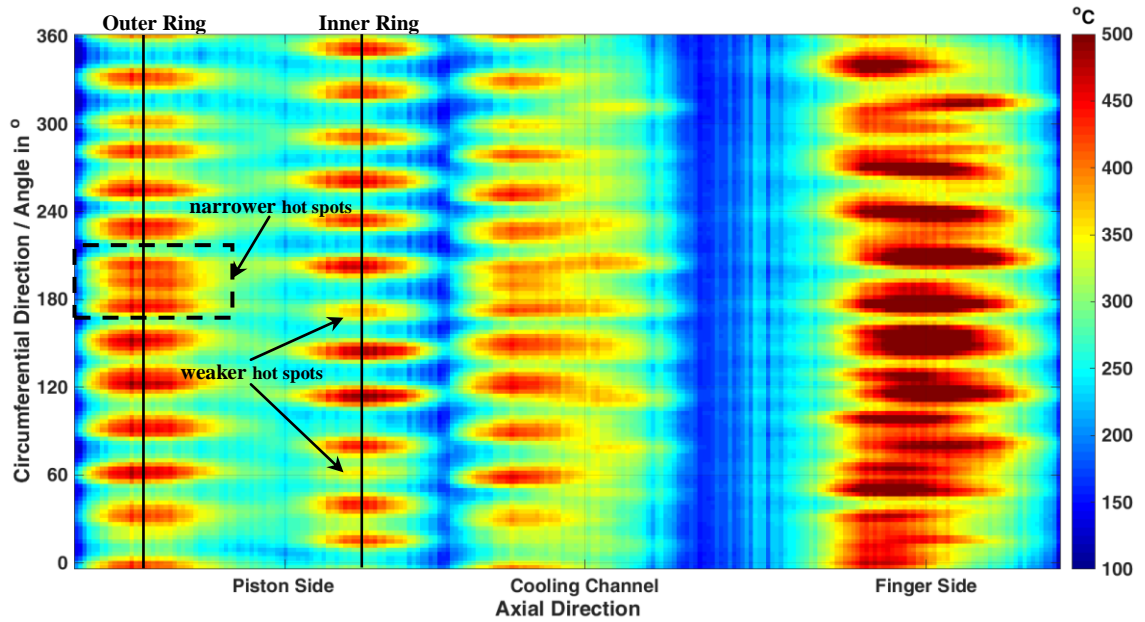


Figure B-2: Thermal image of one drag braking application at the brake dynamometer with 225 km/h and 200 Nm, from 100 to 500 °C, the 700<sup>th</sup> rotation

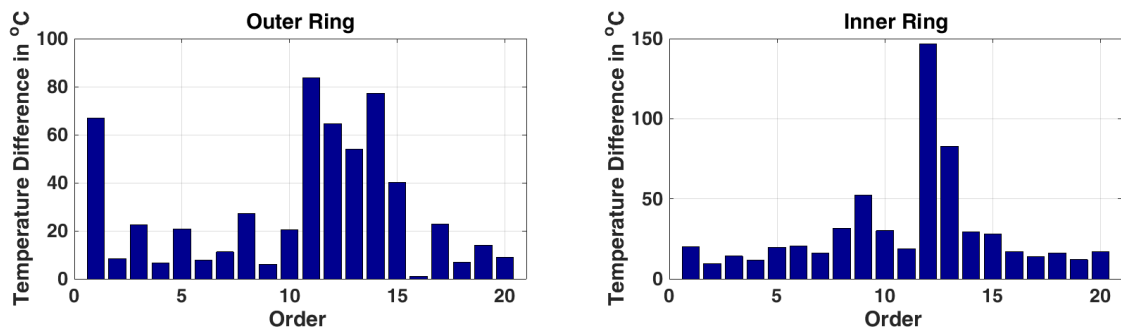


Figure B-3: Order analysis of the thermal variations at the two disc radii marked by the black lines in Figure B-2, the 700<sup>th</sup> rotation

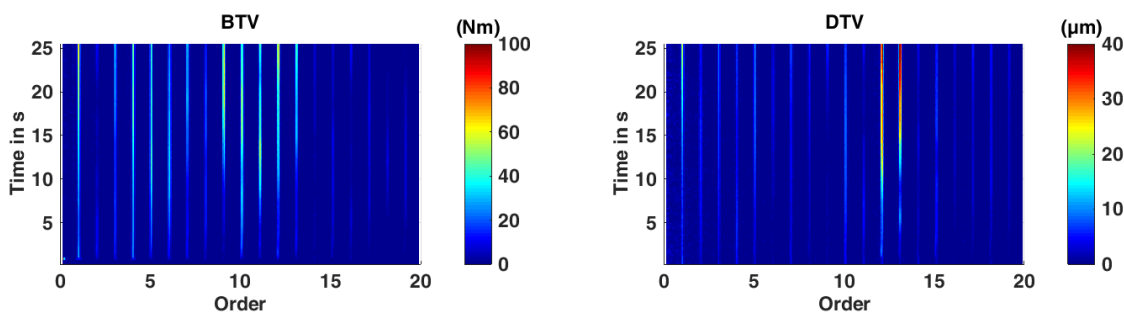


Figure B-4: Order analysis of BTV and DTV, drag braking application at the brake dynamometer with 225 km/h and 200 Nm, from 100 to 500 °C

### B.3 Order analysis of the thermal variation

Figure B-5 exhibits the thermal variations at the two disc radii marked by the two black lines in the 30 s thermal image of Figure 4-22 as well as the order analyses of the thermal variations. The 1<sup>st</sup> to 3<sup>rd</sup> lower orders are much greater than the higher orders.

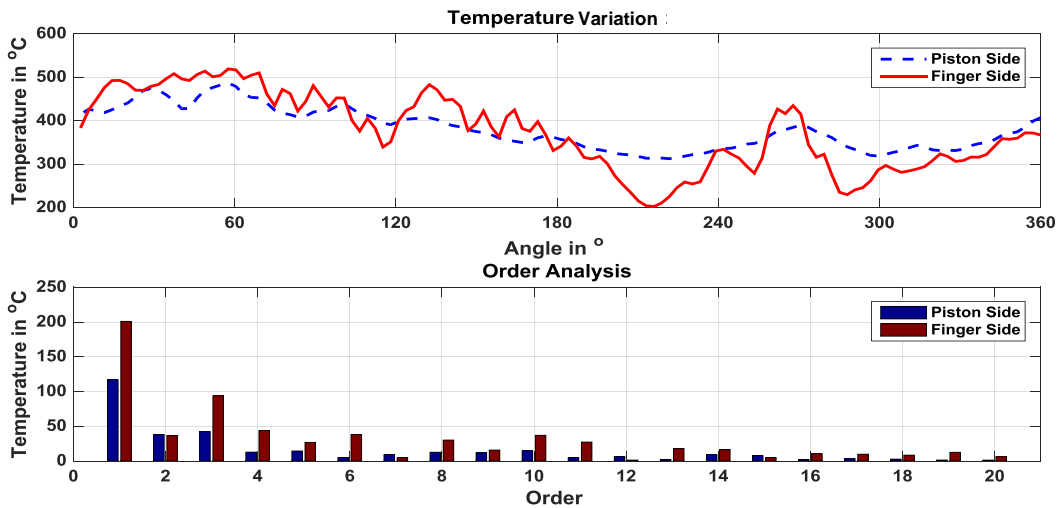


Figure B-5: Thermal variations and their order analyses of one drag braking of the front brake, braking with 225 km/h and 10 bar, from 100 to 500 °C

### B.4 Order analysis of BTV, BPV, DTV, LRO

Figure B-6 shows the order analysis of the BTV, BPV, DTV, and LRO signals for the drag braking application mentioned in the explanation of the AM mechanism, causing adjacent orders. Generally the 9<sup>th</sup> to 14<sup>th</sup> adjacent orders are induced in the signals.

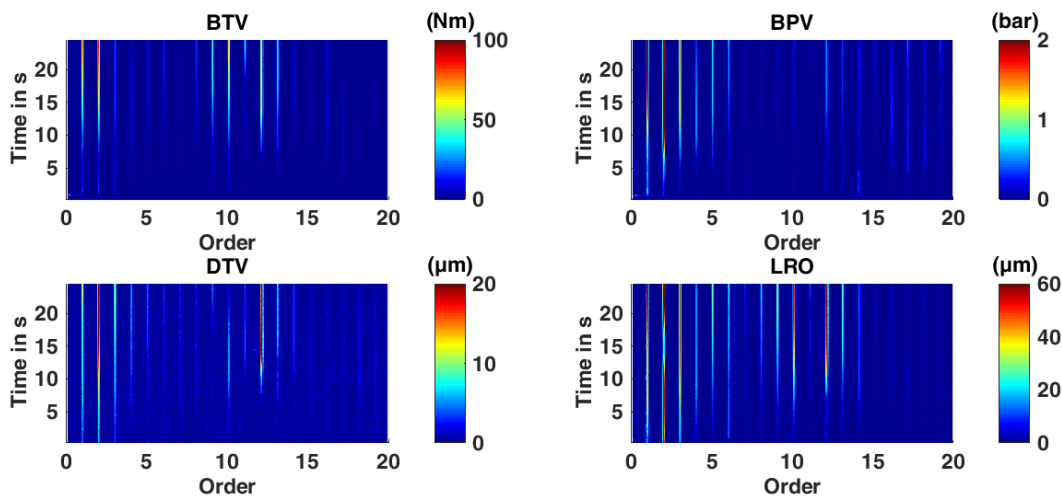


Figure B-6: Order analysis of BTV, BPV, DTV, and LRO for a drag braking application of the rear brake with 225 km/h and 250 Nm, from 100 to 500 °C

## C Test results

### C.1 Influence of adapter stiffness on the order behaviors

The dominant orders of BTV, BPV, LRO, and DTV are not reproducible in the tests with two different adapters. The influence of the adapter stiffness on the order behaviors of hot judder is not consistent under different testing conditions.

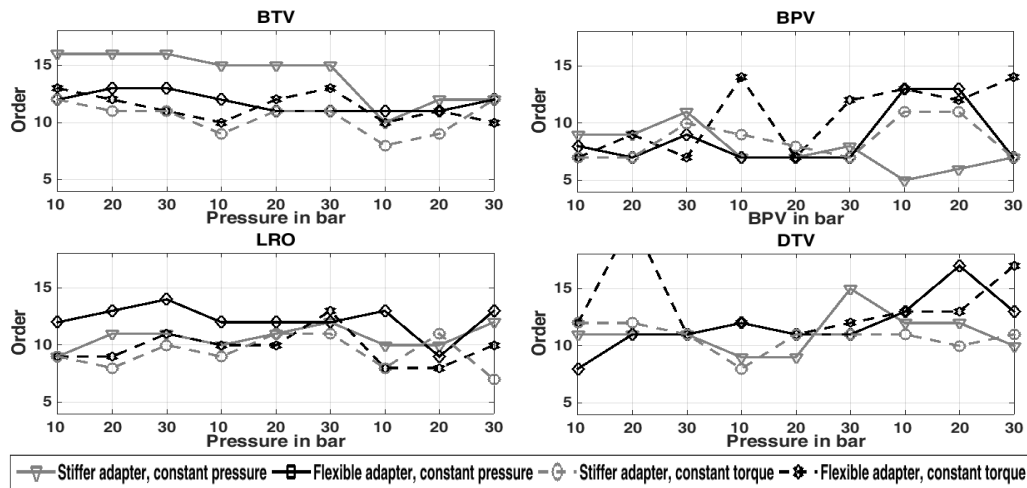


Figure C-1: Comparison of the order behaviors by using two different knuckle adapters

### C.2 The post-processing anti-aliasing filter used for the WFS signals

Because the actual sampling rate of the WFS is 1 kHz, aliasing effects are induced in the signals acquired by the WFS. In order to eliminate the aliasing effects, an anti-aliasing filter is applied during the data processing. Figure C-2 shows the raw BTV spectrum with the folding of the higher orders. The folding signals of the 30<sup>th</sup>, 40<sup>th</sup>, and 50<sup>th</sup> orders are marked with arrows. The principle of the anti-aliasing filter is:

- Because the dominant orders in the spectral diagram are the 10<sup>th</sup> order and its harmonics, the 10<sup>th</sup> to 100<sup>th</sup> (the highest harmonic that can be differentiated from the background noise in the BTV spectrum) order lines and their folding order lines are separately extracted based on the relationship among the frequency  $f$ , the rotational speed  $n$ , and the judder order  $N$ :

- for the order lines

$$f = N \cdot n \tag{C.1}$$

- for the folding order lines

$$f = 1000 - N \cdot n \tag{C.2}$$

- The amplitudes of those sample points that are centered with the folding order lines within a bandwidth of 11 Hz are all set to 0, except for the intersection points with the order lines.
- Intersection points between the folding order lines and the order lines are determined by comparing the frequencies of the points on the same rotational speed axis:

$$|f_j - f_j| < 6 \tag{C.3}$$

where  $j$  is the index of the rotational speed array  $\mathbf{n}$ . The points that satisfy equation C.3 are considered to be the intersection points within the 11 Hz bandwidth, and their amplitudes are kept unchanged.

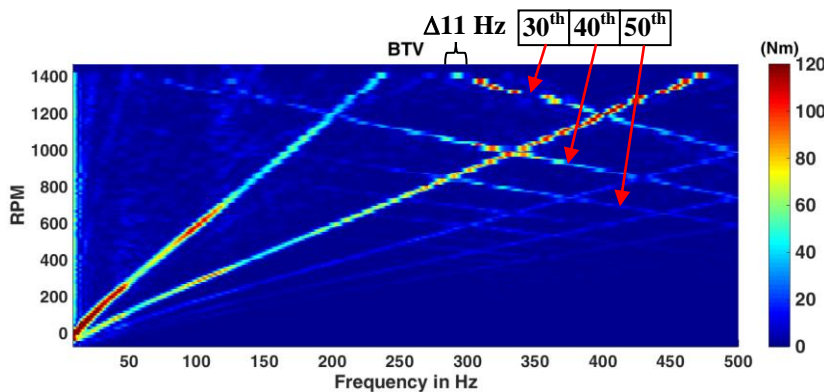


Figure C-2: BTV spectrum with aliasing effects, one test of vehicle  $B$ ,  $\Delta d_D \approx 60 \mu\text{m}$

By using this filter, the aliasing effects are eliminated. The BTV spectrum without the aliasing effect is displayed in Figure C-3.

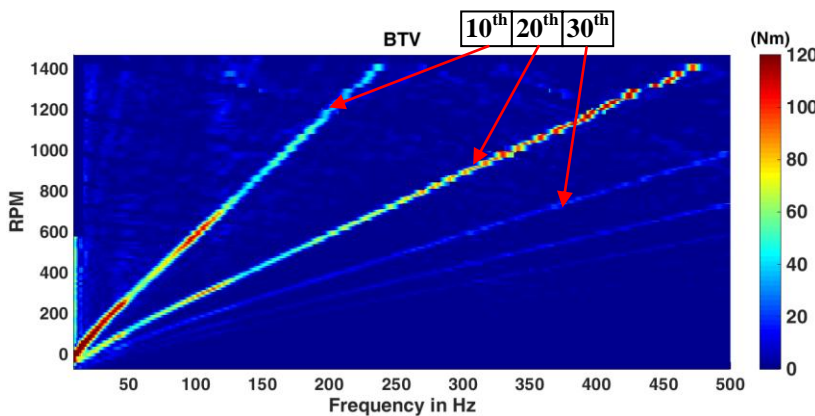


Figure C-3: BTV spectrum without aliasing effects, one test of vehicle  $B$ ,  $\Delta d_D \approx 60 \mu\text{m}$

## C.3 Time signals of one test with a modified disc

Figure C-4 displays the time signals of the test used in the spectral analyses shown in Figure 6-2. Some resonance frequencies can be seen from the driver interface quantities, especially in the accelerations of the brake pedal and the steering wheel, as well as in the transverse and vertical seat track vibrations, indicated by the peaks of the signals at some specific driving speed (corresponding to some specific frequency).

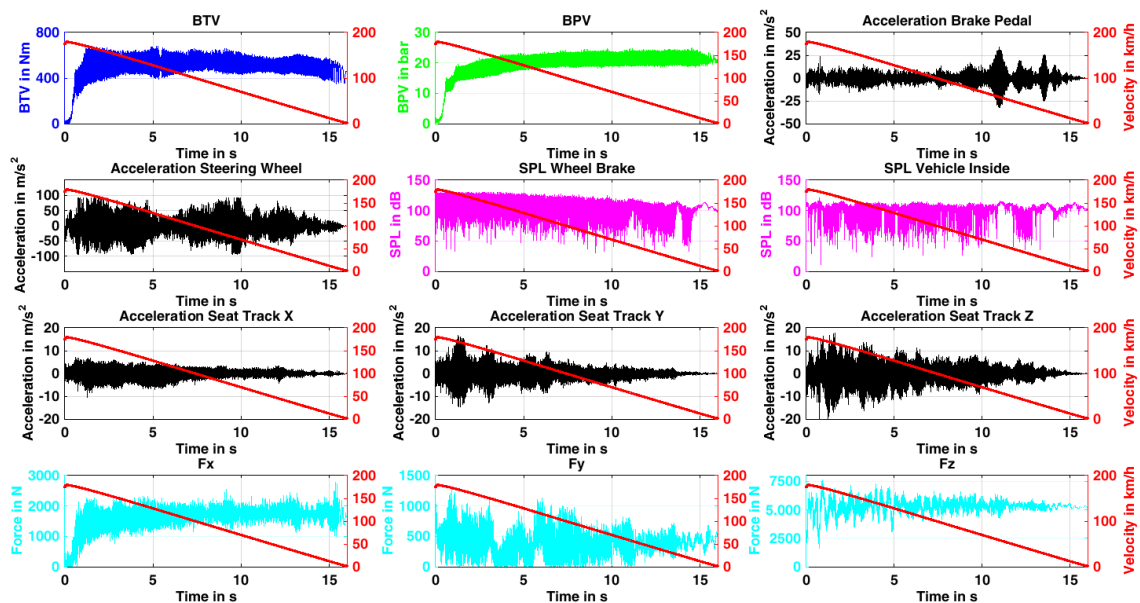


Figure C-4: Time signals of one test with vehicle *B*,  $\Delta d_D \approx 60 \mu\text{m}$ , from 180 to 0 km/h with  $0.31 \text{ m/s}^2$ , from  $50 \text{ }^\circ\text{C}$

## C.4 High-order judder of the rear brake

Spectral analyses of the driver interface quantities of one test with the  $40 \mu\text{m}$  LRO disc in the rear left brake of vehicle *C* are shown in Figure C-5. Steering wheel oscillation is also excited by the judder excitation at the rear brake, although there is no direct connection between the rear axle and the steering system. However, both the frequency characteristics and the amplitudes of the brake pedal and steering wheel vibrations are very similar with those of the seat track vibrations. This suggests that the vibrations of the brake pedal and the steering wheel are strongly influenced by or chiefly caused by the vibrations of the whole vehicle body.

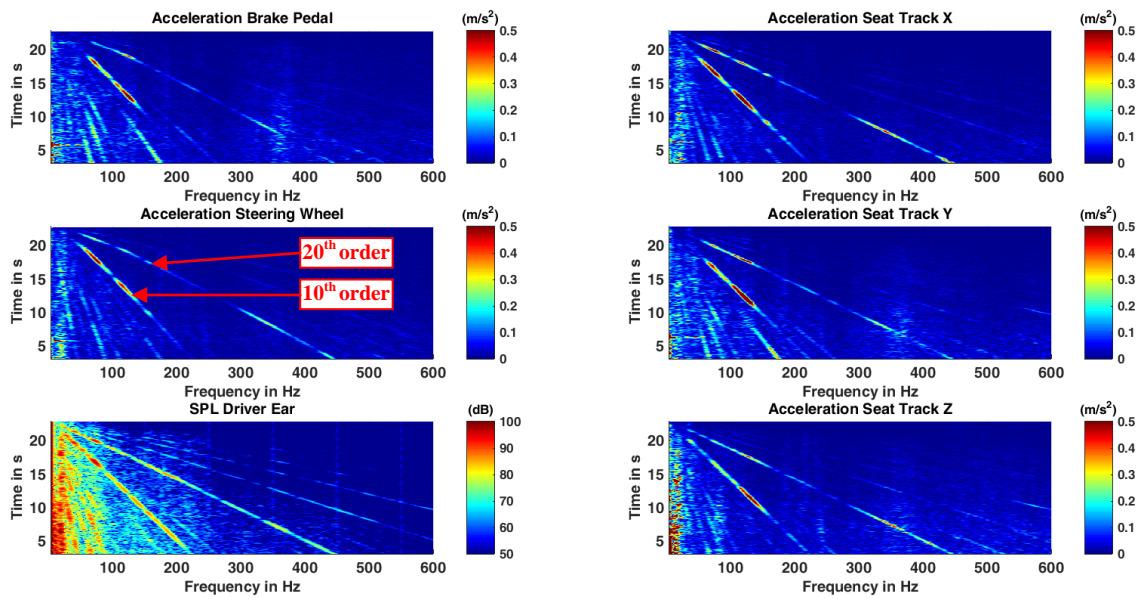


Figure C-5: Spectral diagrams of one test with the 40  $\mu\text{m}$  LRO disc in the rear left brake of vehicle C, braking from 180 km/h and 50 °C with 0.22 g

## C.5 SPL spectrum of exterior drone noise

Figure C-6 shows one spectral diagram of the drone noise near the wheel brake. It is clear that the 10<sup>th</sup>, 20<sup>th</sup>, and 30<sup>th</sup> orders are not always much stronger than the “background noises”. Therefore, the extracted 20<sup>th</sup> order lines used in the calculation of the acoustic efficiency might contain errors, which might be the reason for the discrepancy between the results obtained by the two different brake discs of vehicle B in Figure 6-12.

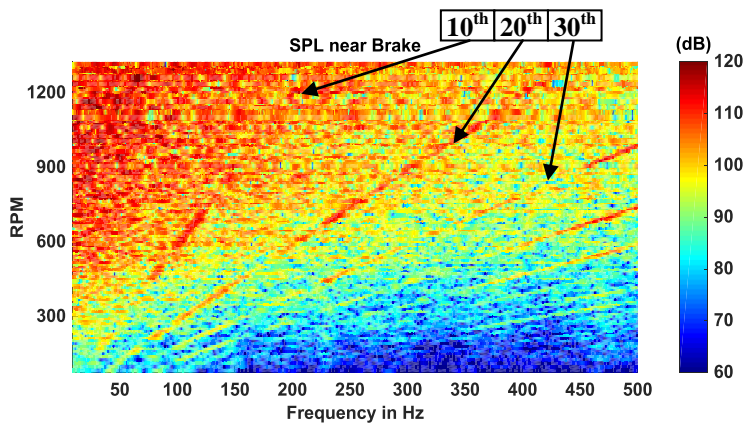


Figure C-6: SPL spectral diagram of the drone noise near the wheel brake, one test of vehicle B with the 100  $\mu\text{m}$  LRO disc, decelerating with 0.22 g from 160 km/h



## C.6 Amplitudes of BTV and BPV

From the 50 tests with the 60  $\mu\text{m}$  DTV disc of vehicle *B*, amplitudes of BTV and BPV for the 10<sup>th</sup> and 20<sup>th</sup> orders in the frequency domain are separately displayed in Figure C-7 and Figure C-8. During the braking (the frequency is decreasing), BTV and BPV amplitudes of the 10<sup>th</sup> order are increasing, while those of the 20<sup>th</sup> order are decreasing. This agrees with the results by using the 100  $\mu\text{m}$  LRO disc of vehicle *B*, shown in Figure 7-11 and Figure 7-12. Besides, amplitudes of BTV and BPV caused by the 100  $\mu\text{m}$  LRO disc are generally smaller than those caused by the 60  $\mu\text{m}$  DTV disc.

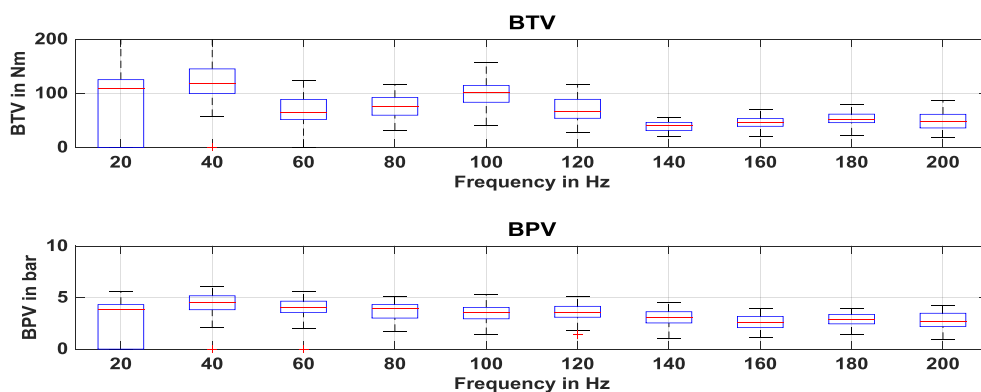


Figure C-7: 10<sup>th</sup> order of BTV and BPV caused by the 60  $\mu\text{m}$  DTV disc of vehicle *B*

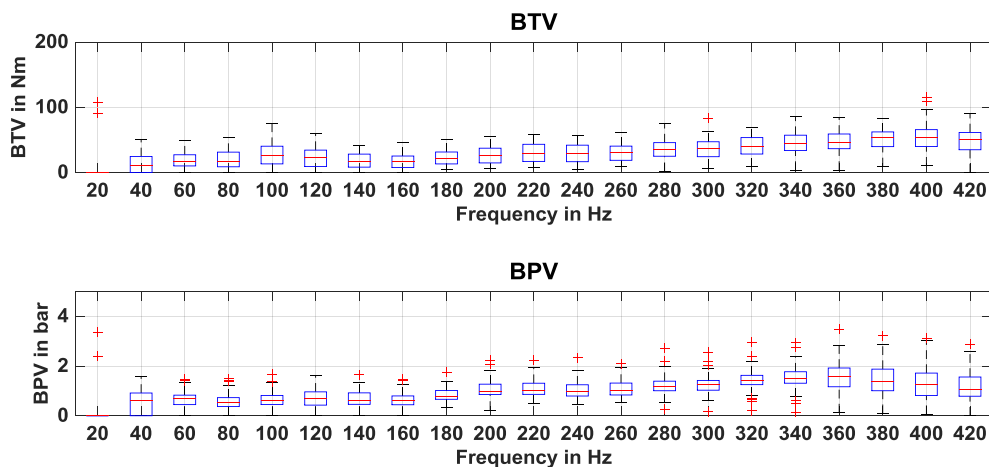


Figure C-8: 20<sup>th</sup> order of BTV and BPV caused by the 60  $\mu\text{m}$  DTV disc of vehicle *B*

Figure C-9 shows the maximum values of BTV and LRO (SRO in the Figure) for the 1<sup>st</sup> to 20<sup>th</sup> orders. The values are of the 1500 tests carried out by Fischer with 50 different brake pad prototypes through drag braking applications at the brake dynamometer. Seeing from the higher dominant orders (9<sup>th</sup> to 15<sup>th</sup>), for the most tests, LRO is lower than 100  $\mu\text{m}$ , and BTV is within 200 Nm. Considering all the 1<sup>st</sup> to 20<sup>th</sup> orders, BTV is smaller than 50 Nm for the most tests.

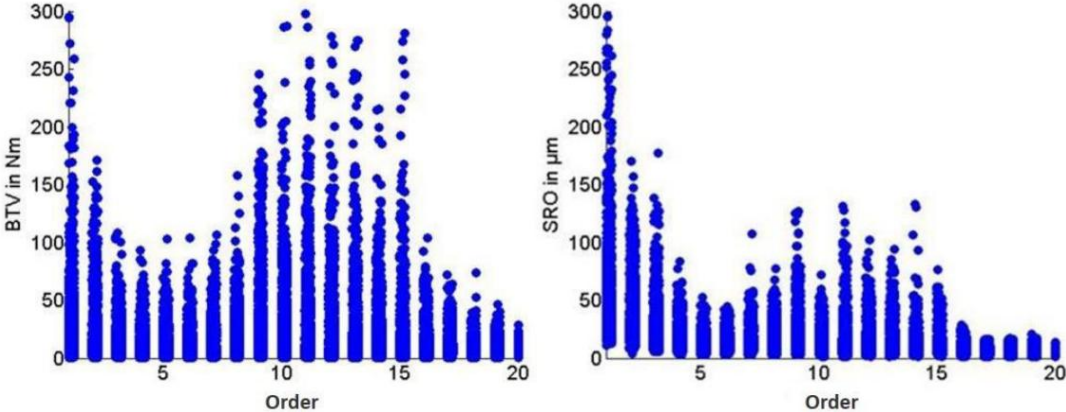


Figure C-9: BTV and LRO for all the drag braking applications of Fischer’s DOE<sup>190</sup>

---

<sup>190</sup> Fischer et al.: Ordnungsanalyse von Heißrubbeln, 2015, p.8.

---

## Reference

- A&D Company, L.:** Wheel Force Sensor. Online available under: <http://www.aandd.jp/products/dsp/wfs.html>, latest accessed at 29.05.2016.
- Abdelhamid, M. Khalid; Bray, W.:** Braking systems creep groan noise: detection and evaluation. SAE Technical Paper 2009-01-2103. In: SAE 2009 Noise and Vibration Conference and Exhibition, May. 19, 2009.
- Anderson, A. E.; Knapp, R. A.:** Hot spotting in automotive friction systems. In: *Wear* 135 (2), 1990, p.319–337. DOI: 10.1016/0043-1648(90)90034-8.
- Augsburg, D.-I. Klaus; Brunner, D.-I. Horst; Grochowicz, D.-I. Jaroslaw.:** Untersuchungen zum Rubbelverhalten von Pkw-Schwimmsattelbremsen. In: *ATZ Automobiltech Z* 101 (1), p.22–30.
- Barber, J. R.:** Frictionally excited thermoelastic instability (TEI). University of Michigan. Online available under: <http://www-personal.umich.edu/~jbarber/TEI.html>, latest accessed at 15 April.2016.
- Barber, J. R.:** The influence of thermal expansion on the friction and wear process. In: *Wear* 10 (2), 1967, p.155–159. DOI: 10.1016/0043-1648(67)90087-7.
- Barber, J. R.:** Thermoelastic instabilities in the sliding of conforming solids. In: *Proceedings of the Royal Society of London. Series A, Mathematical and Physical Sciences* 312 (1510), 1969, p.381–394.
- Bauer, C.:** Untersuchung des Einflusses einer schwingungsfähigen Messvorrichtung auf detektierte Bremsmomentschwankungen am Schwungmassenprüfstand. Nr.511/12. Master Thesis, Technische Universität Darmstadt, Darmstadt, Germany, 2012.
- Bellmann, M. A.:** Perception of whole body vibrations: From basic experiments to effects of seat and steering wheel vibrations on the passenger's comfort inside vehicles. PhD Thesis, Universität Oldenburg, Oldenburg, Germany, 2002.
- Bendat, J. S.; Piersol, A. G. (Ed.):** Random data. Analysis and measurement procedures Julius S. Bendat, Allan G. Piersol. 4. Aufl. Hoboken, New Jersey: Wiley-Interscience Wiley series in probability and statistics. ISBN: 978-0-470-24877-5, 2010.
- Bittner, C.:** Reduzierung des Bremsrubbelns bei Kraftfahrzeugen durch Optimierung der Fahrwerkslagerung. PhD Thesis, Technische Universität München, München, Germany, 2006.
- Breuer, B.; Bill, K. H. (Ed.):** Brake technology handbook. Warrendale, Pa.: SAE International SAE-R, 375. ISBN: 978-0-7680-1787-8, 2008.

**Bryant, D.; Crampton, A.; Fieldhouse, J. D.; Talbot, C. J.:** Discussion of characteristics of brake judder and the necessary data acquisition system for complete analysis. In: *Proceedings of Computing and Engineering Annual Researchers' Conference*. University of Huddersfield. Huddersfield, 2006.

**Bryant, D.; Fieldhouse, J.; Crampton, A.; Talbot, C.; Layfield, J.:** Thermal brake judder investigations using a high speed dynamometer. SAE Technical Paper 2008-01-0818. In: *Brake Technology*, 2008.

**Bryant, D.; Fieldhouse, J. D.; Talbot, C. J.:** Brake judder - an investigation of the thermo-elastic and thermo-plastic effects during braking. In: *Int. J. Vehicle Structures & Systems* 3 (1), 2011. DOI: 10.4273/ijvss.3.1.07.

**Burton, R. A.; Nerlikar, V.; Kilaparti, S. R.:** Thermoelastic instability in a seal-like configuration. In: *Wear* 24 (2), 1973, p.177–188. DOI: 10.1016/0043-1648(73)90230-5.

**Cho, H.:** Experimental study on thermo-elastic behavior of automotive disk brake. PhD Thesis. Inha University, Incheon, South Korea, 2008.

**Cho, M. Hyung; Kim, D. Sun; Yang, S. Hong; Cho, Y. Sun; Lee, J. Ju; Kim, C. Jin.:** A study of the influence of pad properties and disc coning on high speed judder. SAE Technical Paper 2012-01-1815. In: *SAE 2012 Brake Colloquium & Exhibition - 30th Annual*, September. 23, 2012.

**Day, A. J.; Tirovic, M.; Newcomb, T. P.:** Thermal effects and pressure distributions in brakes. In: *Proceedings of the Institution of Mechanical Engineers, Part D: Journal of Automobile Engineering* 205 (3), 1991, p.199–205. DOI: 10.1243/PIME\_PROC\_1991\_205\_171\_02.

**de Vries, A. and Wagner, M.:** The brake judder phenomenon. SAE Technical Paper 920554. In: *International Congress & Exposition*, February. 24, 1992, Warrendale, PA, United States, 1992.

**DIN EN 61672-1.:** Elektroakustik - Schallpegelmesser - Teil 1: Anforderungen, 2014-07.

**DIN ISO 226.:** Normal equal-loudness-level contours, 2006-04.

**Dow, T.; Burton, R. A.:** Thermoelastic instability of sliding contact in the absence of wear. In: *Wear* 19 (3), 1972, p.315–328. DOI: 10.1016/0043-1648(72)90123-8.

**Du, F.:** Identifikation der Heißrubbeln-beeinflussenden Eigenfrequenzen in Pkw. Master Thesis, Technische Universität Darmstadt, Darmstadt, Germany, 2015.

**Duan, C.; Singh, R.:** Analysis of the vehicle brake judder problem by employing a simplified source-path-receiver model. In: *Proceedings of the Institution of Mechanical Engineers, Part D: Journal of Automobile Engineering* 225 (2), 2011, p.141–149. DOI: 10.1177/09544070JAUTO1629.

**Dufrénoy, P.; Brunel, J.-F.:** Thermal localizations in friction brakes. SAE Technical Paper 2008-01-2568. In: 26th Brake Colloquium and Exhibition, October. 12, 2008.

**Engel, H. Georg.:** Systemansatz zur Untersuchung von Wahrnehmung, Übertragung und Anregung bremseregener Lenkunruhe in Personenkraftwagen. PhD Thesis, Technische Universität Darmstadt, Darmstadt, Germany, 1998.

**Fastl, H.; Zwicker, E. (Ed.):** Psychoacoustics. Facts and models. Berlin, Heidelberg: Imprint: Springer. ISBN: 978-3-642-51765-5, 2007.

**Fieldhouse, J. D.; Beveridge, C.:** An experimental investigation of hot judder. SAE Technical Paper 2001-01-3135. In: Proceedings of the 19th Annual Brake Colloquium and Exhibition, 2001, p.1–10.

**Fischer, S.; Könning, M.; Winner, H.; Nunes, R.; Sardá, A.; Hoffrichter, W.:** Theoretische und experimentelle Ordnungsanalyse von Heißrubbeln unter Variation des Bremsbelags. In: B. Breuer (Hg.): Proceedings of XXXIV. International  $\mu$ -Symposium. Bremsen-Fachtagung. Bad Neuenahr, Oktober 30. 794 Bände. Düsseldorf: Fortschritt-Berichte VDI Reihe 12 (12), 2015, p.1–22.

**Fischer, S.; Sardá, A.; Winner, H.:** Effects of different friction materials on hot judder – an experimental investigation. In: EuroBrake 2013. Dresden, Germany, 17-19. June, 2013, p.1–12.

**Gelfand, S. A.:** Hearing. An introduction to psychological and physiological acoustics. 5th ed. London: Informa Healthcare. ISBN: 978-1-4200-8865-6, 2010.

**Genuit, K. (Ed.):** Sound-Engineering im Automobilbereich. Methoden zur Messung und Auswertung von Geräuschen und Schwingungen. 1. Aufl. Berlin, Heidelberg: Springer-Verlag Berlin Heidelberg. ISBN: 978-3-642-01415-4, 2010.

**Gibbons, J. D.; Chakraborti, S. (Ed.):** Nonparametric statistical inference. Section 11.3. 4th ed., rev. and expanded. New York: Marcel Dekker Statistics, textbooks and monographs, v. 168. ISBN: 0-8247-4052-1, 2003.

**Graf, M.; Ostermeyer, G. P.:** Efficient computation of hot bands and hot spots. In: EuroBrake 2013. Dresden, Germany, 17-19. June, 2013, p.1–11.

**Grochowicz, J.:** Experimentelle und rechnerische Untersuchung zu Bremsdruck- und Bremsmomentschwankungen. PhD Thesis, Technische Universität Dresden, Dresden, Germany, 1995.

**Hartsock, D. L.; Fash, J. W.:** Effect of pad/caliper stiffness, pad thickness, and pad length on thermoelastic instability in disk brakes. In: *J. Tribol.* 122 (3), 2000, p.511. DOI: 10.1115/1.555394.

- Hartsock, D. L.; Hecht, R. L.; Fash, J. W.:** Parametric analyses of thermoelastic instability in disc brakes. In: *IJVD* 21 (4/5), 1999, p.510–526. DOI: 10.1504/IJVD.1999.005600.
- Haverkamp, M.:** Brake noise assessment by means of vehicle road tests subjective parameters and objective measurement concepts. SAE Technical Paper 2005-01-3940. In: 23rd Annual Brake Colloquium and Exhibition, OCT. 09, 2005.
- Head acoustics.:** Psychoacoustic Analyses I. Loudness and Sharpness calculation. Application Note – 12/13. Online available under: [https://www.google.de/url?sa=t&rct=j&q=&esrc=s&source=web&cd=2&ved=0ahUKEWjbiIHLyLHMAhVELcAKHX\\_HA7kQFggoMAE&url=https%3A%2F%2Fwww.headacoustics.de%2Fdownloads%2Feng%2Fapplication\\_notes%2Fpsychoacoustic\\_Analyses\\_I\\_e.pdf&usg=AFQjCNEmNjeZGNf6Cb7Hac1JEw1v6F6XGg&sig2=A9RzW\\_2n9hpbgjYBFHvRA&bvm=bv.120853415,d.bGs&cad=rja](https://www.google.de/url?sa=t&rct=j&q=&esrc=s&source=web&cd=2&ved=0ahUKEWjbiIHLyLHMAhVELcAKHX_HA7kQFggoMAE&url=https%3A%2F%2Fwww.headacoustics.de%2Fdownloads%2Feng%2Fapplication_notes%2Fpsychoacoustic_Analyses_I_e.pdf&usg=AFQjCNEmNjeZGNf6Cb7Hac1JEw1v6F6XGg&sig2=A9RzW_2n9hpbgjYBFHvRA&bvm=bv.120853415,d.bGs&cad=rja), latest accessed at 28. April.2016.
- Head acoustics.:** Psychoacoustic analyses II. Psychoacoustic analyses in the ARtemiS SUITE. Application Note – 01/14. Online available under: [https://www.head-acoustics.de/search\\_en/index.php?a=web&q=Psychoacoustic+analysis+I](https://www.head-acoustics.de/search_en/index.php?a=web&q=Psychoacoustic+analysis+I), latest accessed at 28. April.2016.
- Herkenrath, D. Heinrich.:** Bremsmomentenschwankungen infolge Unebenheiten der Bremsscheibe bei Pkw-Bremsen. PhD Thesis, Technischen Hochschule Aachen, Aachen, Germany, 2005.
- Hodges, T.; Dlugosch, F.-J.:** Entwicklung einer Methode zur Untersuchung von Bremsen-Kaltrubbeln. In: *ATZ Automobiltech Z* 103 (1), 2001, p.70–73.
- Honner, M.; Šroub, J.; Švantner, M.; Voldřich, J.:** Frictionally excited thermoelastic instability and the suppression of its exponential rise in disc brakes. In: *Journal of Thermal Stresses* 33 (5), 2010, p.427–440. DOI: 10.1080/01495731003733102.
- Inoue, H.:** Analysis of brake judder caused by thermal deformation of brake disc rotors. SAE Technical Paper 865131 865131, 1986.
- ISO 2631-1.:** Mechanical vibration and shock -- Evaluation of human exposure to whole-body vibration -- Part 1: General requirements, 01.05.1997.
- ISO 5349-1.:** Mechanical vibration -- Measurement and evaluation of human exposure to hand-transmitted vibration -- Part 1: General requirements, 01.05.2001.
- ISO 5349-2.:** Mechanical vibration -- Measurement and evaluation of human exposure to hand-transmitted vibration -- Part 2: Practical guidance for measurement at the workplace, 01.08.2001.

**Jung, T.; Chung, S.:** Research for brake creep groan noise with dynamometer. In: *SAE Int. J. Passeng. Cars - Mech. Syst.* 5 (4), 2012, p.1224–1229. DOI: 10.4271/2012-01-1824.

**Kämmer, S.:** Entwicklung einer Prüfmethodik zur Bestimmung von dynamischen Bremsmomentschwankungen am Schwungmassenprüfstand. Nr.1161/13. Bachelor Thesis, Technische Universität Darmstadt, Darmstadt, Germany, 2013.

**Kao, T. K.; Richmond, J. W.:** Brake disc hot spotting and thermal judder: an experimental and finite element study. In: *International Journal of Vehicle Design* 23 (3/4), 2000.

**Kao, T.-K.; Richmond, J. William; Moore, M. William.:** The application of predictive techniques to study thermo-elastic instability of brakes. In: Annual Colloquium On Brakes & Engineering Display, OCT. 09, 1994.

**Kasem, H.; Dufrénoy, P.; Desplanques, Y.:** Relationships between surface thermal gradients and disc distortion during stop-braking with high energy dissipation. In: *Tribol Lett* 48 (2), 2012, p.169–181. DOI: 10.1007/s11249-012-0003-z.

**Kim, M.-G.; Cho, C.; Kim, C.-B.:** Pressure change and variation of vibration in an automotive disk brake system due to hot spot. SAE Technical Paper 2007-01-3663. In: Asia Pacific Automotive Engineering Conference, 2007.

**Kreitlow, W.; Schrödter, F.; Matthäi, H.:** Vibration and “hum” of disc brakes under load. SAE Technical Paper 850079. In: SAE 1985 Transactions - V94-85, 1985, p.1430–1437.

**Kubota, M.; Suenaga, T.; Kazuhiro, D.:** A study of the mechanism causing high-speed brake judder. SAE Technical Paper 980594. In: Sealing for Automotive Applications - SP-1344, 1998, p.133–137.

**Lee, C. Feng.:** Brake force control and judder compensation of an automotive electro-mechanical brake. PhD Thesis, University of Melbourne, Victoria, Australia, 2013.

**Lee, C. Feng; Manzie, C.:** Adaptive brake torque variation compensation for an electromechanical brake. In: *SAE Int. J. Passeng. Cars - Electron. Electr. Syst.* 5 (2), 2012, p.600–606. DOI: 10.4271/2012-01-1840.

**Lee, C. Feng; Savitski, D.; Manzie, C.; Ivanov, V.:** Active brake judder compensation using an electro-hydraulic brake system. In: *SAE Int. J. Commer. Veh.* 8 (1), 2015. DOI: 10.4271/2015-01-0619.

**Lee, K.; Barber, J. R.:** Frictionally excited thermoelastic instability in automotive disk brakes. In: *J. Tribol* 115 (4), 1993, p.607–614. DOI: 10.1115/1.2921683.

**Lee, K.; Brooks, F. W.:** Hot spotting and judder phenomena in aluminum drum brakes. In: *J. Tribol.* 125 (1), 2003, p.44. DOI: 10.1115/1.1506315.

- Lee, K.; Dinwiddie, R. B.:** Conditions of frictional contact in disk brakes and their effects on brake judder. SAE Technical Paper 980598. In: *SAE 1998 Transactions - Journal of Passenger Cars* 107 (6), 1998. DOI: 10.4271/980598.
- Litos, P.; Honner, M.; Lang, V.; Bartik, J.; Hynek, M.:** A measuring system for experimental research on the thermomechanical coupling of disc brakes. In: *Proceedings of the Institution of Mechanical Engineers, Part D: Journal of Automobile Engineering* 222 (7), 2008, p.1247–1257. DOI: 10.1243/09544070JAUTO593.
- Little, E.; Kao, T.-K.; Ferdani, P.; Hodges, T.:** A dynamometer investigation of thermal judder. SAE Technical Paper 982252. In: *SAE 1998 Transactions - Journal of Passenger Cars* 107 (6), 1998. DOI: 10.4271/982252.
- Mauer, G.; Haverkamp, M.:** Measurement and assessment of noise caused by vehicle brake systems. In: *Proceedings of Inter-Noise 2007*. Istanbul, Turkey. Turkish Acoustical Society.
- McGill, R.; Tukey, J. W.; Larsen, W. A.:** Variations of box plots. In: *The American Statistician* 32 (1), 1978, p.12. DOI: 10.2307/2683468.
- Melz, T.:** Maschinakustik. Grundlagen. Lecture script, Fachgebiet Systemzuverlässigkeit und Maschinakustik, Technische Universität Darmstadt, 2013.
- Meyer, R.:** Brake judder - analysis of the excitation and transmission mechanism within the coupled system brake, chassis and steering system. SAE Technical Paper 2005-01-3916. In: 23rd Annual Brake Colloquium and Exhibition, October. 09, 2005.
- Möser, M. (Ed.):** Messtechnik der Akustik. Berlin, Heidelberg: Springer Berlin Heidelberg. ISBN: 978-3-540-68086-4, 2010.
- Müller, G. (Ed.):** Handbook of engineering acoustics. Heidelberg: Springer. ISBN: 978-3-540-24052-5, 2013.
- Neureder, U.:** Untersuchungen zur Übertragung von Radkraftschwankungen auf die Lenkung von Pkw mit Federbeinvorderachse und Zahnstangenlenkung. PhD Thesis, Technische Universität Darmstadt, Darmstadt, Germany, 2002.
- Okamura, T.:** Effect of material and dimensional homogeneity on thermo-mechanical deformation of brake discs during high-speed braking. In: *SAE Int. J. Commer. Veh.* 8 (2), 2015, p.293–301. DOI: 10.4271/2015-01-2673.
- Ostertagová, E.:** Modelling using polynomial regression. In: *Procedia Engineering* 48, 2012, p.500–506. DOI: 10.1016/j.proeng.2012.09.545.
- Panier, S.; Dufrénoy, P.; Brunel, J. F.; Weichert, D.:** Progressive waviness distortion: a new approach of hot spotting in disc brakes. In: *Journal of Thermal Stresses* 28 (1), 2004, p.47–62. DOI: 10.1080/01495730490498638.



- Panier, S.; Dufrénoy, P.; Weichert, D.:** An experimental investigation of hot spots in railway disc brakes. In: *Wear* 256 (7–8), 2004, p.764–773. DOI: 10.1016/S0043-1648(03)00459-9.
- Rees, D. G.:** Essential statistics. 4th ed. Boca Raton: Chapman & Hall/CRC Texts in statistical science. ISBN: 1-58488-007-4, 2001.
- Richard L. St. Pierre Jr.; Maguire, D. J.:** The impact of a-weighting sound pressure level measurements during the evaluation of noise exposure. In: Noise-Con 04. The 2004 National Conference on Noise Control Engineering. Baltimore Maryland, USA. 12-14, July, 2004, p.702–708.
- Rossing, T. D. (Ed.):** Springer Handbook of Acoustics. New York, NY: Imprint: Springer. ISBN: 978-1-4939-0754-0, 2014.
- Ruan, C.; Zhang, L.; Meng, D.:** A study on the bench test of friction-induced hot spots in disc brake. In: *SAE Int. J. Commer. Veh.* 8 (2), 2015, p.310–315. DOI: 10.4271/2015-01-2694.
- Sardá, A.:** Wirkungskette der Entstehung von Hotspots und Heißrubbeln in Pkw-Scheibenbremsen. PhD Thesis, Technische Universität Darmstadt, Darmstadt, Germany, 2009.
- Sardá, A.; Haag, M.; Winner, H.; Semsch, M.:** Experimental investigation of hot spots and thermal judder. In: 26th Brake Colloquium and Exhibition, October. 12, 2008.
- Sardá, A.; Seipel, G.; Winner, H.; Semsch, M.:** Wirkungskette der Entstehung von Hotspots und Heißrubbeln in Scheibenbremsen. In: XXVIII. Internationales  $\mu$ -Symposium. Bad Neuenahr, 24. Oktober, 2008.
- Schlecht, A.:** Minimierung der Schwingungsempfindlichkeit von Kraftfahrzeugvorderachsen. PhD Thesis, Technische Universität München, München, Germany, 2012.
- Sim, K. S.; Lee, J. H.; Park, T. W.; Cho, M. H.:** Vibration path analysis and optimal design of the suspension for brake judder reduction. In: *Int.J Automot. Technol.* 14 (4), 2013, p.587–594. DOI: 10.1007/s12239-013-0063-6.
- Steffen, T.:** Untersuchung der Hotspotbildung bei Pkw-Bremsscheiben. PhD Thesis, Universität der Bundeswehr Hamburg, Hamburg, Germany, 1998.
- Tan, M.; Wang, A.; Zhang, L.; Blaschke, P. G.:** A parametric study of brake roughness. In: 2002 IMAC-XX: Conference & Exposition on Structural Dynamics. Los Angeles CA, USA, 4-7 February. 2 Bände (4753), 2002, p.542–547.
- Tang, J.; Bryant, D.; Qi, H.:** A 3D finite element simulation of ventilated brake disc hot spotting. In: EuroBrake 2016. EuroBrake 2016. Milan, Italy, 13-15 June 2016. Fisita, 2016.

**Triches Jr, M.; Gerges, S. N. Y.; Jordan, R.:** Reduction of squeal noise from disc brake systems using constrained layer damping. In: *Journal of the Brazilian Society of Mechanical Sciences and Engineering* 26 (3), 2004, p.340–348. DOI: 10.1590/S1678-58782004000300011.

**VDI 2057 Part 1.:** Human exposure to mechanical vibrations -- Whole-body vibration, 2002-09.

**VDI 2057 Part 2.:** Human exposure to mechanical vibrations -- Hand-arm vibration, 2014-05.

**Woo, J. Hoon; Kim, J.; Kim, K. Yun; Ko, D.:** A study on the transfer path analysis of brake creep groan noise. SAE Technical Paper 2014-01-2510. In: SAE Brake Colloquium & Exhibition - 32nd Annual, October. 05, 2014

**Xu, X.; Winner, H.:** Experimental investigation of hot judder characteristics in passenger car. EB2015-VBN-006. In: EuroBrake 2015. Dresden, Germany, 4-5 May, 2015, p.1–12.

**Xu, X.; Winner, H.:** An experimental comparison of hot judder behaviours between dynamometer tests and vehicle tests. EB2016-SVM-007. In: EuroBrake 2016. Milan, Italy, 13–15 June 2016.

**Yi, Y.-B.; Barber, J. R.; Hartsock, D. L.:** Thermoelastic instabilities in automotive disc brakes — finite element analysis and experimental verification. In: *Contact Mechanics* 103, 2002, p.187–202. DOI: 10.1007/978-94-017-1154-8\_20.

**Yi, Y.-B.; Bendawi, A.; Li, H.; Zhao, J.:** Finite element analysis of thermoelastic instability in intermittent sliding contact. In: *Journal of Thermal Stresses* 37 (7), 2014, p.870–883. DOI: 10.1080/01495739.2014.912919.

**Yu, J.:** An analysis of fluid-mechanically-coupled, non-linear rotational vibration sensitivity of automotive hydraulic power steering systems. In: ASME 2004 International Mechanical Engineering Congress and Exposition: American Society of Mechanical Engineers, 2004, p.183–188.

**Yu, J.; Brickner, B.; Nutwell, B.; Johnson, M.:** Analysis of vehicle chassis transmissibility of steering shimmy and brake judder: mechanism study and virtual design of experiment. SAE Technical Paper 2007-01-2342. In: *SAE 2007 Transactions Journal of Passenger Cars: Mechanical Systems* 116 (6), 2007. DOI: 10.4271/2007-01-2342.

**Yu, J.; Nutwell, B.; Brickner, B.:** Analysis of vehicle chassis transmissibility of steering shimmy and brake judder: system modeling and validation. SAE Technical Paper 2007-01-2341. In: *SAE 2007 Transactions Journal of Passenger Cars: Mechanical Systems* 116 (6), 2007. DOI: 10.4271/2007-01-2341.

**Yu, J.; Slattengren, J.; Motoyama, K.:** Modeling and factor analysis of hydraulic power steering systems for rotational steering vibration by using msc. adams. In: MSC. Software Virtual Product Development Conference. Huntington Beach, California, USA, 2004.

**Zeller, P.; Andreas, E.; Fastl, H. (Ed.):** Handbuch Fahrzeugakustik. Grundlagen, Auslegung, Berechnung, Versuch herausgegeben von Peter Zeller. 2. Aufl. Wiesbaden: Imprint: Vieweg+Teubner Verlag ATZ. ISBN: 978-3-8348-8657-6, 2012.

**Zhang, L.; Ning, G.; Yin, X.; Yu, Z.:** Experimental research on the transfer path of steering wheel wobbling induced by brake judder. In: *Journal of Vibration and Shock* 25 (2), 2006, p.70–74.

**Zhang, L.; Ning, G.; Yu, Z.:** Brake judder induced steering wheel vibration: experiment, simulation and analysis. SAE Technical Paper 2007-01-3966. In: 25th Annual Brake Colloquium, 2007.

---

## Own publications

**Xu, X.; Winner, H.:** An experimental comparison of hot judder behaviors between dynamometer test and vehicle test. In: EuroBrake 2016, EB2016-SVM-007. 13-15 June 2016, Milan, Italy, 2016

**Winner, H.; Fischer, S.; Xu, X.; Könnig, M.:** Heißrubbeln - Experimentelle Beobachtungen und Erklärungsmodelle. In: VDI-Fachkonferenz Innovative Bremsentechnik, VDI-Berichte 2241. 14-15 October 2015, Hannover, Germany, 2015

**Xu, X.; Winner, H.:** Experimental Investigation of Hot Judder Characteristics in Passenger Car. In: EuroBrake 2015, EB2015-VBN-006. 04-05 May 2015, Dresden, Germany, 2015

---

## Supervised Bachelor/ Master theses

**Yu, Lingpeng:** Simulation und Analyse der Auswirkungen verschiedener Bremsscheibenoberflächengeometrien auf Bremsmomentschwankungen. Master-Thesis Nr. 558/15, 2015

**Du, Fanglei:** Identifikation der Heißrubbeln-beeinflussenden Eigenfrequenzen in Pkw. Master-Thesis Nr. 575/15, 2015

**Guo, Guicun:** Untersuchung und Bewertung des Brummgeräuschs in Pkw. Master-Thesis Nr. 566/15, 2015

**Zingel, Philipp:** Untersuchung des Übertragungsverhaltens von Heißrubbeln in Pkw. Bachelor-Thesis Nr. 1202/14, 2014

**Dong, Mingzhe:** Identifikation des Auftretens von Heißrubbeln in Pkw. Master-Thesis Nr. 542/14, 2014

---

# Curriculum vitae

## Personal data

Name: Xinfu Xu  
Birthdate: 29.12.1986  
Birthplace: Shandong, China

## Education

2002 – 2005 High School-Shandong Yishui No.2 High School  
Shandong, China

2005 – 2009 B. Sc. in Vehicle Engineering  
Yanshan University  
Hebei, China

2009 – 2011 M. Sc. in Transportation Engineering  
Tongji University  
Shanghai, China

2012– 2016 Doctorate in Automotive Engineering  
Prof. Dr. rer. nat. Hermann Winner  
Institute of Automotive Engineering  
Technischen Universität Darmstadt